On-site Aerodynamic Analysis of Runners

Master in Aerodynamics

Michael Buszek

Delft University of Technology

TU Delft

On-site Aerodynamic Analysis of Runners

by

Michael Buszek

to obtain the degree of Master of Science
at the Delft University of Technology,
to be defended publicly on Wednesday March 12, 2025 at 13:45.

Student number:	4773934	
Project duration:	September 2023 – February, 2025	
Thesis committee:	Dr. Sciacchitano,	TU Delft, supervisor
	Dr. Ir. Terra,	TU Delft
	Prof. Dr. Scarano	TU Delft, examiner
	Dr. Ir. van Oudheusden	TU Delft, chair

This thesis is confidential and cannot be made public until 22.09.2025

TU Delft

Preface

This M.Sc. thesis marks the culmination of my Aerodynamics and Wind Energy master's program at the Faculty of Aerospace Engineering at Delft University of Technology.

I would like to thank Dr. Andrea Sciacchitano and Ir. Wouter Terra, for providing me an opportunity to conduct this highly practical research, in which I could work with both my hands and my head, and had a chance to use state of the art technology. I would also like to thank them for the knowledge they shared with me along the way.

I would also like to thank Cristina D'angelo for the help in data analysis, Dennis Bruikman for facilitating the physical building of the experiment, Adrian Grille Guerra for making the bubbles flow, and Gert-Jan Berends for resolving countless server issues.

Furthermore, I extend my gratitude to the athletes for spending their time with us, and to the many others in Apeldoorn, who contributed to the success of this research.

Michael Buszek
Delft, February 2025

Abstract

Aerodynamic drag plays a critical role in high-speed sports, including running, where small performance margins can be decisive for victory in elite competitions. Despite its importance, research on running aerodynamics remains underexplored, with most studies relying on stationary mannequins or simulations that do not capture the dynamic behavior of flow around a moving runner. In other words, there is a significant research gap in experimentally visualizing the wake flow and accurately measuring the drag in real-world running scenarios. This study aims to address this research gap.

In recent years, the Ring of Fire measurement technique has emerged as a feasible option to visualise and analyse flow structures of transiting objects based on particle image velocimetry. The technique has already been proven in sports like cycling and ice skating, but has not yet been applied to running. This study adapts the Ring of Fire measurement method for sprinting athletes, and the raw images are processed by Shake-the-Box (STB) Lagrangian Particle Tracking. This results in a three-dimensional, time-resolved velocity field in the wake of a runner with an uncertainty of less than 5% of the runner's speed. This velocity field is used for qualitative flow visualisations, as well as for drag estimations, which are computed from a control volume approach by utilising the flow field before and after the passage of the athlete.

The experimental methodology involved nine junior athletes, wearing both standard sprint suits and aerodynamic suits, sprinting at constant speeds through a measurement setup including three high speed cameras, four LED arrays and Helium Filled Soap Bubbles (HFSB).

The results of the investigation include the visualisation of the full wake, quantification of the velocity deficit, a qualitative vorticity analysis, some lateral velocity findings and the measured values for drag of one of the athletes.

There are multiple interesting findings about the flow around a dynamic runner in this report. One of them is the splitting of the wake into two side-by-side stream tubes in the far wake. The velocity deficit in a relevant region of the dynamic wake has also been quantified, and it is shown to vary with the inverse of the distance behind the runner, which is useful information for trailing runners. Another interesting observation is that the vorticity field in the near wake generally follows the rules of finite cylinder flow, where the body parts of the athlete are finite cylinders with variable diameter. The hypothesis that the flow should have a lateral oscillation related to the frequency of the runner's steps has also been confirmed.

This study demonstrates the applicability of the Ring of Fire system to running aerodynamics and offers the full visualisation of the three dimensional flow in the wake of a moving runner, bridging the research gap to pave the way for further advancements in the field.

Contents

List of Figures

List of Tables

1

Introduction

This chapter summarises the research gaps in the relevant research field and develops the goals of this research.

Section 1.1 highlights the importance of aerodynamic drag in running sports. Then, section 1.2 finds a research gap in the field of running aerodynamics. Finally, section 1.3 lists the goals of this research.

1.1. Importance of drag in running sports

For a long time, aerodynamic drag was an important field of research in many racing sports, for example cycling, skiing, motorsport, etc. However, research on running aerodynamics remains underexplored. This subsection discusses how an advancement in running aerodynamics could lead to enhanced results in running competitions.

According to Schickhofer et al., aerodynamic drag consumes about 7-9% of a sprinter's total mechanical power in the velocity range of 30 to 36 km/h, the fraction becoming more significant with increasing speed [1]. According to Hill [2], air resistance accounts for at most 5% of total resistance, the remainder of the resistance being in muscles and limbs themselves. Drag is of course a smaller percentage of total resistance than in the other mentioned sports due to running's comparably low speed, but studies have already shown that reducing a runner's drag by a small margin can make the difference between first and second place in an Olympic competition in a whole range of running distances [3] [4]. In other words, the winning time margins are extremely small compared to the timescale of the race, so a small improvement in a runner's performance can be decisive in a top level competition.

Kyle also points out the importance of air resistance in sprinting and uses a mathematical model to predict that in sprinting and long distance running races, a 2% reduction in drag can result in "substantial lead distances with little effort required on the runner's part" [5].

Beaumont et al. show another approach to the importance of drag in running, predicting a 0.6km/h velocity increase at equal metabolic cost of running in a drag-reducing running formation [6].

As for the 100m race specifically, Murieka shows a reduction in the 100m sprint time of 0.1s with a back wind of 2m/s [7] (which effectively reduces the air resistance of the runner), which suggests that an aerodynamic improvement can have a positive effect on the 100m sprinting times.

1.2. Research gap in running aerodynamics

Current research in the field of running aerodynamics is quite limited. There have been simulations and experiments dealing with drag reduction of running in formations and using sports textiles, but to the author's best knowledge, there is no complete research that shows the real behavior of the flow around a moving runner.

Most research done in the past uses stationary manequins for experiments, including the experiments by Hill [2], Kyle et al. [5] and Chowdhury et al. [3], or stationary human models for simulations, in the

numerical research by Zhang et al. [8], Schickhofer et al. [1], Beaumont et al. [6], Forte et al. [9] and Kim et al. [10]. Some of this research provides good flow visualizations around the models, but it is not confirmed that the flow would behave the same way around a real moving human.

The only recent paper found that considers a real moving runner is published by Pecchiari et al. [11]. They placed a treadmill with a runner in a wind tunnel, but the research is missing flow visualization around or behind the runner, it instead focuses on the drag measurement itself. Pecchiari et al. also confirmed that before their research, no direct measurement of the drag in walking and running humans was available.

It is therefore concluded that there is a significant research gap in the area of experimental measurements of flow topology in the wake of a moving runner. With the recent development in quantitative flow visualization (large-scale PIV) by Caridi et al. [12], this kind of measurement is now facilitated.

Furthermore, most of the research on running aerodynamics mentioned in this subsection deals with slower, long distance running, like marathons or race walking, but not much research is done on sprinting specifically. Sprinting aerodynamics can be influenced by different phenomena than the aerodynamics of slower running due to the greater displacement of sprinters' limbs during motion and the increased fraction of running time spent airborne between steps.

This thesis partly focuses on filling those research gaps and exploring the evolution of the wake behind a real moving sprinter, recognizing the main flow structures and possibly linking them to the resulting drag values.

1.3. Main goals of this research

This subsection summarises the goals of the research that this literature study supports.

The first goal of this research is to improve the existing measurement and processing methods, including the use of the Shake the Box processing method and the development of a new seeding injection system.

The second goal of this work is to fill the research gap in running aerodynamics by applying the improved measurement and processing methods to professional sprinters to understand the general flow characteristics around a sprinter and possibly find areas where drag can be reduced.

2

Running Aerodynamics

This chapter dives into the background information in the topic of running aerodynamics. In section 2.1 different aspects of aerodynamic drag on a runner are discussed. In section 2.2 the background information on the topic of bluff body aerodynamics is presented. Finally, section 2.3 explores the approaches used in the past for numerical and experimental investigations into running aerodynamics.

Then, the results of some previous studies on running aerodynamics are presented and any useful information available on the flow topology and general flow structures is extracted. In section 2.4 the flow visualisations are collected from available literature. In section 2.5 the effect of the phase of the step on flow topology is investigated. In section 2.6 the effects of runner height and tilt on drag are described. Finally, section 2.7 shows the Reynolds number effect on drag.

2.1. Aerodynamic drag

Throughout this report, frequent references are made to the aerodynamic drag produced by the runner. It is crucial, therefore, to specify the definition used. The drag force encountered by a body moving through a fluid is usually represented by Equation 2.1, and throughout this report the same definition will be used.

$$D = \frac{1}{2}\rho V^2 S C_D \tag{2.1}$$

In Equation 2.1, D represents the overall aerodynamic drag force, $\frac{1}{2}\rho V^2$ denotes the dynamic pressure, C_D signifies the drag coefficient of the cyclist, and S represents a reference surface, which in this case is the projected frontal area, used with the same name amongst others by Spoelstra et al. [13]. The drag force defined by Equation 2.1 acts in the direction directly aligned with the relative air velocity to the runner. For this reason, an assumption is made that the freestream conditions before the runner's passage through the experimental setup are static enough to ignore the directionality of drag. The benefit of this assumption is that the drag can be calculated exactly along the running vector. This has been done before by Spoelstra et al. with good results [13], [14].

This thesis also deals with a term called drag area. This is the product of the reference area and the drag coefficient as shown in Equation 2.2, and is expressed in square meters (m²).

$$\text{drag area} = C_D S = \frac{D}{\frac{1}{2}\rho V^2} \tag{2.2}$$

The use of drag area is useful for comparisons of drag results between runners of different geometry, without the need for projected frontal area measurements. Not only is this convenient for comparing runners within this study, but it also facilitates comparisons to running drag results in literature, where the projected frontal area is not obtainable.

2.2. Bluff body aerodynamics

A runner can be characterised as a bluff body, which is defined by large regions of separated flow and high aerodynamic drag, largely dominated by the pressure drag, as explained by Roshko [15]. The shape of a human running at constant speed is similar to the shape of a vertical cylinder, especially around the torso area. Therefore, this section gives some background information on general bluff body aerodynamics, to hopefully facilitate the understanding running aerodynamics.

The Reynolds number (Re) characterizes the balance between inertial and viscous forces acting on a body. It is represented mathematically by Equation 2.3.

$$Re = \frac{U_\infty D}{\nu} \tag{2.3}$$

In Equation 2.3, U_∞ stands for the free stream velocity, D represents the width of the bluff body, for example cylinder diameter, and ν denotes the kinematic viscosity of the fluid, which for air is equal to $1.48 \cdot 10^{-5} m^2/s$.

Figure 2.1 shows the four flow ranges of the flow past circular cylinders depending on Reynolds number, and how each stage affects the drag experienced by the cylinder.

According to Achenbach, in the subcritical flow regime the surface roughness does not yet significantly affect the flow. Within a wide range of small Reynolds numbers, the drag coefficient remains relatively stable. However, as the Reynolds number increases, there is a sudden decrease in the drag coefficient for a specific range of Reynolds numbers. This transition marks the critical flow regime, where the lower limit of the drag coefficient as well as its location on the Reynolds number range depend on the roughness of the surface. Beyond the critical point, the drag coefficient begins to increase again, entering the supercritical range, until it reaches a nearly constant value in the transcritical range [16].

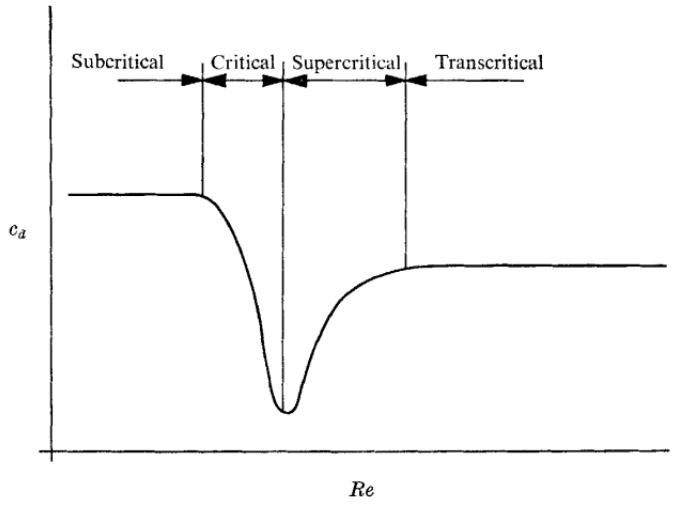

Figure 2.1: The four flow ranges of the flow past circular cylinders by Achenbach [16]

Taking a runner's shoulder width as the equivalent to a cylinder's diameter, the Reynolds number of a runner running with the speed of 8m/s with the average shoulder width of 40cm is in the order of $2 * 10^5$, which falls right between the subcritical and critical regions of flow in Figure 2.1 for a normal smooth cylinder. However, a runner is not a perfect cylinder and their rougness is not zero.

Figure 2.2 shows in more detail the drag coefficients of circular cylinders in cross flow at different roughness levels defined by k_s/D, where k_s is the roughness height and D is the same as in Equation 2.3. Clearly, increasing the roughness height shifts the critical region to smaller Reynolds numbers and increases the minimum achievable drag coefficient.

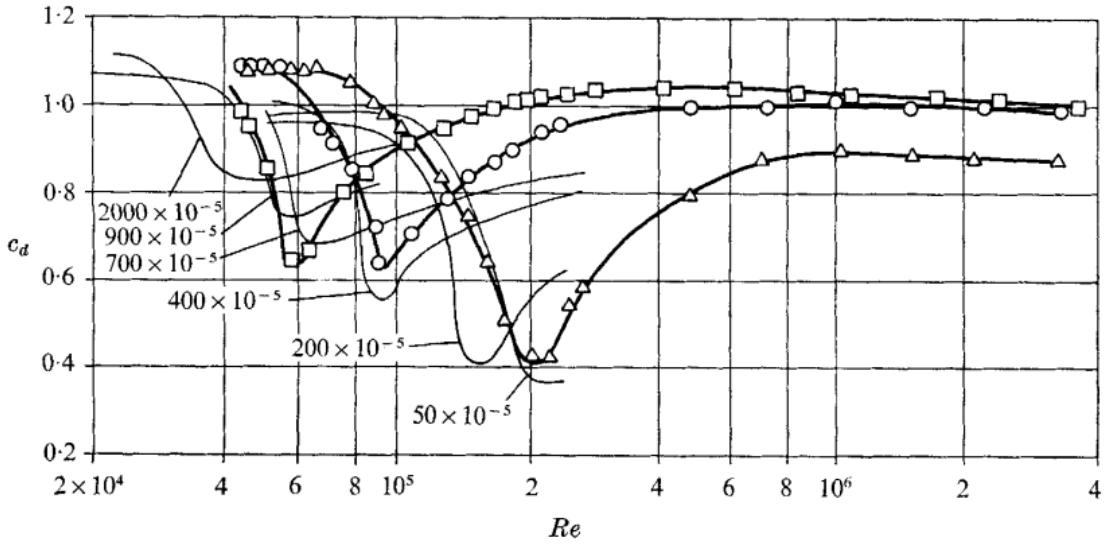

Figure 2.2: Drag coefficients of circular cylinders in cross flow at different roughness levels (roughness height/diameter of cylinder) by Achenbach [16]

According to Achenbach, the decrease of drag in the critical region is sensitive to many factors [16]. Therefore, the outcome of this data that is interesting for applications to runners, which are not perfect cylinders in not perfect conditions, is that increasing the roughness height at the runner's Reynolds number of around $2 \cdot 10^5$, makes it more probable that more of the flow will be in the transcritical region where drag is lower, and less of the flow will be in the subcritical region where drag is higher. This especially applies to arms and legs, which have smaller diameters and therefore lower Reynolds numbers at the same velocity.

The effect of roughness on the aerodynamic drag of bluff bodies, specifically applied to humans in sport positions, was studied by Chowdhurry et al. [3]. They did wind tunnel testing of cylinders wrapped in different textiles at different angles of attack, and concluded that "the bare smooth cylinder possesses higher aerodynamic drag at all speeds compared to rough surface textiles" and that the "right selection of textiles for athletes is utmost important for achieving aerodynamic advantages."

2.3. Investigation approaches

The aerodynamic drag of an athlete can be estimated experimentally or numerically. This section discusses the applicability of both for the measurement of a runner in motion. Additionally, it considers some flow visualisation techniques to explore the options available for the following research.

2.3.1. Numerical simulations

At a first glance, numerical simulations seem like the best option for flow visualisation of a runner. Not only can they predict the flow both around the runner and in their wake, but they also generate data in the entire simulation domain, often with good resolution.

Zhang et al. [8] used CFD simulations to investigate the aerodynamic drag reduction for race walking formations. The Navier–Stokes equations for momentum conservation are discretized using the Reynolds-averaged (RANS) approach. The simulations are performed with the commercial CFD code Ansys Fluent. They arrive at different interesting flow visualisations, including pressure fields, velocity fields and streamlines. The simulations are performed for an unsteady state, since the walker is a bluff body, but the model itself is non moving. This can provide data about the general flow characteristics around a vertically positioned human body, but it does not provide enough detail about the movement of running. Furthermore, Zhang et al. pointed out that previous CFD studies on running used similar mathematical models, but arrived at very different drag coefficient values (19% difference), depending on factors like positions of hands and legs.

Similar research was performed in multiple other studies, including Schickhofer et al. [1] and Beaumont et al. [6] for investigating more running formations, and Forte et al. [9] for estimating the drag coefficient throughout a wide range of running and walking speeds.

Kim et al. [10] took an interesting approach to try to overcome the issue of simulating flow around a stationary model. They measured running participants on a treadmill with inertial measurement unit sensors to estimate the angles of different joints at different phases of the running step. They considered two main parts of the cycle: the takeoff phase and the touchdown phase. They state that "although there is a difference from a real runner, the range of the cross-sectional area for two postures can cover the cross sectional area when a runner moves. Consequently, the aerodynamic characteristics can be roughly estimated from the stationary model." This is certainly an improvement over estimating drag from just one part of the running cycle, but as acknowledged by the researchers, the results still have limitations.

Kim et al. [10] also develop a mathematical model based on drag data known for different simple shapes at different angles of attack, and the results are somewhat comparable to the results from the simulations.

To conclude, plenty of research has been done on running and walking aerodynamics via numerical simulations, but simulating a complex body in motion would be a big challenge and to the best knowledge of the author, it has not been done yet, at least in the field of running aerodynamics. The static body simulations are not sure to provide an accurate drag estimation and the flow visualisations might miss some flow structures that develop specifically when the body is moving.

2.3.2. Experimental measurements

The drag calculated by the numerical simulations from the previous subsection can be validated with physical experiments in a wind tunnel. Originally, Hill [2] performed wind tunnel experiments on a small scale static mannequin to calculate the drag coefficient.

Kyle et al. [5] followed up on the research and used full scale segments of a human mannequin to test for the effect of different clothing and hair configurations on drag.

More recently, Inoue et al. [17] developed a moving-belt system for a wind tunnel and placed a static small scale model in the test section just above the moving belt. This simulated the effect of the manequin moving with respect to both the air and the floor, and changed the boundary condition of the floor to be more realistic.

Later, Pecchiari et al. investigated "terrestrial locomotion" in a larger wind tunnel to fit a real runner on a treadmill in the test section. In their study, they "directly measured the force exerted by still air resistance on eight male subjects during walking and running on an instrumented treadmill with a belt moving at the same speed of a flow of laminar air facing the subject" [11]. The drag was measured by the ground reaction force of the treadmill. The result of the study is a predictive equation to estimate drag as a function of the speed and the height of the runner.

Pecchiari's method is good for an accurate drag measurement of a moving human, which all the previous research neglected. This method could also be used for investigating the effect of aerodynamic clothing on the drag.

However, nothing was done in their research to understand the flow topology. In addition to ground reaction force measurements, more information can be extracted from the experiment with flow visualization techniques. Some of the more recent experiments involving flow measurement techniques will be presented here with the aim of providing the reader with a comprehensive understanding of the progress achieved up to this point.

A different approach to measuring the drag of a moving object is to abandon the wind tunnel and have the measured object transiting through static air. According to Spoelstra et al. [13], this has been done for cyclists with the coast-down technique or using power meters. However, since running is a more complex motion, those methods are not possible. If a runner would have to be investigated in an on-site measurement without a wind tunnel, the drag could be measured from the flow itself, via momentum conservation. In that case a flow measurement technique is needed to recreate the velocity field on

which the conservation of momentum can be used. This has been demonstrated by Terra et al. [18] by measuring the drag of a transiting sphere by large-scale tomographic-PIV. Later a similar method has been used by Spoelstra et al. to measure the drag of cyclists and ice skaters [13], [14].

In chapter 3, a more comprehensive examination of the applicable flow measurement techniques will be conducted to evaluate each technique's efficacy and applicability to the following research.

2.4. Flow visualisations available in literature

The flow visualisations presented in this section come from numerical simulations with a static human model only, because of the lack of availability of any other data.

2.4.1. Velocity fields

This subsection looks at results from past research and identifies the following main flow structures for a runner:

- downwash originating from head and upper back
- large flow separation and reverse flow behing shoulder area and hip area
- asymmetry due to arm positions: alternating sideways flow in the wake at arm height

Zhang et al. [8] discuss the impact of walking formations on the flow and they provide useful velocity field data for a single race walker. This is displayed in Figure 2.3. Schickhofer et al. [1] also shared images of velocity data around runners, which can be seen in Figure 2.5. Both of those visualisations were performed using CFD with static human models.

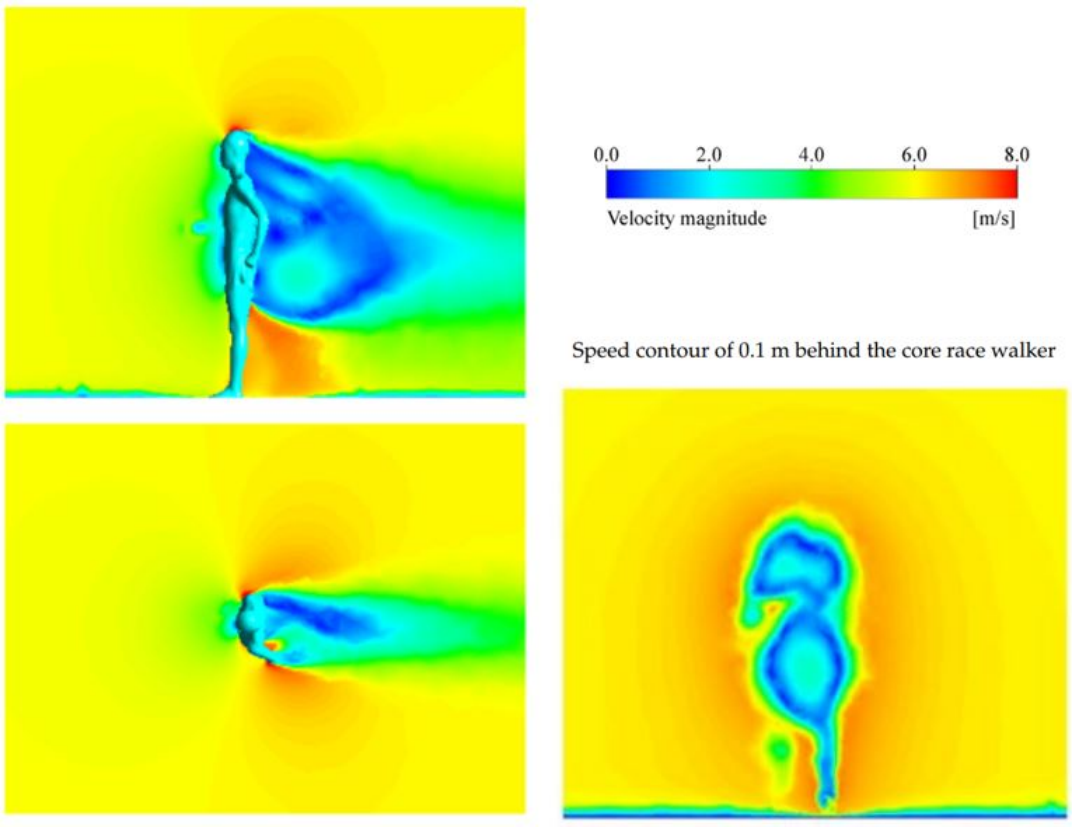

Figure 2.3: Velocity field three view of the wake of a single race walker by Zhang et al. [8]

In Figure 2.3 the wake of a race walker computed by CFD is presented in three planes. The image on the right is taken in a plane 0.1m behind the walker, so it still resembles a human shape.

Since a runner runs in a similar upright posture with differences mostly in limb angles, it can be assumed that the head and torso sections would produce a comparable flow on a runner.

Since only velocity magnitude is presented, it is difficult to decide the direction of the flow in some places, but it can be reasoned that there is a recirculation region behind the lower back of the walker, since there is a circular region of around 2m/s velocity inside of a circle of zero velocity, so it can be assumed that the velocity vector changes sign to negative across the region of zero velocity.

From the side view, it is clear that the head has a large region of attached flow, after which there is separation and the flow is pulled downwards. Therefore, one of the main flow structures is a downwash from the head region going down to the back.

Looking at the back view, the head does not have much effect on the wake, which is affected mostly by two regions of biggest back flow: shoulders and hips with lower back. Therefore, another main flow structure is the flow towards the running direction following the shoulders and the lower back.

The reason why at the height of the head and the legs the reverse flow region is less significant is that they are narrower in cross section and more slim in shape, so mostly attached flow goes around the neck or between the legs, and fills in the velocity deficit that would be present there if the human was replaced by a uniform cylinder of the same height. This can be nicely seen in Figure 2.4.

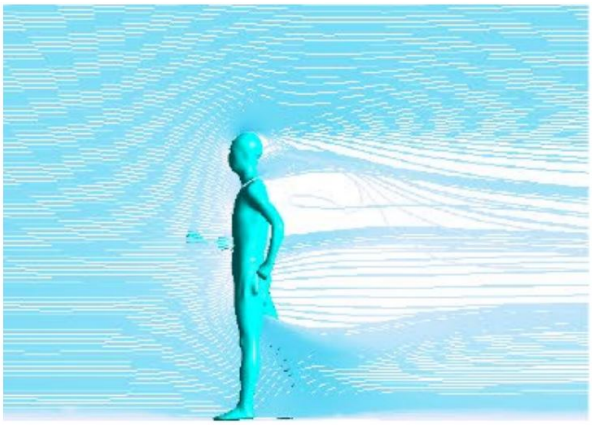

Figure 2.4: Side view of the streamlines passing around a race walker by Zhang et al. [8]

Another aspect of the flow to recognise is the asymmetry visible from the top view. Even though the model is static, it has one arm backwards and one forwards (the arms of the model can be seen more clearly in Figure 2.6), which causes higher flow velocities (less bluff body separation) on the side with the arm backwards. Therefore, for a runner another expected main flow stucture is an alternating sideways flow in the wake at arm height.

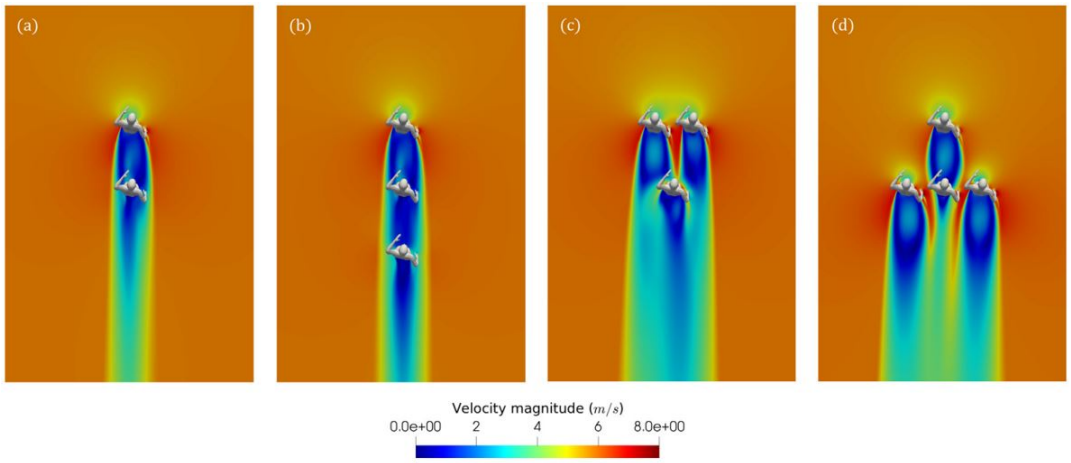

Figure 2.5: Top view of the velocity fields of runner formation wakes by Schickhofer et al. [1]

Figure 2.5 confirms together with Figure 2.3 that a wake of a runner has a significant velocity deficit a long distance behind a runner. This means the momentum term of the equation for drag is significant for a long distance behind the runner.

Figure 2.5 also confirms the asymmetry of the flow due to a difference in arm position between the left and the right sides. In this case, the wake turns slightly left.

2.4.2. Pressure fields

Pressure is a significant term in a drag estimation, specifically the difference between the front and the back pressure. While no data is available on the percentage of drag caused by pressure for runners, it is known that ”bluff bodies are not streamlined, and so the drag is primarily pressure drag, due to the higher pressure at the front of the body than at the rear”. [19] Therefore, it is important to understand what kind of pressure distribution to expect from a real runner. This section finds all the data available on a runner’s pressure distribution.

Zhang et al. [8], Beaumont et al. [6], and Schickhofer et al. [1] published results of CFD simulations, and amongst others they shared some pressure field visualisations. They are analysed in this subsection to extract any necessary information.

The pressure coefficient referred to in this subsection is defined by Equation 2.4.

$$C_p = \frac{P - P_\infty}{\frac{1}{2}\rho_\infty U_\infty^2} \tag{2.4}$$

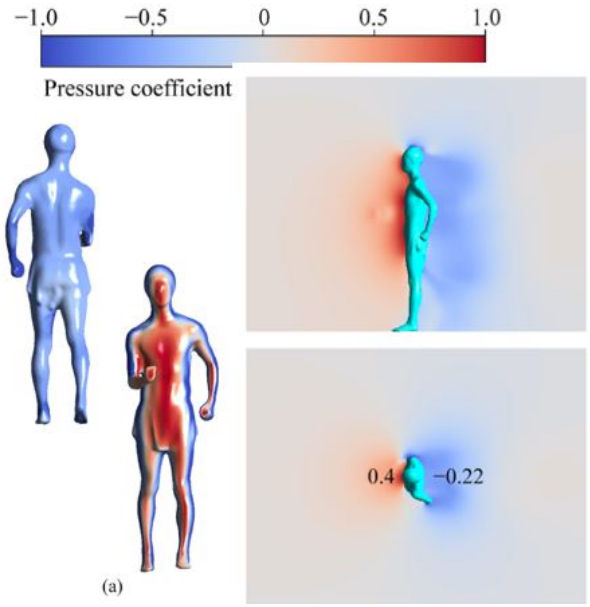

Figure 2.6: Pressure data on a race walker by Zhang et al. [8] The numbers on the top view graph are pressure coefficients at some distance (selected by the author but not mentioned) from the chest for pressure comparisons with other formations.

In Figure 2.6, Zhang et al. show the distribution of pressure coefficient on the 3-dimensional surface of a race walker.

On the front, where the stagnation point is, the pressure is close to 1. Towards the sides, the pressure reaches its lowest point as the flow accelerates around the body, just before flow separation. On the back surface of the walker, the pressure coefficient is negative but with a small magnitude, which suggests separated flow. Upon closer inspection it can also be seen that the pressure coefficient is more negative on the back surface between two volumes, for example in the groin or between the arm and the body, where the flow accelerates more due to Bernoulli's principle: the area that the air passes through is smaller, so the velocity is higher and therefore the pressure is lower.

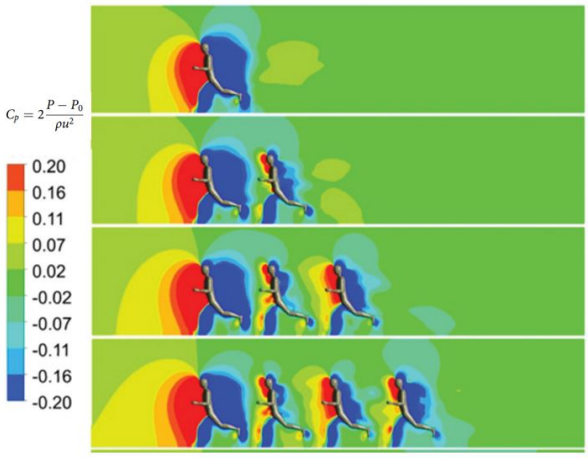

Figure 2.7: Pressure fields around formation runners by Beaumont et al. [6]

In Figure 2.7, Beaumont et al. show more clearly the side view of the pressure field around a runner, which is more related to this research than a walker. The case with 1 runner is particularly applicable to the current research.

The area in front of a runner is characterised by an increased pressure at least 2 body lengths in front of him.

The main low pressure zone in the wake of the runner extends less than 1 body length behind him, which for a full scale human would be 1-2 meters. However, up to around 1.5 body lengths there is still a visible effect of the runner on the pressure in the wake, in fact the pressure coefficient in some areas behind the runner is even positive.

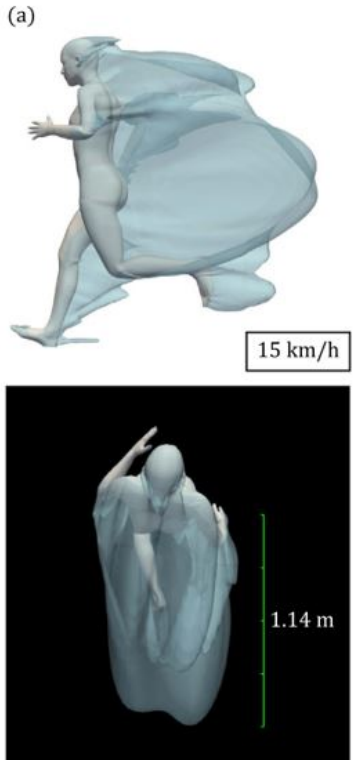

Figure 2.8: Wake behind a runner visualised by an isosurface of pressure at $P_{tot} = 0$ by Schickhofer et al. [1]

A similar result is obtained by Schickhofer et al.. In Figure 2.8 the isosurface of pressure corresponding to freestream is plotted in 3 dimensions. Inside of the isosurface there is a negative pressure coefficient, and outside the pressure should be around freestream, as in Figure 2.7. The size of the area of negative pressure coefficient is similar in the two figures, reaching slightly less than 1 body length behind the runner.

The size of the volume inside of the isosurface should be correlated with the magnitude of separation happening around the body, and therefore to drag. From Figure 2.8, it can be deduced that a significant area of separation originates from the hips (as seen from the side view) and the shoulders (as seen from the top view). This is in agreement to what has been found in subsection 2.4.1.

From this information, knowing that flow separation can be reduced by introducing roughness or vortex generators, it can be deduced that the flow around a runner can be optimised for minimum drag by installing roughness or vortex generators around the shoulders and on the sides of the hips.

2.5. Variation in flow in different phases of the step

The research done up to now on running aerodynamics with flow visualisation consists of only numerical simulations on static models. Kim et al. [10] tried to overcome the problem of a static model by simulating the static body in two different phases. They use the following names for the two phases:

- takeoff - where the back foot leaves the ground
- touchdown - where the front foot lands on the ground

To arrive at the exact geometry of the human in those two phases, Kim et al. measured running participants on a treadmill with inertial measurement unit sensors to estimate the angles of different joints at different phases of the running step. They state that ”although there is a difference from a real runner, the range of the cross-sectional area for two postures can cover the cross sectional area when a runner moves. Consequently, the aerodynamic characteristics can be roughly estimated from the stationary model.” [10].

Figure 2.9 and Figure 2.10 show the velocity fields around the simulated runner in takeoff and landing positions, with speed of flow represented by the color of streamlines.

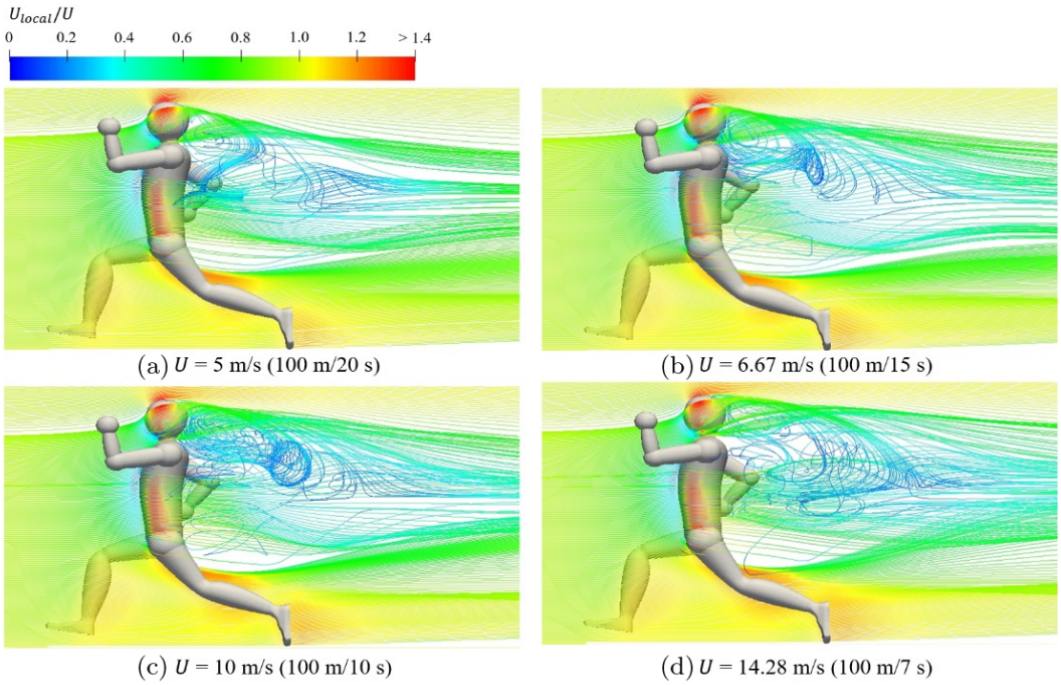

Figure 2.9: Instantaneous velocity field around a runner in takeoff position, with speed of flow represented by the color of streamlines by Kim et al. [10]

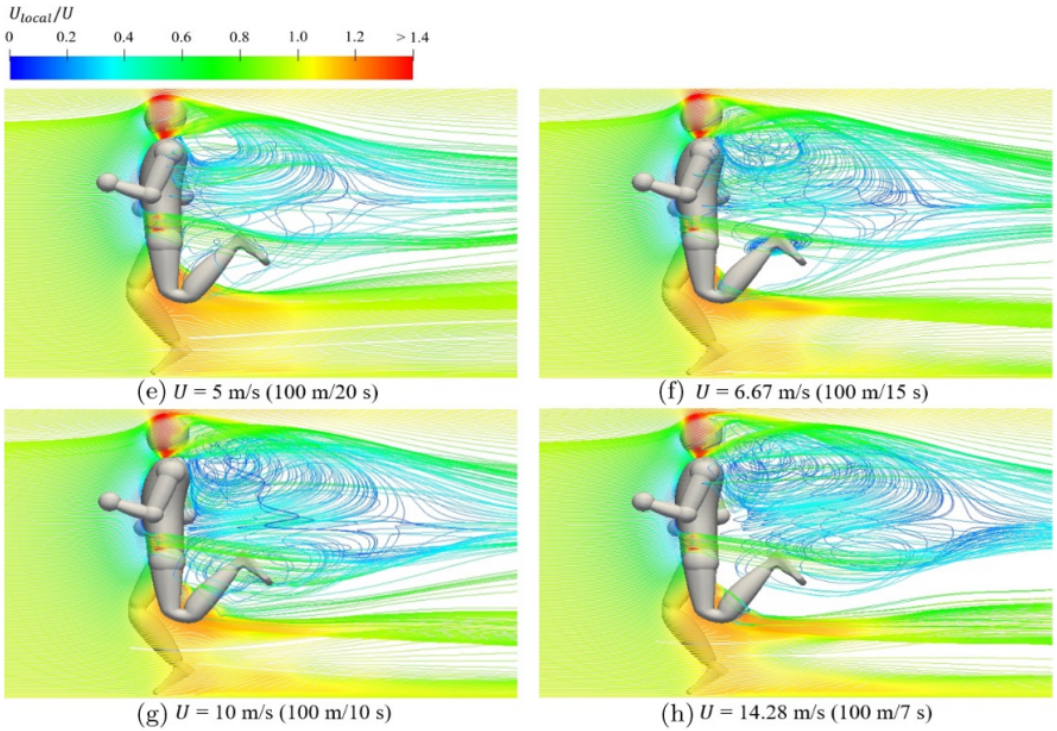

Figure 2.10: Instantaneous velocity field around a runner in touchdown position, with speed of flow represented by the color of streamlines by Kim et al. [10]

The first observation that Kim et al. make is that the wake region is more complex at high-running speeds at takeoff and touchdown. Another observation is that the flow between the left and right leg accelerates because of the decreased area [10]. However, Kim et al. do not discuss in depth the flow field, so more observations will be made below.

Comparing Figure 2.9 and Figure 2.10, the streamlines seem to be separating mostly around the head and shoulder area during takeoff. In comparison, during touchdown the separation becomes intense around the hip area as well. One reason for this could be that during takeoff, the upper arms are away from the torso, one being forward and one being backwards. Meanwhile, during touchdown the upper arms are vertical and close to the torso, which effectively increases the frontal area of the torso.

Another difference between the two phases is the position of the feet. During takeoff, both feet are immersed in the flow, while during touchdown the back foot is in the separated wake caused by the hip, effectively decreasing the inflow velocity to the foot and shin, which could cause lower drag. However, for a moving runner this should not be the case, because during the step the foot is connected to the ground, and therefore it does not recieve the freestream flow.

More information can be extracted from Figure 2.11, where Kim et al. show the surface velocity distribution on the runner's skin at takeoff and touchdown positions.

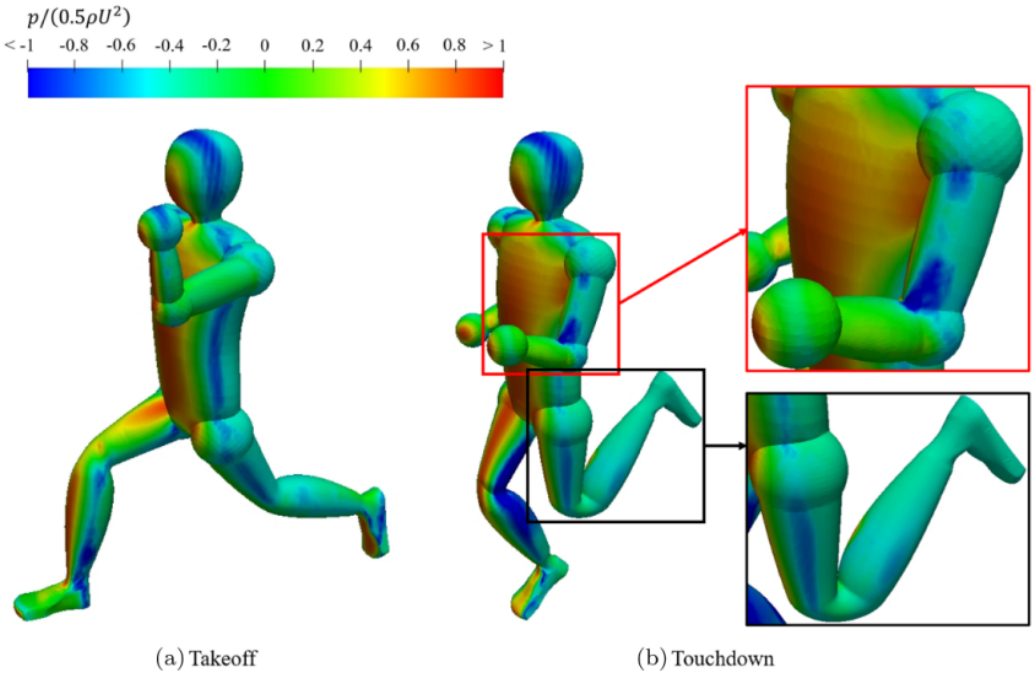

Figure 2.11: Surface velocity distribution on the runner's skin at takeoff and touchdown positions by Kim et al. [10]

Kim et al. observe that at touchdown the high pressure is distributed along the frontal surfaces of the head, body, and forward leg. It is also noted that "the flow separation at the left lower arm and left upper leg affected the left upper arm and left lower leg, respectively" [10]. In clearer words, the forward component of a leg or arm causes separation, in which the back component of the arm or leg is immersed, which aligns with the observations drawn from Figure 2.10. This is visible especially well on the bottom right detail of Figure 2.11, where the calf of the runner has a lower than usual frontal pressure.

2.6. Runner's height and tilt effect on drag

Some literature cited in this thesis considered the effect of other factors on the drag experienced by a runner, like height or body tilt. This section goes into detail on their effect on drag.

2.6.1. Height effect

Pecchiari et al. experimentally measured the drag of moving runners in a wind tunnel, with a variation in height between the contestants. Figure 2.12 shows the intermediate results of this study, where the height of the runner squared is highly correlated to the drag, represented here as A_{eff}. This term is defined in Equation 2.5. This equation represents the effective area in terms of drag force, density and velocity. The effective area from this definition is also equal to half of the drag area defined in Equation 2.2.

$$A_{\text{eff}} = \frac{D}{\rho V^2} = \frac{1}{2} \cdot \text{drag area} \tag{2.5}$$

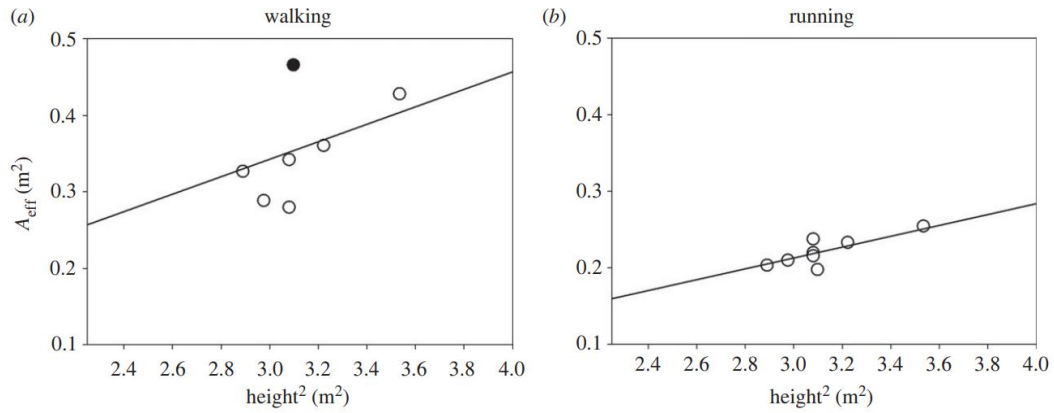

Figure 2.12: Effect of runner's height on the drag area by Pecchiari et al. [11] The black dot is an outlier, which is not considered for the line fit.

Figure 2.12 shows, specifically for running speeds, that the drag experienced by a runner should vary linearly with the height of the runner squared. This fact can be useful for comparing drag areas of different runners in the following study.

2.6.2. Body tilt effect

Kim et al. [10] simulated a static runner model in the takeoff and touchdown phases, with an additional variation in upper body tilt angle, which would be necessary for sprinting acceleration or for running against a headwind. Figure 2.13 shows the results of that study.

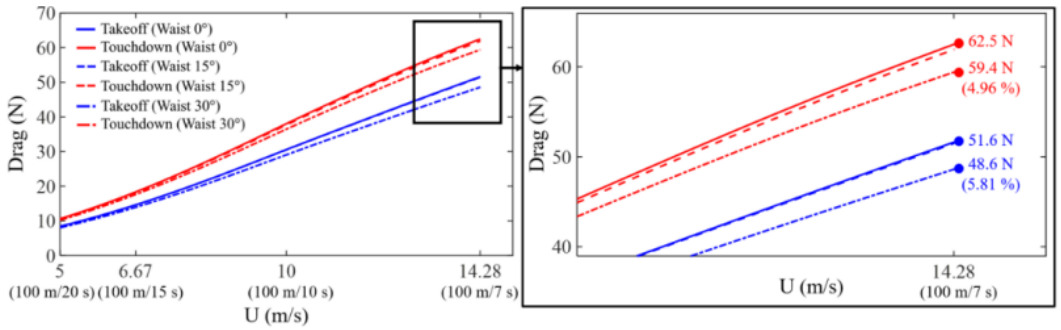

Figure 2.13: Drag of a runner leaning forward at different angles by Kim et al. [10]

At sprinting speeds, which is towards the right of the graphs of Figure 2.13, it is visible that an upper body tilt of 30 degrees decreases aerodynamic drag compared to the standard upright position. A lean of 15 degrees makes very little difference with respect to the upright position. According to Kim et al., the drag coefficient increases with body lean, but the frontal area decreases at a faster rate, therefore a decrease in drag [10].

2.7. Reynolds number effect

Finally, the experimental research of Pecchiari et al. allows for an investigation of running speed on the drag area and therefore also on the drag coefficient of real moving runners, which is described in this section.

Figure 2.14 shows two graphs from their study, for a single runner. The left graph shows the relation of total drag to the running speed, and the right graph shows the relation of effective area to running speed squared. Again, effective area is described by Equation 2.5.

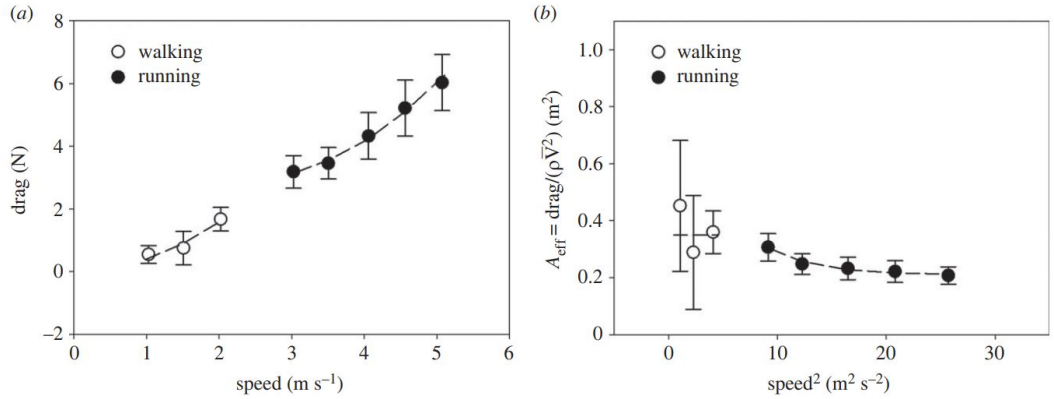

Figure 2.14: Effect of running velocity on drag and drag area by Pecchiari et al. [11]

The left of Figure 2.14 states the obvious: drag increases with running speed.

The more interesting result is on the right graph. For walking speeds there is too much uncertainty to come to any conclusions, but for running in the speed range of $3m/s$ and $5m/s$ (corresponding to speed^2 of 9 to 25 m^2s^{-2}) there is a visible trend. The drag area decreases with running speed, and towards the higher speeds it approaches a lower limit.

It is possible that the right graph in Figure 2.14 follows a similar pattern as Figure 2.1 for cylinder flow, transitioning from subcritical to transcritical flow regimes, except that on a flow around a human body there is no local minimum of drag coefficient around the critical flow regime. Instead, the drag coefficient and therefore also drag area possibly smoothly transition from their subcritical values to their transcritical values in the range between walking and running speeds.

Unfortunately, the graph does not reach professional sprinter speeds of $10m/s$, but assuming that the reasoning in the paragraph above is correct, it can be expected that the trend of the graph continues and at higher speeds the effective area remains constant in the fully developed transcritical flow regime.

However, for any future research investigating the effect of a changing variable on a runner's drag, it would be safest to keep the running speed the same between different runs.

3

Background on particle velocimetry

This chapter delves into the experimental techniques designed to explore the three-dimensional flow patterns surrounding an object. The focus is put on on identifying the methodologies most applicable to the research into running aerodynamics.

Section 3.1 expains the basics of particle velocimetry. Section 3.2 lists the relevant methods of processing in flows with particles. Section 3.3 gives information about the use of helium filled soap bubbles. Section 3.4 introduces the ”Ring of Fire” method. Section 3.5 explains how to measure drag from the flow in the wake of an object using momenum analysis. Lastly, section 3.6 lists the research questions of this thesis.

3.1. Particle velocimetry

Particle Image Velocimetry (PIV) and Particle Tracking Velocimetry (PTV) are flow visualisation methods based on processing images of a moving flow. This section goes deep into details on different aspects to consider when choosing a PIV/PTV experimental setup.

The details of the PIV method are explained well by Raffel et al. [20]. The explanation is supplemented by Figure 3.1. The procedure of performing PIV measurements involves adding tracer particles to the flow and illuminating them with a light source. Different sizes of particles can be used for different scales of experiments. The pulse-like illumination (typically laser or LED) and one or more cameras are synchronised and activated twice in a quick succession to capture the original particles and then the slightly displaced particles. Calibration relates the particle image displacement to the tracer particle displacement and after post-processing, which calculates the local velocity vectors, the data can be visualized as a vector field.

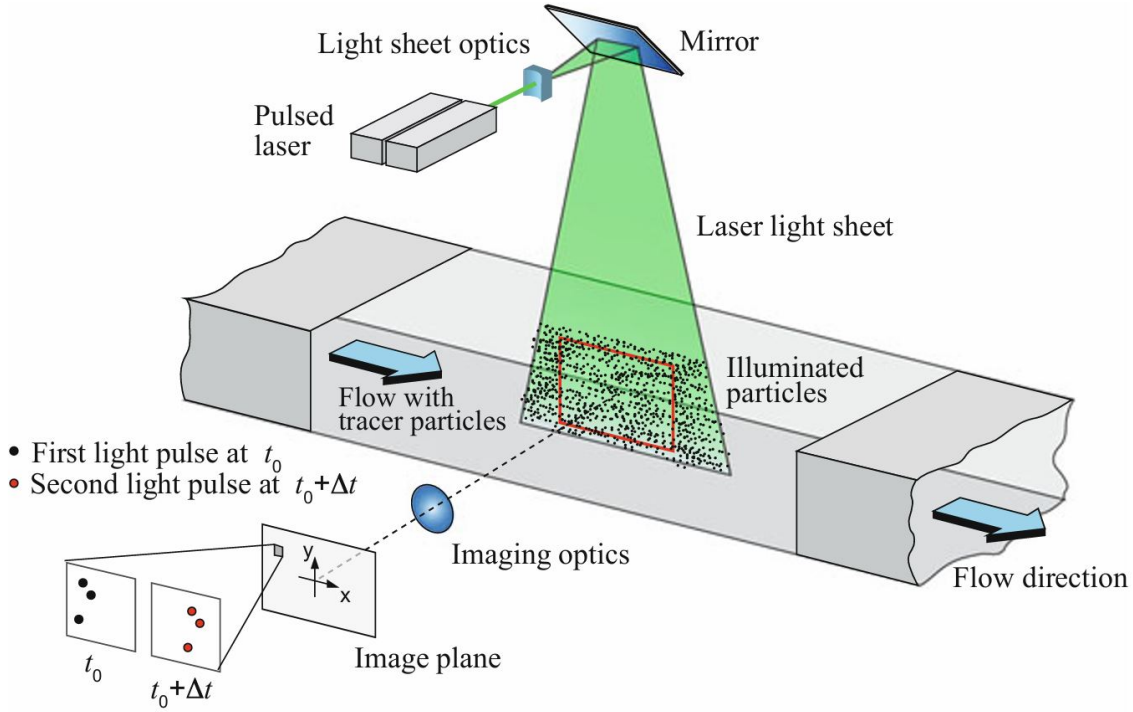

Figure 3.1: Schematic view of the Ring of Fire setup by Raffel et al. [20]

If the illumination plane is perpendicular to the flow and behind the model in a wind tunnel, PIV achieves a similar result to an advanced wake rake system, but with additional benefits, including the fact that that PIV is non-intrusive, is capable of producing results with a high resolution and can capture flow structures over extensive areas. Additionally, the plane of measurement can be placed anywhere, even coinciding with the model, and it can be parallel to the flow, which a wake rake cannot achieve.

As a recent example of the use of this method, Terra et al. [21] conducted a large-scale PIV wind tunnel experiment to measure the time-averaged drag force and flow topology in the wake of a cyclist.

3.2. Processing methods

This subsection lists the different types of processing in PIV measurements and how they relate to the number of cameras used.

3.2.1. Standard PIV

The standard, most simple PIV setup is as shown in Figure 3.1. There is only one camera collecting images of the desired field of view, preferably at an angle perpendicular to the illumination plane.

This method can only output 2 component vectors on a 2-dimensional plane. The out-of-plane velocity component is not determined, and the in-plane components suffer from an irreversible error caused by the perspective transformation [20].

The benefit of this method is its simplicity, and the obvious drawback is the limit of 2 dimensions.

3.2.2. Stereo-PIV

Stereo-PIV is the simplest PIV method used to capture the out-of-plane velocity vector and typically makes use of 2 cameras with an angular separation to achieve that [20]. This PIV method is limited to just a 2-dimensional measurement plane.

3.2.3. Tomo-PIV

Tomographic PIV differs from stereoscopic PIV in the fact that it is able to measure velocity fields in a thicker measurement volume, as opposed to only a measurement plane. This allows for the collection

of 3 dimensional, 3 component velocity information.

A Tomo-PIV setup typically makes use of 3 to 6 cameras and a thicker illumination sheet, requiring higher illumination system power to achieve a comparable brightness. A calibration procedure is used to determine the relationship between the three-dimensional coordinates and their projections onto the image planes. The use of more cameras increases measurement accuracy and allows for more particles per pixel, meaning a higher particle density can be used in the same measurement volume [20]. The general flow chart of the Tomo-PIV technique can be seen in Figure 3.2.

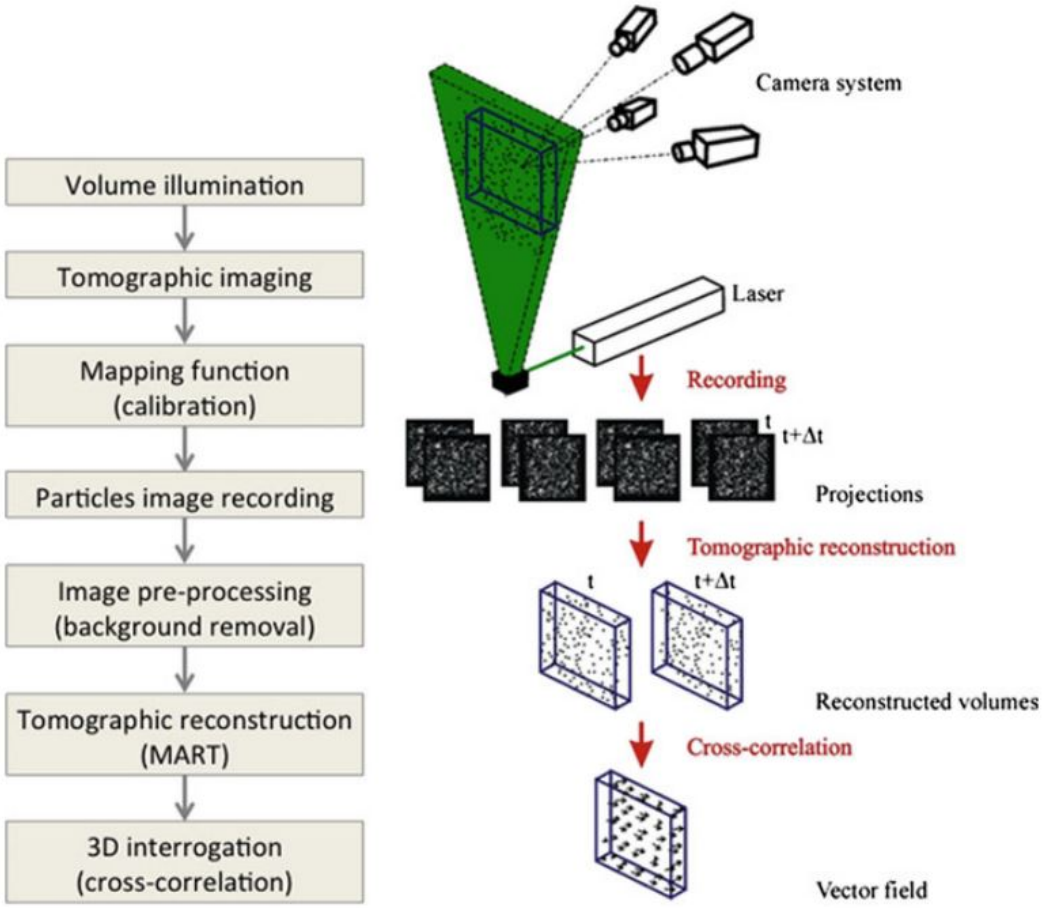

Figure 3.2: Tomo-PIV flowchart and schematic illustration by Raffel et al. [20]

3.2.4. PTV and "Shake the Box"

According to Raffel et al., particle tracking velocimetry (PTV) methods can offer better spatial resolution and measurement accuracy than the correlation based PIV techniques discussed previously. ”If strong velocity gradients are present in the flow, PIV results are biased in 2D as well as 3D” [20]. Gradient based quantities such as the vorticity are affected by this the most.

Since the flow in the near wake of a runner is highly chaotic, with strong vorticity and velocity gradients, PTV processing might be more useful for that application than the PIV techniques discussed before.

However, according to Raffel et al., 3D PTV as introduced in the early 1990s uses a triangulation method based on epipolar lines to determine the volumetric distribution of particles at each time step. This approach is most effective for processing images with a low particle image density. In contrast, the ”Shake the Box” (STB) method addresses the challenges posed by high particle image density by strongly integrating temporal information into the particle reconstruction process and employing

sophisticated triangulation algorithms [20].

Schanz et al. introduced and tested the STB method. They also compared it to results of other methods, including tomographic PIV and conventional PTV. They found that for STB, ”Noise-free images with a particle image density of 0.125 ppp could be successfully evaluated. After a convergence phase, nearly full completeness (>99.5 % of identified particles at 0.125 ppp), virtually no ghost particles (<0.04 % false particles) and high accuracy (average position error of 0.018 px) were attained” [22].

STB was able to handle particle concentrations at least an order of magnitude higher than the older, conventional 3D PTV techniques. Tomographic reconstruction on the other hand was able to process particle image densities equally high as STB, but the processing resulted in lower quality, including ”much higher ghost particle occurrence (>250 % false particles at 0.125 ppp) and a significantly lower accuracy (average position error of 0.3 px)” [22].

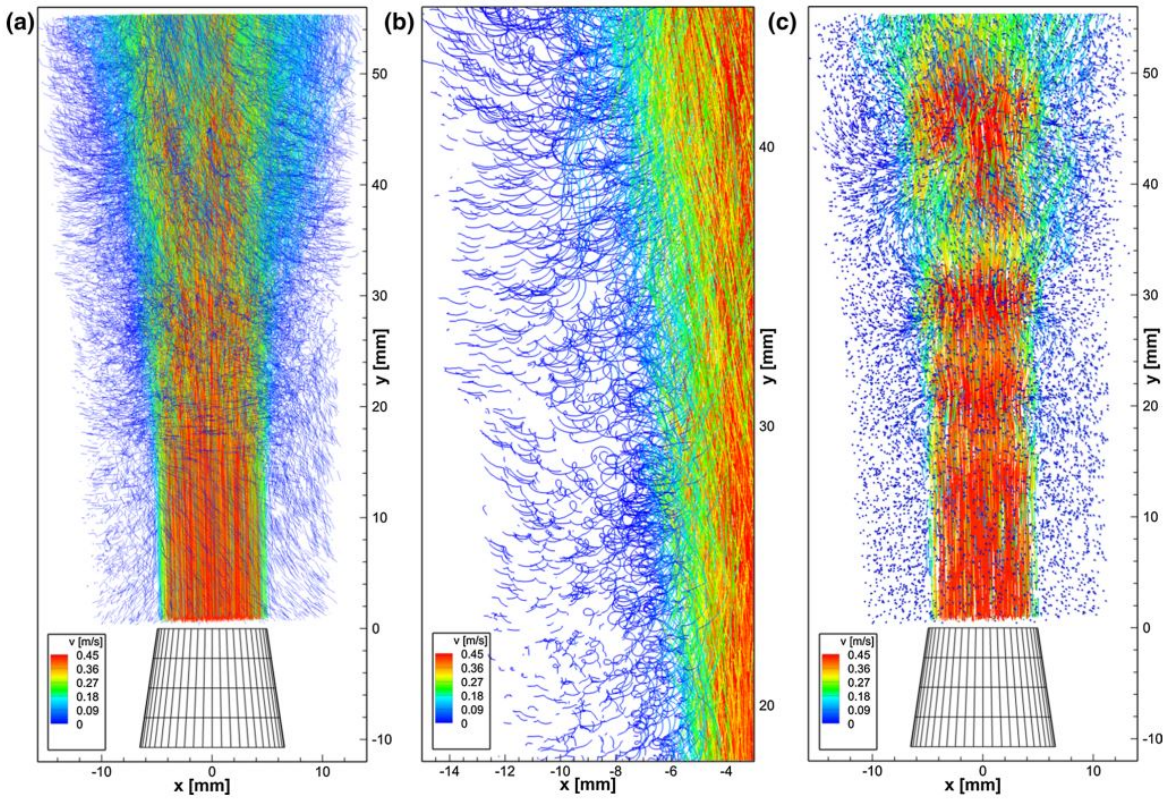

Figure 3.3: STB result for a water jet by Schanz et al. [22]. a) particle tracks using 100 images, b) zoomed in detail, c) shorter particle tracks using 15 images. Particle tracks are color coded with y-direction velocity.

Figure 3.3 shows an example result of STB processing. The STB method is particularly advantageous for visually inspecting flow structures due to its ability to provide high-resolution, three-dimensional visualizations of particle trajectories. By accurately tracking a large number of particles over time, it generates detailed, continuous representations of flow patterns in a 3D volume, like on the left of Figure 3.3. This allows for clear and accurate high resolution visualizations of complex and dynamic flows like a wake of a runner, which might be more difficult using other previously mentioned PIV methods.

3.3. Large-Scale PIV

One of the difficulties with PIV measurements in the past has been the limited measurement volume. Scarano states that the measurement volume in PIV is typically limited to a few hundred cubic centimeters [23]. This restricts tomographic PIV use in fields like sports aerodynamics, where regions of interest can be in the order of meters.

Caridi et al. explain that the main issue is the limited laser pulse energy over a large volume and the

small optical aperture needed for in-focus imaging [12]. The light collected by cameras for each particle simply reduces with an increasing measurement area. Melling et al. concluded that using larger tracer particles increases scattered intensity but increases particle inertia, which reduces the ability of the particles to follow high accelerations of the flow [24].

Recently, Bosbach et al. [25] developed a way to produce helium filled soap bubbles (HFSB). Scarano later showed that sub-millimeter (HFSB) provide higher scattered intensity than standard micron sized bubbles and they keep good tracing fidelity, with a time response of 10–30 μs, making them suitable for quantitative studies in low-speed aerodynamics [26].

Terra et al. [21] investigated the feasibility of large-scale PIV wake rake measurements to determine drag on a three-dimensional human-scale wind tunnel model. The velocity field was successfully retrieved in a 1.6 m^2 volume.

3.4. On site PIV: Ring of Fire

PIV measurements can also be performed on site. The Ring of Fire measurement method does not requre a wind tunnel. Instead, the air and the seeding are stationary, and the measured object travels through them.

3.4.1. Recent developments

Recent uses include Terra et al. for measuring the drag of a transiting sphere [18], and Spoelstra et al., who investigated the wake behind cyclists [13] and ice skaters [14]. Figure 3.4 shows one of the setups for measuring the drag of drafting cyclists.

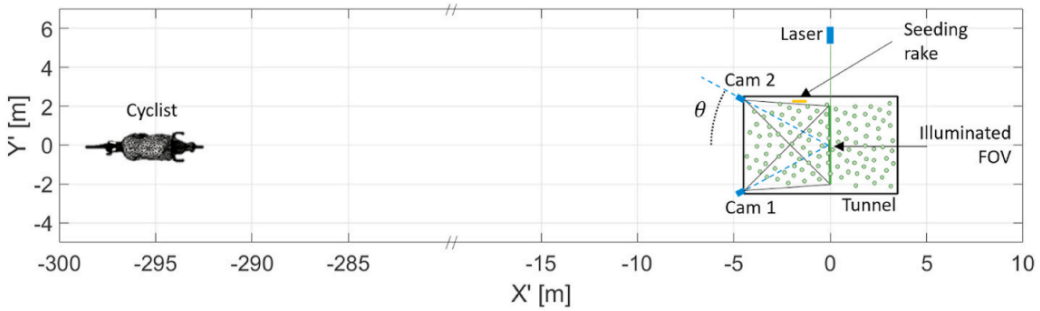

Figure 3.4: Schematic view of the Ring of Fire setup for cyclist measurements by Spoelstra et al. [13]

In the measurement shown in Figure 3.4, there is a long track for a cyclist to accelerate on, to arrive at the measurement plane with a constant speed. Two cameras are used to capture images. The seeding is created by a seeding rack inside of a tent and stored in a tent. The illumination is provided by by a laser from the side. The tent front and back walls are opened like curtains just before the passage of the cyclist to minimise the loss of seeding to the outside environment.

3.4.2. Seeding injection for Ring of Fire

The recent Ring of Fire research on sports aerodynamics of Spoelstra et al. [13], [14] used a sturdy yet inefficient system for bubble distribution in the domain. The helium filled soap bubbles were injected into the domain by a seeding rake developed for wind tunnel use. The current bubble injection method for Ring of Fire requires a large tent that accumulates the bubbles in a large volume, which is then opened for an athlete to pass through.

A seeding injection system tailored for Ring of Fire needs can be optimised for its own needs. The existing seeding rake has 204 orifices for bubble injection, but since the ring of fire is a static setup with no wind tunnel flow, the bubbles can be accumulated in the measurement domain over time and fewer seeding nozzles should be needed.

One alternative is a new, more efficient but also more sensitive method for seeding injection, which can be developed further in the future into a mobile measurement base. The main principle of the new

system is the accumulation of bubbles in a large cylinder, and pushing them out with a piston through a perforated long tube that wraps around the desired domain, releasing bubbles uniformly, right where they are needed. The system operates on only one nozzle, as opposed to the current 264 nozzles. More on this system is available in Appendix A.

3.5. Drag evaluation by momentum analysis

The method for drag evaluation through the Ring of Fire has been developed by Spoelstra et al. [27] and Terra et al. [18].

The instantaneous drag force $D(t)$ is calculated by the conservation of momentum in a control volume around a runner. The runner is assumed to move at constant speed u_r with respect to the ground. The air motion in the environment prior to the passage is denoted as u_1 and the pressure as p_1. After the passage, the wake's velocity field is denoted as u_2 and its pressure field as p_2. S_1 and S_2 are chosen such that the mass is conserved. Note that p_1 is integrated over S_2 and not S_1 to account for the pressure over the sides of the boundary.

$$D(t) = \underbrace{\rho \iint_{S_1} (u_1 - u_r)^2 \, dS - \rho \iint_{S_2} (u_2 - u_r)^2 \, dS}_{\text{Momentum term}} + \underbrace{\iint_{S_2} p_1 \, dS - \iint_{S_2} p_2 \, dS}_{\text{Pressure term}} \tag{3.1}$$

Where ρ is the air density. According to Terra et al. [18] for an individual body passing through the domain, S_2 can be chosen far in the wake that the pressure term is negligible, but close enough that the mamentum term does not start decreasing due to viscosity.

The importance of the drag components for a sphere can be seen in Figure 3.5. Since a runner is also a bluff body, it can be reasoned that the graph of drag components for a runner would have a similar structure to the graph of the sphere.

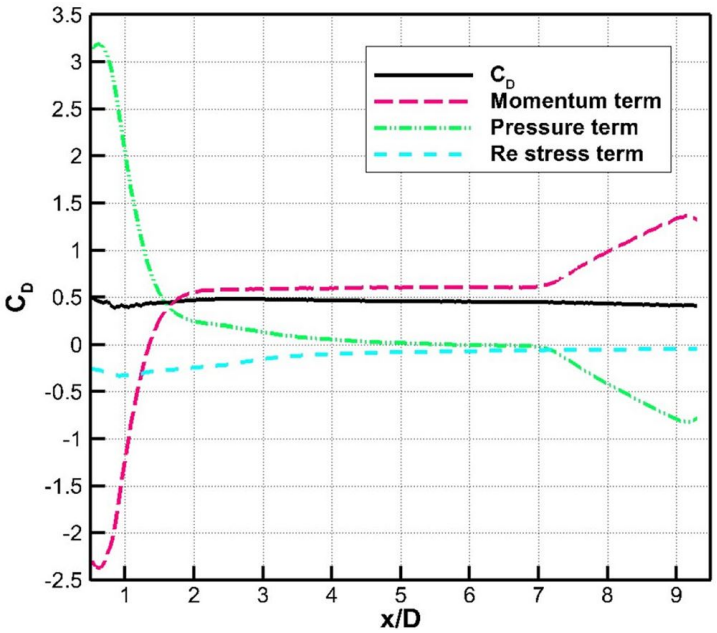

Figure 3.5: The sphere drag components varying with time from the study of Terra et al. [18]

The drag coefficient right behind the transiting object has a high uncertainty, because the pressure term of the drag equation is in its full effect. The pressure term decays quickly and vanishes at around $x/D = 5$.

The momentum term is negative at first, which can be thought of as thrust. This thrust is caused by the reverse flow in the recirculation region and the accelerated flow around the sphere. [18]

The Reynolds stress term is smaller than the other two, but it is still significant and ignoring it could cause significant errors, as it decays more slowly than the pressure term.

The total drag coefficient reaches a maximum at around 2-3 diameters behind the sphere, and then decays slowly as viscosity slows down the wake. The drag estimation then becomes lower with increasing distance from the sphere.

3.6. Research questions

Based on the literature study, this thesis has one main research question, which can be split into subquestions, as follows:

What are the general characteristics of airflow in the wake of a real moving sprinter?

- What is the evolution of the flow velocity component in the direction of the runner?
- Where are the main vorticity structures around the runner's body?
- How does the lateral velocity of the flow depend on the phase of the runner's movement?
- What is the drag area of the runner?

4

Experimental Setup

This chapter presents the experimental setup used in the experiment, including the location, equipment placement and procedures

Section 4.1 introduces the athletes that participated in the experiments and the garments they wore. Section 4.2 presents the hardware used in the experimental setup and the reasoning behind its positioning. Section 4.3 explains the calibration procedures and the theory behind them. Section 4.4 outlines the experimental protocol. Lastly, section 4.5 refers the reader to the test matrix, which is shown in Appendix C.

4.1. Test objects

4.1.1. Runners

The runners were 9 junior athletes from a local sports club. For privacy and simplicity, they were named with numbers from 1 to 9 and their height has been anonymized by indicating a range.

On the last day of the experiments, when the experimental setup was finalised, athletes 7, 8 and 9 were present. Their genders and heights are given in Table 4.1. They were each asked to sprint through an 80 meter long track 10 times, maintaining a constant speed of 8 m/s while passing through the measurement setup. The three runners alternated so that they can get sufficient rest between their runs, and they were asked to change between 2 types of garments. More information on all the runs can be found in the test matrix in Appendix C.

Table 4.1: Athlete data

athlete number	gender	height [cm]
7	female	165-170
8	female	165-170
9	male	180-185

4.1.2. Garments

Two types of garments were worn for the experiments:

- Sprint suit - a standard tight suit with short sleeves.
- Aero suit - a long-sleeved suit with circular vortex generators in separation-prone places, like shoulders or hips

4.2. Hardware setup for Ring of Fire

This section explains the physical setup of the RIng of Fire system to provide a good understaning of the experiment's design. To facilitate the understanding of the following sections, Figure 4.1 presents

a picture of the entire experimental setup.

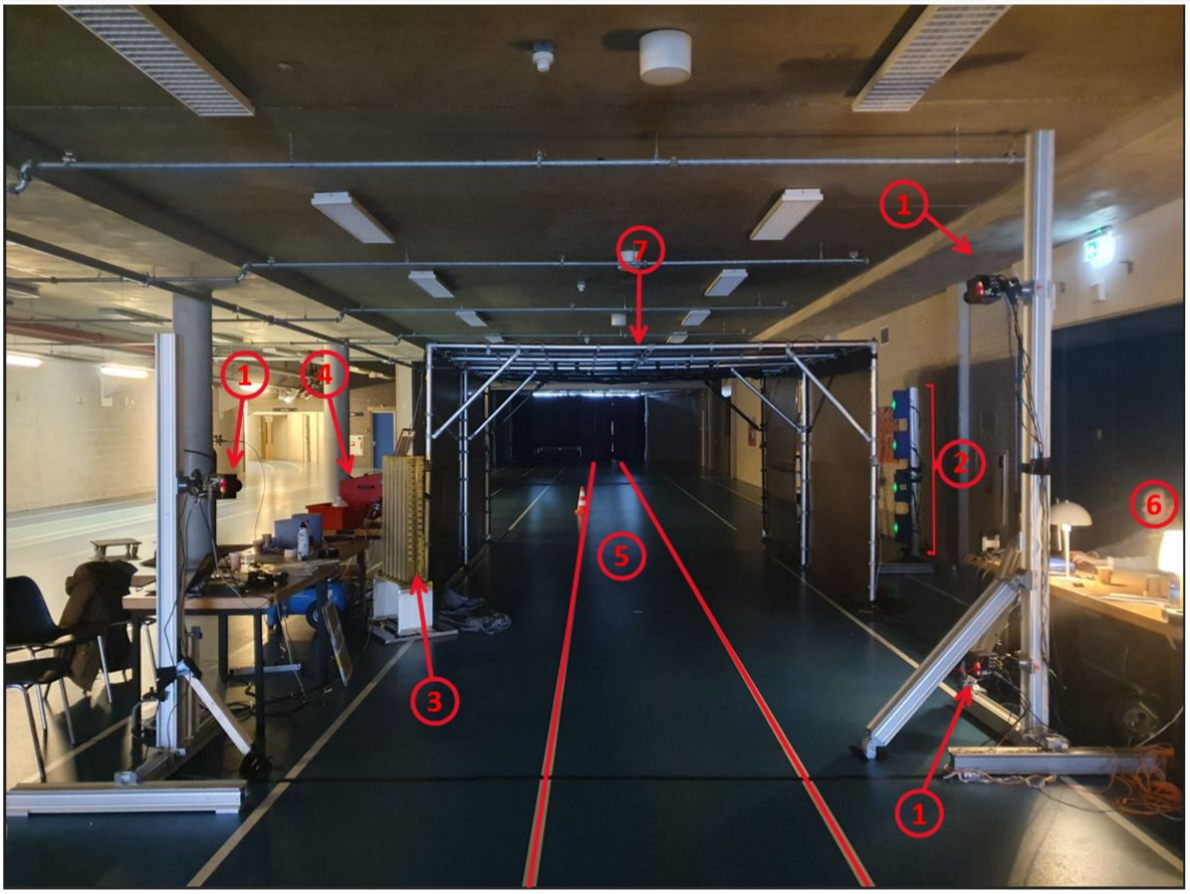

Figure 4.1: Picture of the Ring of Fire setup: (1) three cameras, (2) four LED's, (3) seeding rack, (4) FSU and pressure generator, (5) running track between white lines, (6) data acquisition computer and camera controller, (7) tunnel

4.2.1. Test facility

The experiments were performed at Omnisport Apeldoorn, located at De Voorwaarts 55, 7321 MA, Apeldoorn, Netherlands. The facility includes an indoor oval running track and next to it a short straight sprint track. The latter was selected as the experiment location because of its straightness and large empty area for equipment. The athletics track consisted of six lanes of 1.2m wide each. The total length of the track lanes was 80m and the measurement equipment was set up roughly in the middle of that length to allow sufficient space for the runners to accelerate to the required speed, and then to safely decelerate.

For the time of measurements, the lamps and ventilation system in the hall were switched off to allow for more contrast between the tracer particles and the background, and to prevent any wind through the measurement plane which could influence the momentum balance. The light from the lamps of the adjacent track ensured that the runners had enough brightness to see the running track.

4.2.2. Tunnel structure

A tunnel made of a metal pipe frame and wooden sheet walls, with a height of $2.5m$, width of $4m$ and length of $5m$ makes sure that the seeding injected into the measurement domain remains where it is supposed to be. The measurement domain is placed roughly in the middle of the tunnel's depth, in the middle of the tunnel's width, and touching the floor.

A cut-out in the right side of the tunnel allows the LED's light to pass into the measurement volume from outside of the tunnel. The cut-out also acts as a light stop, allowing light to only pass into the required volume, and darkening the volume in front of and behind the measurement volume. The reflective

metal pipes and white track lines that appear in the measurement plane of any camera's view were covered with black duct tape to increase the contrast between the seeding and the background.

4.2.3. Illumination

To illumiante the measurement domain, 4 LED arrays (Flash Light 300 supplied by LaVision) were mounted equidistantly on a vertical beam, as can be seen on the right of Figure 4.1.

The illumination pattern is shown in Figure 4.2. There are dark areas between the LED arrays, but at a high enough distance from the light source, the light beams expand enough that the whole height of the measurement domain can be covered.

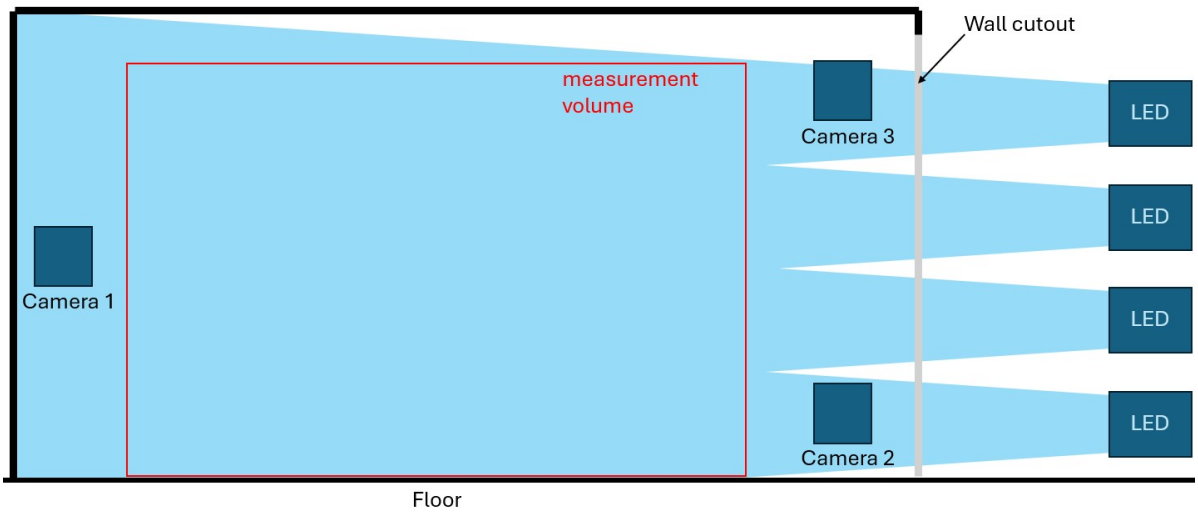

Figure 4.2: Front view sketch of the measurement plane and the illumination scheme

Similarly, in Figure 4.3, the light beam is narrower than the measurement depth close to the light source, but at some distance the light beam becomes wide enough to encapsulate the entire measurement volume.

To achieve the required thickness and uniformity of the illumination, the light source had to be placed outside of the tunnel, and a vertical hole was cut out in the wall of the tunnel, allowing a narrow beam of light in, but blocking any unnecessary light from entering and spreading to the sides. The hole cutout can be seen most clearly in Figure 4.4. The cutout was covered with transparent plastic packaging foil to prevent air from passing through.

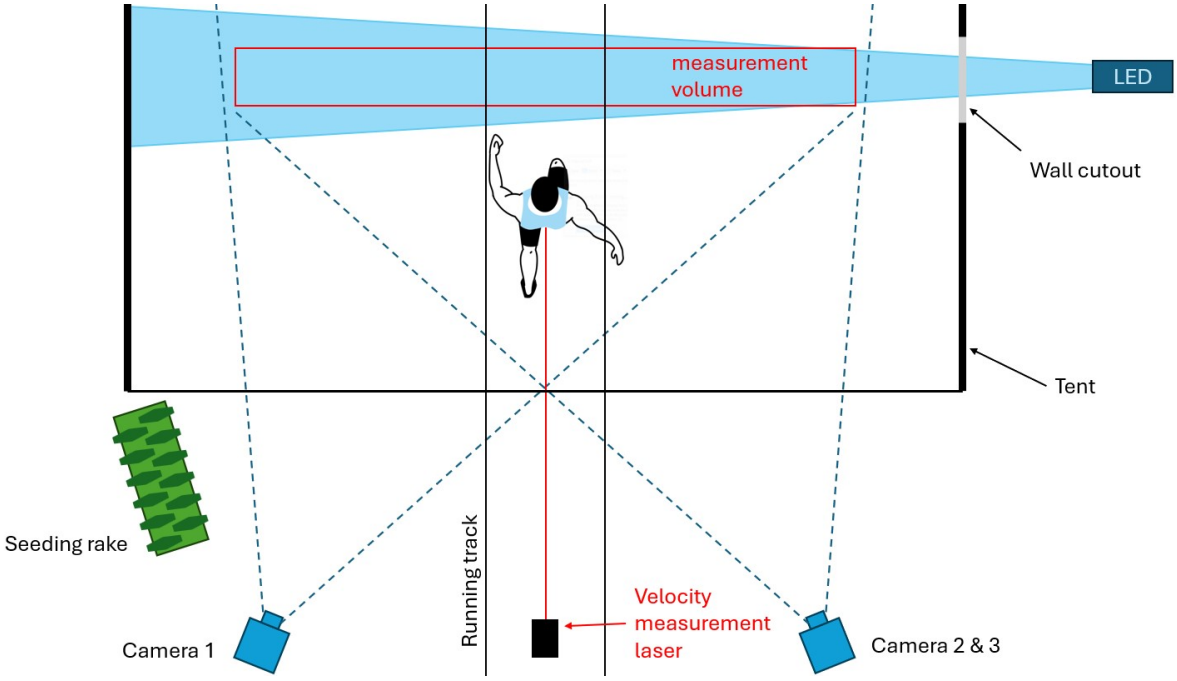

Figure 4.3: Top view sketch of the Ring of Fire hardware setup.

There were 2 attempts to further improve the illumination intensity and uniformity within the measurement domain:

- 1st attempt - put spherical Fresnel lenses at the edge of the measurement domain. This was successful at converging the light and increasing illumination intensity at the left side of the domain, but the focal point fell inside of the measurement domain, causing individual beams from each diode with dark areas between them. It was decided that the lack of uniformity is suboptimal for particle tracking.
- 2nd attempt - put a long vertical mirror on the left side of the tunnel to reflect the light back at the source. This increased the intensity of light at the left side as intended, as the intensity of available light was doubled at the mirror location, and illumiantion intensity was not sacrificed this time. However, a different problem prevented this solution from working: The original light beam, when reflected by the mirror, continued expanding in thickness after being reflected, causing an unacceptably large illumination thickness, illuminating unwanted particles outside of the measurement domain.

4.2.4. Imaging system

The cameras used for this experiment were supplied by LaVision. The model used was Photron MINI AX 100 (CMOS, 1024 × 1024 pixels, pixel pitch of 20 μm, 12 bits), with Nikon 50 mm lenses. The f-stop setting on the lens was 5.6.

The cameras covered the measurement domain with size 2.7m x 2.7m with depth of 0.3m, resulting in a magnification factor of 0.008. The digital image resolution was 2.51mm/px.

The cameras and LED arrays were synchronised by the LaVision High Speed Controller: PTUX Photron mini. The acquisition frequency was 400 Hz, with an illumination pulse duration of 250μs. The images were sent to an acqiusituion PC and copied to external hard disks for backup.

The angular separation between the cameras needed to be large enough within the available space. The schematic of the placement is shown in Figure 4.3 and Figure 4.2, and the real positions of the cameras are shown in Figure 4.1.

4.2.5. Seeding

Helium Filled Soap Bubbles (HFSB) were used as the tracer particles of the system, for reasons explained in section 3.3. The target particle concentration in the domain was 0.02-0.035 particles per pixel, similarly to the water jet experiment of Schanz et al. [22]. The seeding concentration during a run can be seen in Figure 4.4.

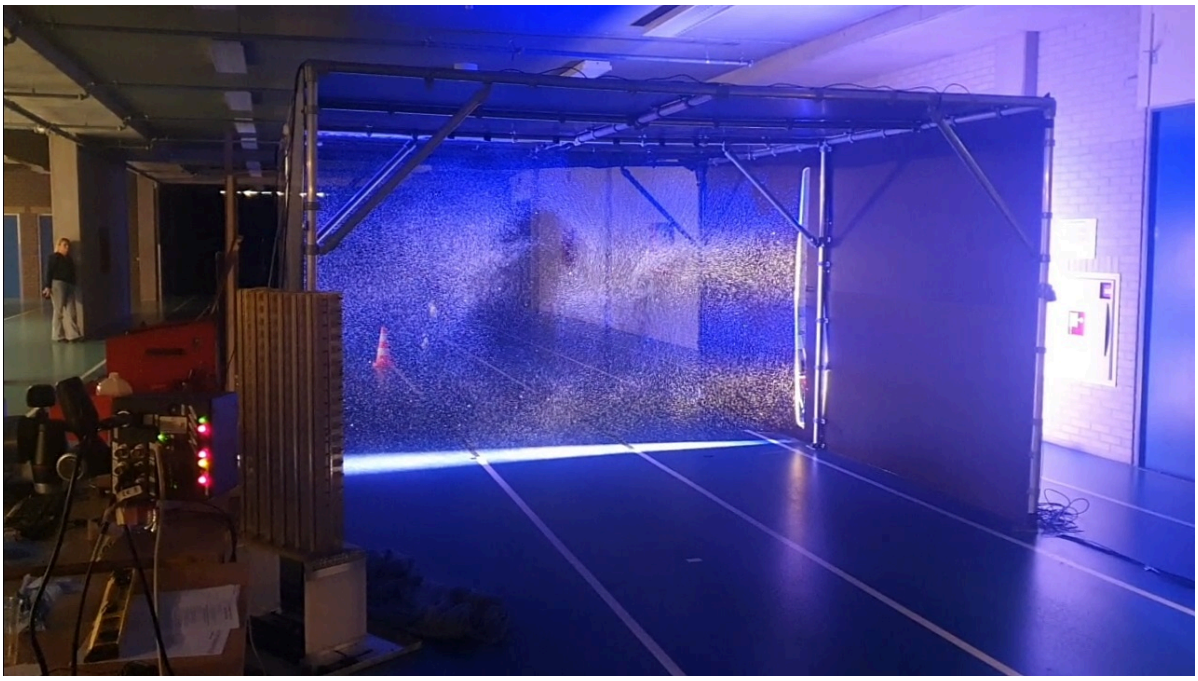

Figure 4.4: Picture of the Ring of Fire setup working during the experiment, after the passage of an athlete

Originally, the seeding was supposed to be provided by a piston-cylinder system through a pipe that wraps around the measurement domain. However, that system did not provide enough seeding in the testing phase in the experiment location, so it was replaced with the backup working solution. More about the piston-cylinder system is explained in Appendix A.

The seeding rake that was used during the experiment as a backup solution is a set of 12 half-wings, with 17 seeding-generating nozzles on each wing, resulting in 204 total nozzles. A picture of the rake is shown in Figure 4.5. During the experiment, around half of the nozzles worked properly and the other half were stuck, so in the end around 100 nozzles were providing seeding.

The rake has been developed for wind tunnel use, so it generates a high concentration of bubbles, to be spread into the wind tunnel test section by the free flow. The concentration created in stationary air is too high for PTV measurements, but that concentration can be manually spread around the domain by the experiment operator, resulting in an optimal concentration.

Figure 4.5: The seeding rake used for the experiments

The seeding rake is supplied pressurised air, helium and soap through a custom Fluid Supply Unit.

4.2.6. Triggering hardware

A laser photodetector was connected to the LaVision High Speed Controller in order to start the acquisition of each run at the same location of the approaching runner. However, the system stopped working when the photodetector was connected, so the experiment was conducted with manual triggering by pressing a button on the acquisition computer when a runner was approaching.

With this in mind, the largest possible acquisition of 5000 images was chosen to maximise the available data, and after every run the data was trimmed to only what is necessary, which is 350 frames before passage to catch the freestream condition without the runner blocking the view of any camera, and 650 frames after the passage, to save the wake up to around 10m behind the runner.

After acquisiton, the passage frame had to be found and a range of frames manually saved, which took multiple minutes and sometimes needed to be redone multiple times due to DaVis bugs, so the saving of data was the rate limiting step for the experiment.

4.2.7. Velocity measurement

The velocity of each runner was measured using a laser system aligned with the running track, pointed at the runner's waist horizontally from behind. The laser system used for this is called LAVEG from Jenoptik and it is shown in Figure 4.6. It has been used in the study of Ashton et al. where the uncertainty of the velocity measurement varied between 8% and 13% of measured velocity [28].

Figure 4.6: The laser used for measuring athlete velocity

4.3. Calibration

For the system to work correctly, it needs to be calibrated to the current environment. This comes in 2 steps. First, the view seen by the cameras must be calibrated to the geometry of the measurement domain, which is done by the geometrical calibration. Secondly, the images of particles taken by the cameras must be calibrated to assure correct particle identification in later steps.

4.3.1. Geometrical calibration

The geometrical calibration is necessary whenever it is expected that any of the cameras have moved with respect to the measurement domain. Therefore, it should be done every morning in case someone bumped or moved any part of the experimental setup.

To perform a calibration, a wooden calibration plate with known dimensions and known locations of markers is placed in the measurement plane at a known position. The cameras take pictures of the calibration plate, which is shown in Figure 4.7. Then, in the virtual space, the program creates a coordinate system with an origin at the chosen point on the calibration plate, and scales the distances in all the directions to match the physical dimensionsions of the calibration plate.

Figure 4.7: Calibration plate

4.3.2. Volume self calibration

The purpose of Volume self-calibration is to remove any residual calibration disparities using recorded particle images. The information in this section is taken from [29].

Volume self-calibration requires two steps: calculation of the disparity vector map and correction of the calibration (mapping function)

The disparity vectors form when the lines of sight of the cameras on a particle do not all intersect at 1 point where the particle is. A best-guess particle position is then formed by all the cameras and each camera therefore shifts a particle pixel on its sensor by a small distance, so that all the lines of sight intersect. The disparity vector is then the distance between the particle positions on the sensor and the back projected positions, as seen in Figure 4.8, where the detected particle positions are marked in orange and the back projected positions are marked in blue.

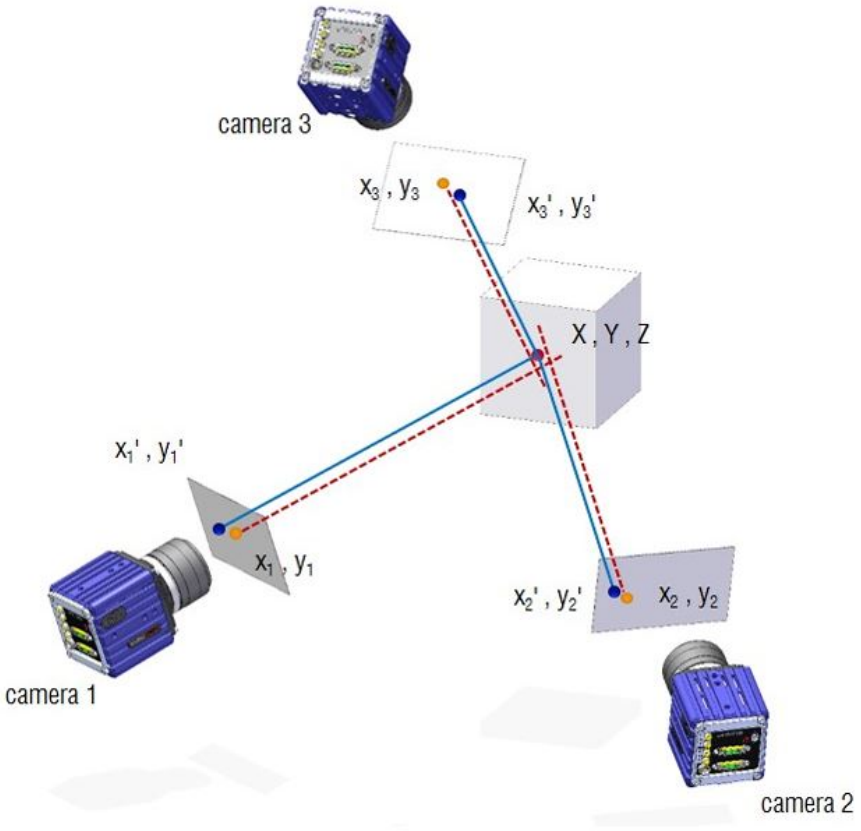

Figure 4.8: Visualisation of disparity vectors from [29]

The disparity vectors are calculated for each particle. Then, the measurement volume is divided into many subvolumes. Within one subvolume, the disparity vectors of all the local particles are combined and this information is used to improve the mapping function for that region.

The calculation of the disparity vector map and correction of the mapping function can be repeated multiple times to converge to a remaining disparity below 0.1 voxel in all sub volumes.

Lastly, an optical transfer function is calculated, and it can be used for the ”Shake-the-Box” processing later, which will be explained in section 5.2.

4.4. Experimental protocol

The protocol for the experiment is outlined here, starting from the beginning of the day.

- Set up all equipment as described before in this chapter
- Perform the camera brightness calibration using an internal shutter.
- Perform the geometric calibration as explained in subsection 4.3.1
- Perform test runs to make sure the equipment works correctly
- On data from test runs, perform a volume self calibration, as explained in subsection 4.3.2
- Athletes warm up
- Perform all runs planned for ther day:
  - Release seeding from the rake with LED on, until the amount of seeding looks sufficient
  - Stop the Fluid Supply unit

  - Manually spread the seeding to all corners of the tent, making sure a uniform distribution is the result. Wait for seeding to lose any remaining velocity or mixing
  - Athlete runs through the domain in the center of the track while their velocity is measured and cameras record the flow
  - Manually save the data as explained in subsection 4.2.6
- Turn off the Fluid Supply Unit
- Back up collected data on 2 hard disks
- Turn off all other equipment

4.5. Test matrix

The test matrix for the last day of the experiments is presented in Appendix C. Only the last day is presented because that is when the experimental setup was finalised and only this data is considered for analysis.

5

Data Reduction and Analysis

This chapter explains the reduction of the colledted data and introduces methods for data analysis that will be used in chapter 6.

Section 5.1 reduces the amount of analysed runs. Section 5.2 presents the settings used in the PIV raw data processing and shows example intermediate results. Section 5.3 introduces visual analysis methods that are necessary to obtain the qualitative results of chapter 6. Section 5.4 shows the method used for averaging the flow field from multiple runs. Section 5.5 explains the method used for obtaining the drag of the athletes. Finally, section 5.6 quantifies the uncertainty of the measured velocity fields.

5.1. Data selection

To put the focus on the depth of the flow analysis, and not on the high amount of runs that can be analysed, the individual analysis has been reduced to four runs, all collected on one day, with one setup, one athlete and one type of garment. Athlete 7 was chosen because of the consistent running technique and similar run phase between different passages. The athlete was wearing the sprint garment in all those runs. Table 5.1 summarises which runs have been chosen for the individual analysis and any relevant information about them. Runs A, B, C and D correspond to run numbers 63, 66, 81 and 84 in the test matrix shown in Appendix C.

Table 5.1: Summary of the individually analysed runs, in chronological order

Given report name	phase during passage	Running velocity [m/s]
A	almost landing on right foot	7.8
B	flight, right foot forward	7.6
C	almost landing on right foot	7.9
D	flight, right foot forward	8.0

5.2. PIV data processing

To obtain planes of velocity data from raw images of the cameras, multiple steps need to be performed. They are all explained in this section.

5.2.1. Subtract time filter

Firstly, the background light is reduced by the ”subtract time filter” function. It removes the minimum light intensity of each pixel from a set of 31 consecutive images. The effect is that the stationary background becomes dark and the moving particles remain bright. This increases the signal to noise ratio for the next step. Figure 5.1 shows the effect of the operation on a raw image.

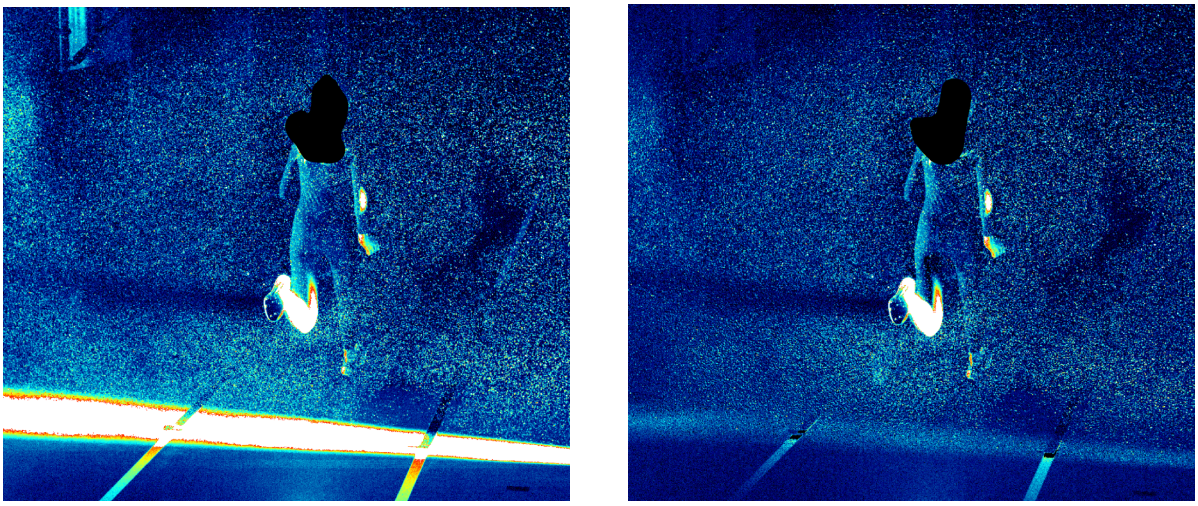

(a) Raw image

(b) Image after ”subtract time filter” processing

Figure 5.1: The light intensity on the sensor of camera 3 during run A. The light intensity scale is constant between the 2 images and the white color signifies an intensity of over 400 counts.

5.2.2. Shake-the-Box

The ”Shake-the-Box” algorithm identifies three-dimensional positions of particles based on a threshold light intensity and draws particle tracks in time, based on the gradual travel of a particle across consecutive frames. The parameters used in the final processing can be found in Table 5.2. Figure 5.2 shows an example result of the operation.

Table 5.2: Shake-the-Box parameters for processing

Parameter	**Value**
Multi-passes	2
Threshold for 2D particle detection	80 counts
Allowed triangulation error	1 voxel
Vx for tracking	0 ± 5 m/s
Vy for tracking	0 ± 5 m/s
Vz for tracking	-4 ± 6 m/s

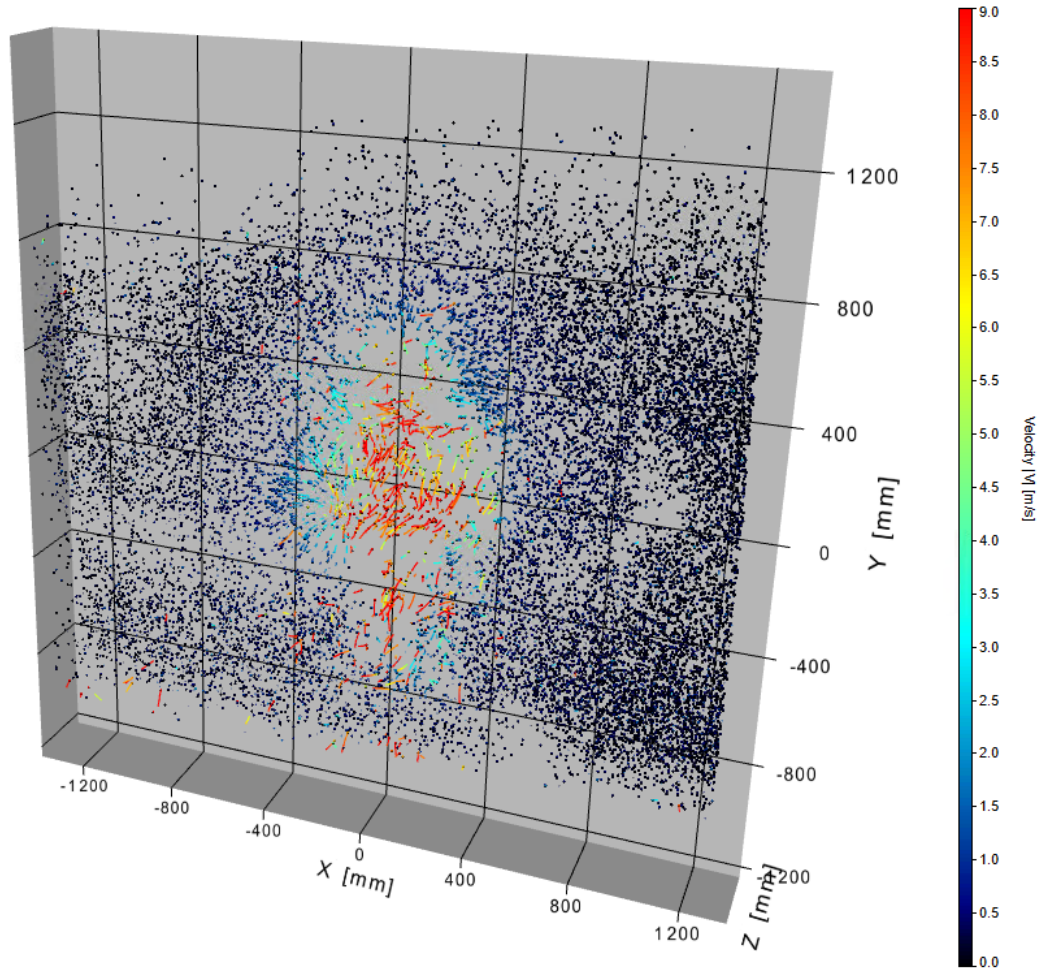

Figure 5.2: Shake-the-Box result for run A, during the frame of passage.

5.2.3. Binning

Lastly, the Particle tracks calculated in the previous step are binned into planes of velocity data. The measurement volume is divided into many subvolumes and in each volume the general velocity is approximated by a second order polynomial fit of the individual particle velocities. Table 5.3 shows the parameters used during the final processing. Figure 5.3 shows an example binning of the set of particles from Figure 5.2.

The Binned image can display many different variables, including all velocity components and vorticity values. The image can also be further modified to crop the data and to shift the coordinate system, as explained in section 5.3.

Table 5.3: Binning parameters for processing

Parameter	**Value**
Subvolume size (digital units)	64x64x64 voxel
Subvolume size (physical units)	160x160x160 mm
Subvolume Overlap	75%
Filter length	5 time steps

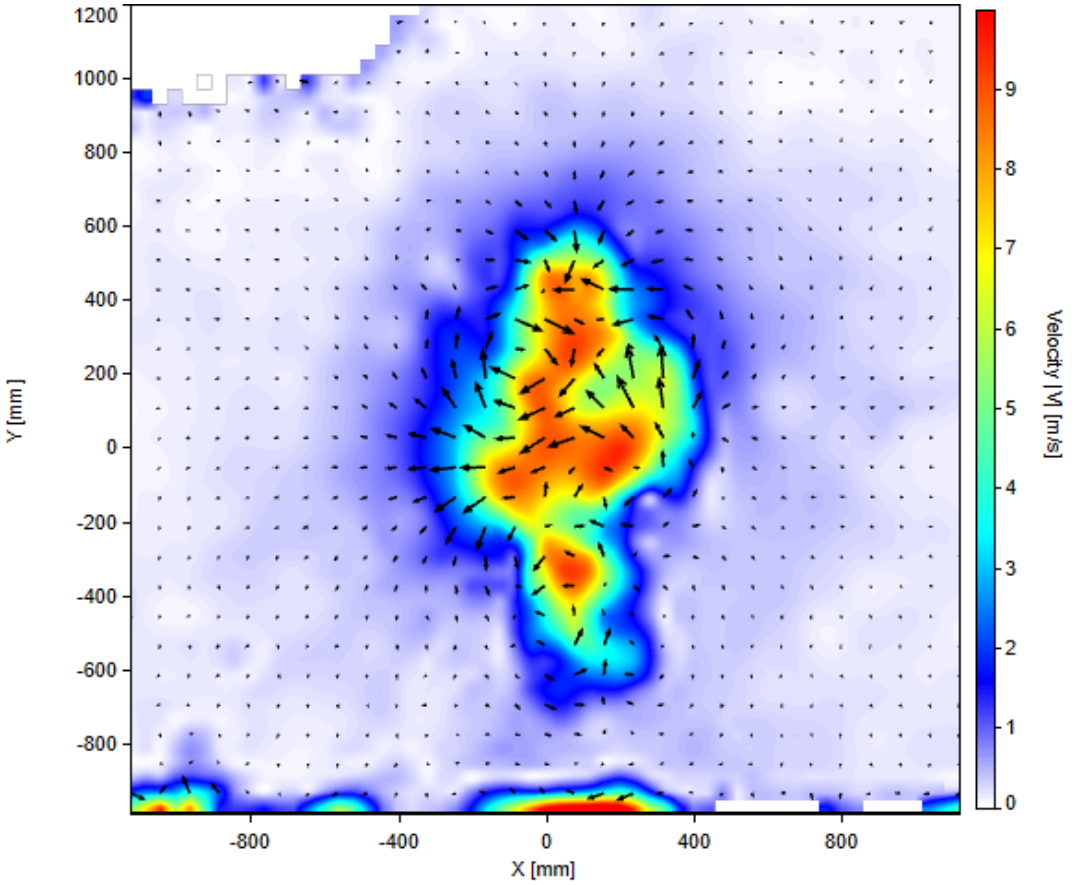

Figure 5.3: Binning of the set of particles from Figure 5.2, showing the magnitude of the velocity with color, and lateral velocities with vector arrows.

5.3. Visual analysis

To fully understand the vortex structures in this research, the velocity field is analysed in planes perpendicular to the runner's motion. The runner's profile is drawn over the velocity field graphs to understand which body parts are causing the major vorticity, and a general vortex structure common to all the runs is identified.

5.3.1. Reference passage frame

Chapter 6 often refers to a reference frame or passage frame. For consistency, this subsection sets specific criteria for selecting that frame. The frames in the analysis are counted from this frame, and distance behind the runner is also calculated with respect to this frame.

The reference frame of passage is the first frame after the last part of the torso has left the illumination volume. Before this frame some flow fields are incomplete due to reflections, and after this frame, the vector fields of runs A, B, C and D are complete, even in the location where the left leg is still in the illumination plane.

Figure 5.4 shows the reference passage frame for each of the runs individually analysed in this paper. The head has been obscured to maintain privacy. Note that runs A and C are in similar phase to each other, and rund B and D and in a phase similar to each other, but they are in a slightly different phase than runs A and C.

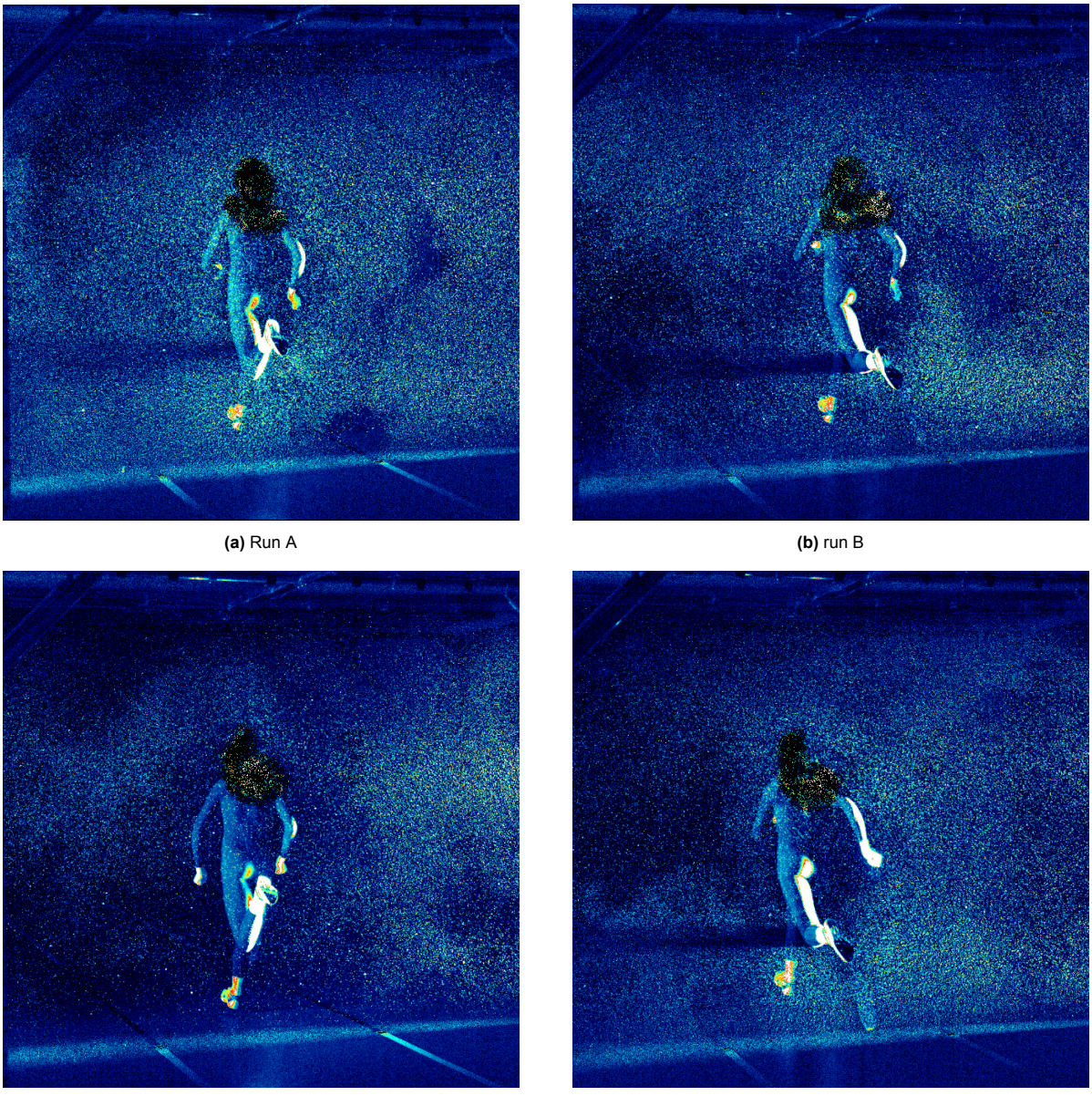

(a) Run A

(b) run B

(c) run C

(d) run D

Figure 5.4: The reference passage frame of runs A, B, C and D

5.3.2. Obtaining the runner's profile

The goal in this subsection is to generate an image of the runner's outline in the position in which they pass through the measurement domain. The vorticity sources will be identified in the close wake, so the runner's position is drawn at the time when they are just exiting the measurement volume. For consistency, the last timeframe when any part of the torso leaves the illumination volume is taken.

Figure 5.5 shows the body of athlete 7 in that exact frame, from the views of cameras 1 and 2. Since Camera 2 is horizontally closer to the running track than camera 1, it produces an image of the runner that is closer to the ideal view from behind, which is not available. At the same time, the view from camera 3 is the same as from camera 2, but from a larger height, which also moves it further from the ideal back view. Therefore, the perspective corrected image from camera 2 is selected for drawing outlines of runners for the purpose of vortex origin identification.

Figure 5.6 shows how the outline of the runner obtained from the relevant frame is transfered to the plane of velocity field.

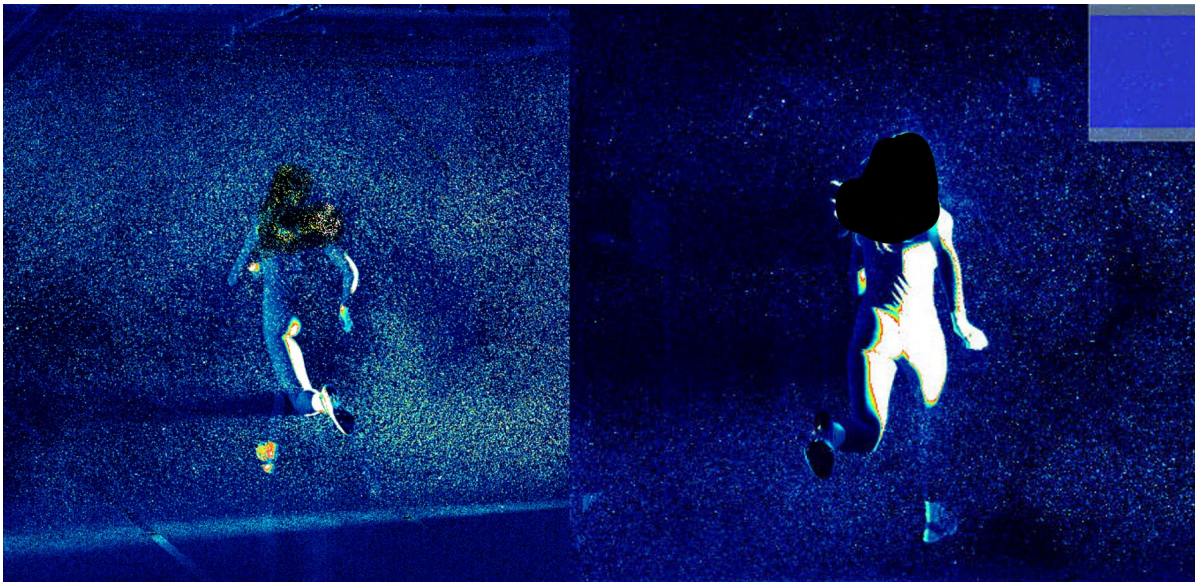

Figure 5.5: Comparison between camera 1 and camera 2 body shapes

A hand drawing of the runner's outline, ignoring the hair shape, is drawn digitally. Even though the image is from the camera closest to the running track, and it is perspective corrected by the software, the runner still seems to be viewed slightly from the side. To account for that, the body parts that pertrude forwards or backwards are additionally corrected during the sketching process. This additional correction can be seen in Figure 5.6, where the backwards pointing left leg has been sketched more towards the right, the forward pointing right foot has been corrected to the left, as was the forward pointing left forearm. The result is the runner's figure with the same height and proportions as the real runner, but seen from an artificial perpendicular view from the back.

Horizontal and vertical lines denoting the position of the drawing in the domain are also drawn, for example the x and y locations of the zero coordinate are marked for the positioning, and the location of the y-coordinates of 1000mm and -1000mm are marked for scaling purposes.

In the next image (right hand side of Figure 5.6) the drawing is copied, scaled (conserving the width to height ratio), and located at the zero coordinates again.

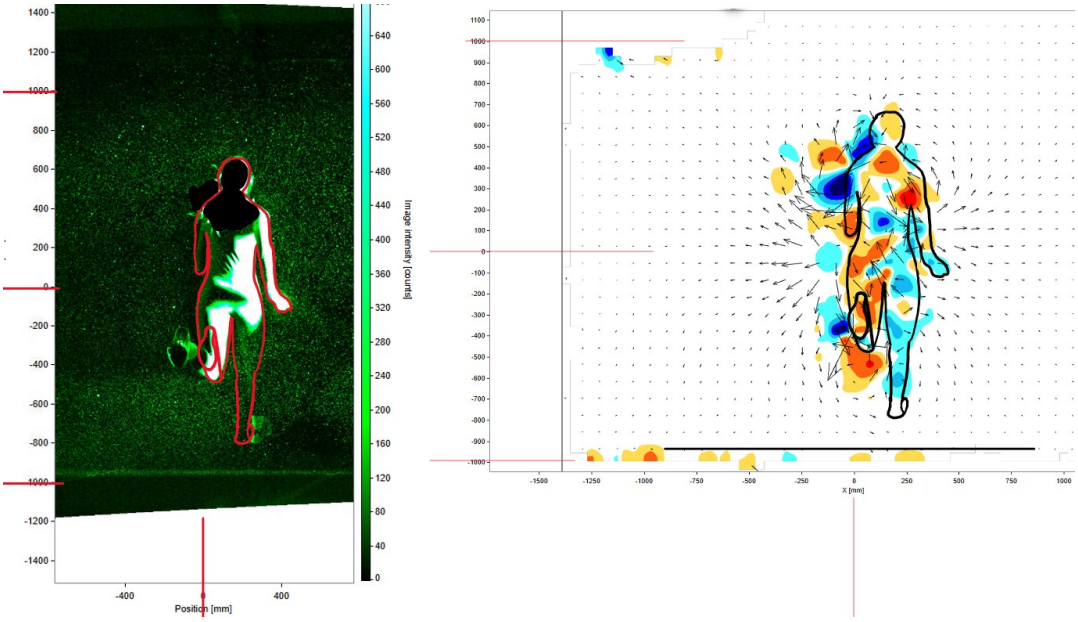

Figure 5.6: Example process of figure outlining and matching with vorticity field

5.3.3. Change of coordinate system

For clarity in chapter 6, the zero coordinate in the vertical direction y has been set at floor level. The lateral coordinate x has been kept the same, with zero in the middle of the running track.

5.4. Averaged flow

For some visualisations, the wake behind the runner is averaged from multiple runs. If this is the case, the following procedure applies:

- Choose a reference lateral coordinate, for example $x = 0$.
- Note the runner's lateral position (measured at the top of the head) during passage with respect to the chosen coordinate.
- export the particle tracks as a set of 3-dimensional velocities at the locations of the particles, where the velocities of the particles depend on the frame number. Convert the frame number to time by dividing by the acquisition frequency.
- Convert the time dimension to the space dimension using running speed for each run: $z = t \cdot V_{\text{athlete}}$. This accounts for slightly differing running speeds between the runs.
- nondimensionalise the velocities of the particle tracks with the running velocity: $\vec{V}_{nd} = \vec{V}/V_{\text{athlete}}$, where $\vec{V}_{nd}$ is the nondimensionalised particle velocity, $\vec{V}$ is the actual particle velocity and V_{athlete} is the athlete velocity during the specific run.
- In matlab, append to one list all the nondimensionalised particle tracks from each run shifted by the runner's lateral position.
- Manually perform binning in the appended file.

The result is a binned set of velocity fields made from all of the velocity tracks of all the considered runs combined.

Assuming similar particle concentrations between the runs, the outcome is the average of the velocity fields. If the particle concentration differs between the runs, the outcome is a weighted average of the runs, local particle density being the weight of the run in averaging.

5.5. Drag analysis

To obtain the drag of a runner, Equation 3.1 for conservation of flow momentum must be applied on a volume around the runner. The control volume is assumed to be moving together with the runner and the only surfaces through which flow passes are 2 vertical planes: one in front and one behind the runner.

To do this, a freestream velocity field (shortly before the passage of the athlete) and multiple wake velocity fields are exported to matlab as planes of binned data. The boundary behind the runner is made by drawing a contour around the wake defined by a threshold flow velocity value. The size of the boundary in front of the runner is selected such that the mass flow is conserved. This procedure has been developed by M. Hirsch and is explained in more detail in the article of Spoelstra et al. [30]

This procedure is repeated for multiple planes in the wake for each run to obtain an evolution of drag with the distance behind the runner. The drag area is computed by dividing the drag values by $\frac{1}{2}\rho u_r^2$, where u_r is the runner's velocity. The concept of drag area is explained in section 2.1.

5.6. Uncertainty analysis

To confirm the reliability of the results presented in chapter 6, the uncertainty of the measured velocity needs to be quantified.

Figure 5.7 shows the uncertainty color map of run A at the reference passage frame. The standard uncertainty of the averaged velocity $U_{\bar{v}}$ is calculated from the standard deviation σ of all velocity vectors within the bin and the number of contributing particles N, as in Equation 5.1, from [29].

$$U_{\bar{v}} = \frac{\sigma}{\sqrt{N}} \tag{5.1}$$

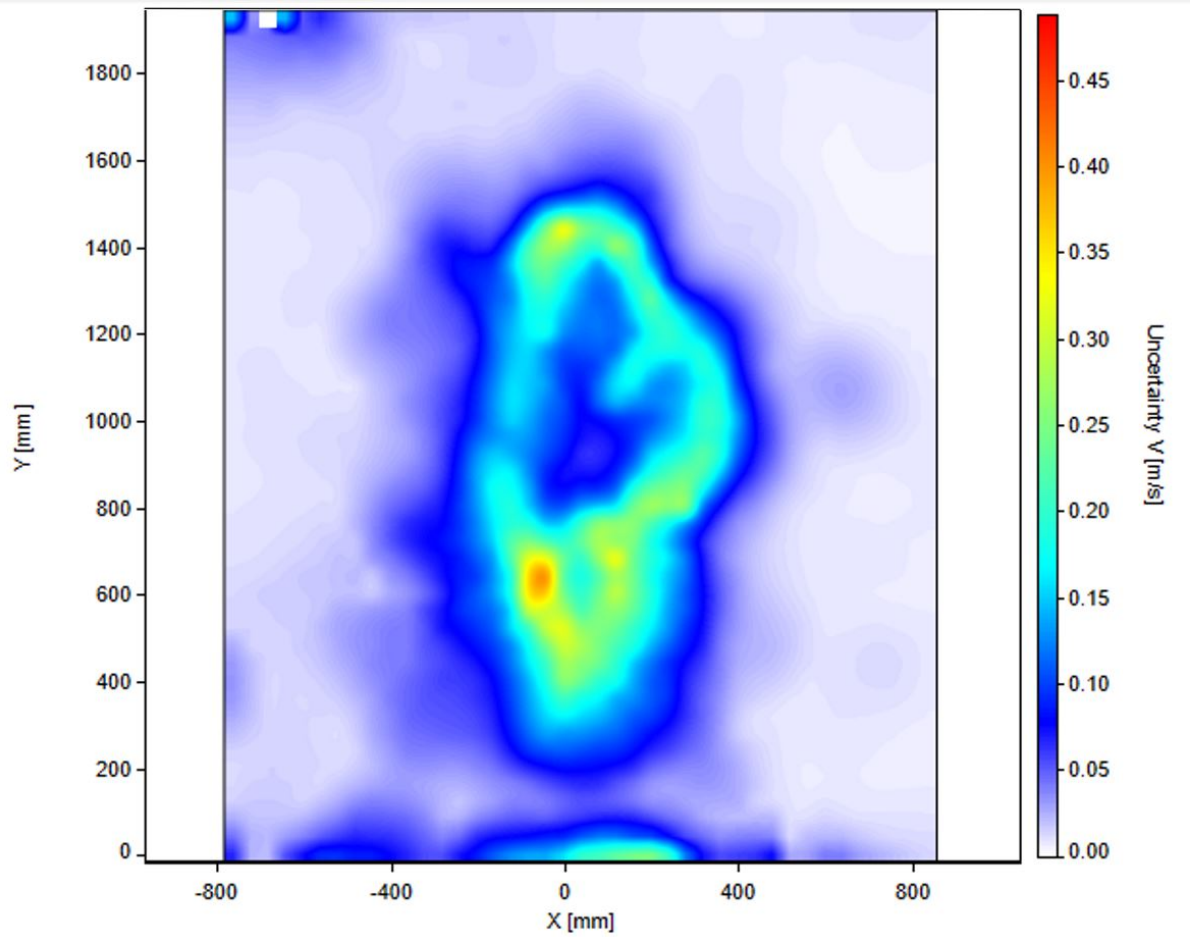

Figure 5.7: Standard uncertainty field of run A in the reference passage frame, at $z = 20mm$

In the reference passage frame, the uncertainty is high in the middle of the domain, where the athlete has just passed. The maximum uncertainty after this frame decreases.

In Figure 5.7, the maximum uncertainty is $0.4m/s$, which is 5% of the athlete's speed. In the freestream around the runner, the uncertainty varies between $0.005m/s$ and $0.025m/s$, which is less than 0.5% of running speed.

The maximum uncertainty appears at the location where the left foot is still in the illuminated plane, possibly causing reflections. The particles can still be correctly identified there, but with higher uncertainty.

Figure 5.8 Shows the variation of maximum uncertainty in the wake of the runner during the reference passage frame. The uncertainty at the edges of the depth of the measurement domain is significantly higher than in the middle, possibly due to weaker illumination. The plane at the z position of $-20mm$ was found to have the smallest maximum uncertainty so it has been chosen for all the single-run processing in chapter 6.

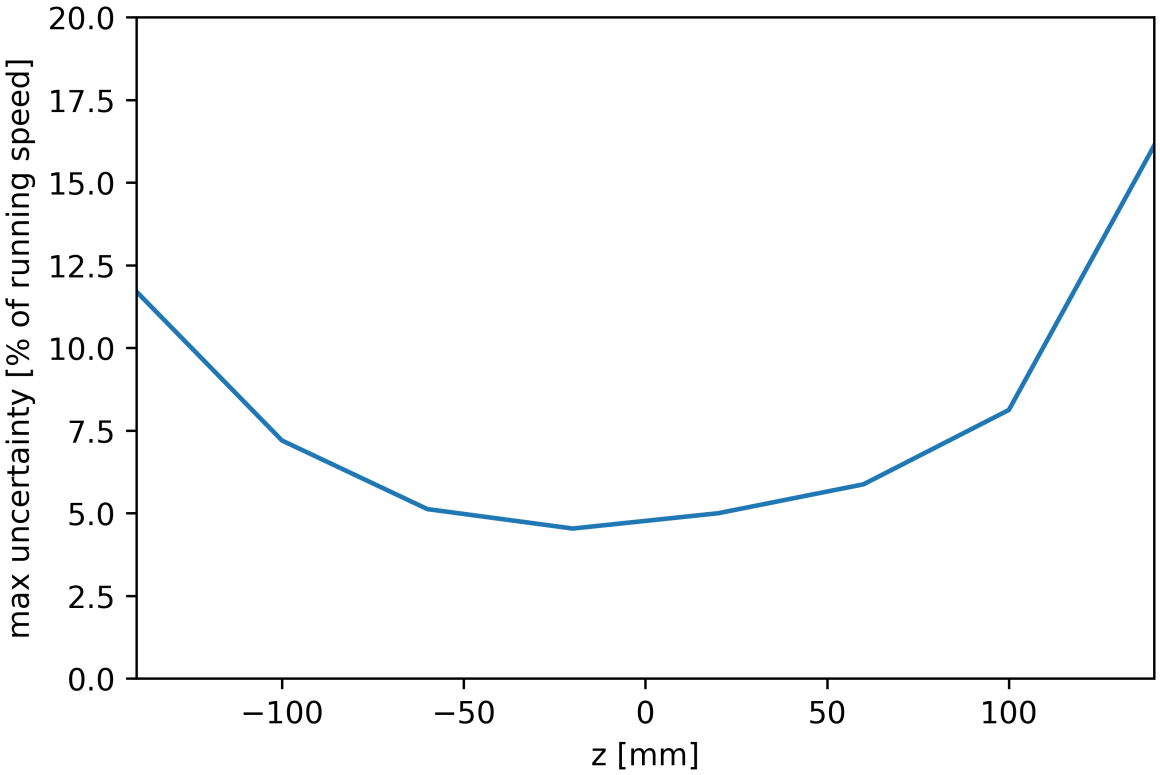

Figure 5.8: Maximum uncertainty variation with the z plane

6 Results

This chapter shows the results of the flow analysis performed using the procedures explained in chapter 5.

Section 6.1 shows general behaviour of the entire wake, visualising the longitudinal velocity with a a 3D contour surface, as well as showing it from a side view and a top view. After that, section 6.2 shows the evolution of longitudinal velocity of the averaged flow in perpendicular planes and then performs a quantification of the velocity deficit in the wake. Later, section 6.3 analyses the vorticity of individual runs in the near wake and then shows an evolution of the vorticity of the averaged flow. Section 6.4 confirms a dependence of wake behaviour on the phase of the passing runner, with a focus on lateral velocity evolution. Finally, section 6.5 estimates the drag of the runner.

6.1. Full wake

This section shows the entire wake behind the runners, to give an idea about its general shape. The constructed images are based on an average flow, as explained in section 5.4. The average in this case is done on runs A, B, C, D and one more run of the same athlete with the same garment in a similar phase of the run.

6.1.1. Full wake visualisations

Figure 6.1 Shows the 3D contour of the longitudinal velocity behind the runner equal to 15% (orange) and 50% (green)) of the running speed, as well as planar cross sections of longitudinal velocity.

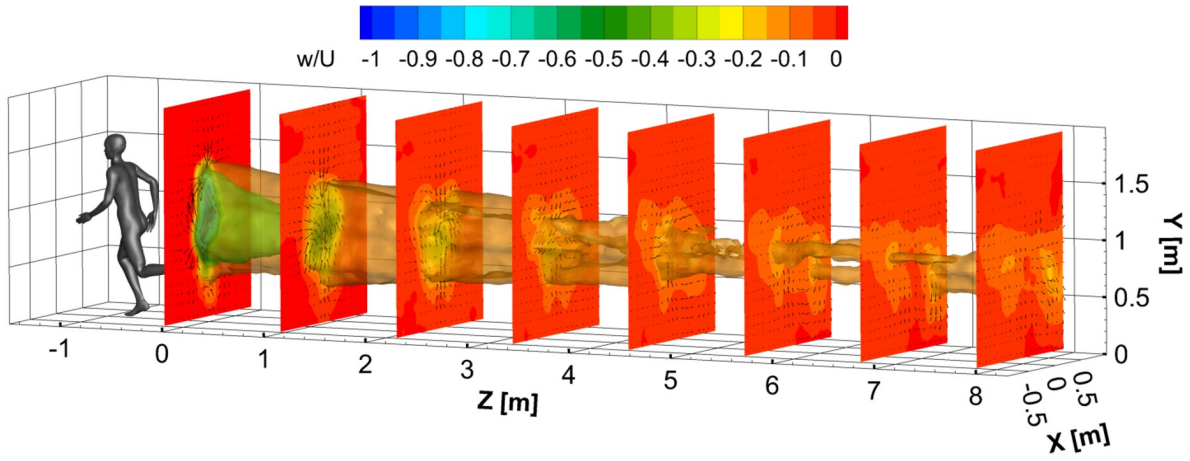

Figure 6.1: 3D contour plot of longitudinal velocity behind the runner, contour is 15% of running speed

In the near wake, it can be seen that the wake has a shape similar to the runner's body. The torso position corresponds to the biggest area of the wake. The left leg also has a contribution to the wake shape, because it is starting to move forward. The right leg is landing on the ground, therefore it is close to stationary with respect to the ground and air, which explains why there is no right leg wake.

As the distance from the runner increases, the 50% wake quickly disappears, and the 15% wake becomes less tall and more wide. Eventually, the longitudinal velocity field splits into 2 areas of peak velocity, with clearly lower velocity between them. This happens at around the height of the arms and it remains in this form until the wake decays.

A possible explanation for the wake splitting into two parts is that there is a remaining velocity where the hand passes through the air at a faster speed than the body itself. This higher initial velocity could remain in the flow for longer than the rest of the wake. However, determining a cause for this phenomenon confidently would require further investigation.

6.1.2. Side view and top view cross-sections

Figure 6.2 and Figure 6.3 show the side and top view cross sections of the average flow field of the 4 runs.

The side view was sliced in the middle, at x = 0mm. Note that as explained in section 5.4, all the runs were horizontally shifted so that they pass exactly through x=0.

The top view was sliced at the location of the hips, at y=830mm, because that is the height where the far wake develops. At this height, the graph provides the maximum information about the far wake flow. Note again how the wake splits into 2 side-by-side stream tubes at around 4 meters behind the runner.

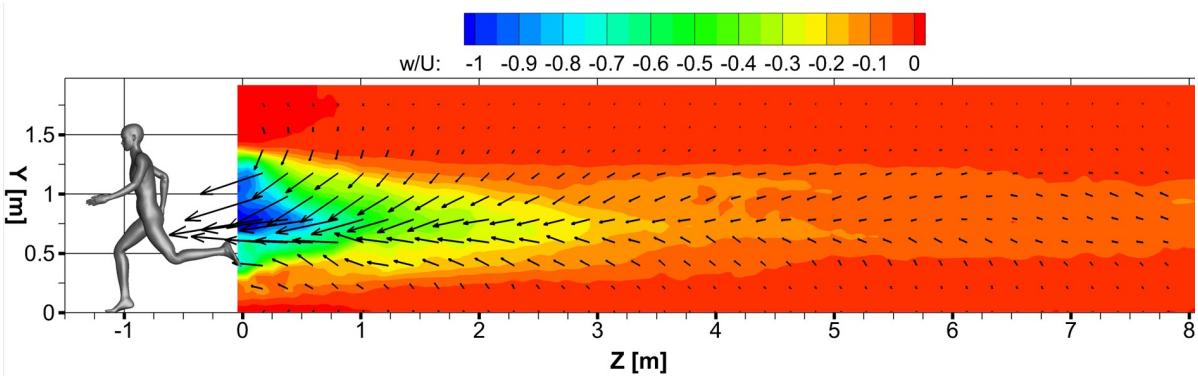

Figure 6.2: Side view of the runner's wake, slice at x=0mm (middle)

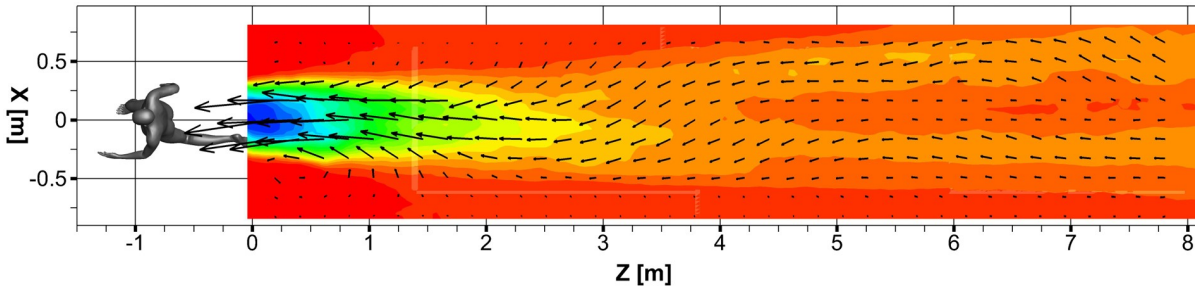

Figure 6.3: Top view of the runner's wake, slice at y=830mm (hip area)

Figure 6.2 shows how the center of the wake emerges from the hips, and the rest of the wake is sucked in towards that point. The wake of the shoulders also contains significant velocity, but there is downwash that pushes that part of the wake down to the hip height. Similarly, the wake of the legs is slightly pulled up to that same central location.

Figure 6.3 shows a straight stream until around 3m behind the runner, where it starts to curve to one side. Around 4m behind the runner the wake splits in two, after which the wake is mostly straight again. Around 7m behind the runner, the flow starts curving to the other side within one of the two wake streams, while it stays straight in the other stream. This asymmetry could be due to the phase of the running motion.

6.2. Longitudinal velocity analysis

This section analyses the longitudinal velocity behind the runner, which can also be called the velocity deficit in the wake. This analysis is important because the integral of the velocity deficit over the entire wake is a direct contribution to the drag calculated by Equation 3.1.

6.2.1. Cross sections of longitudinal velocity

Figure 6.4 shows the positions of planes for which the velocity fields, averaged across runs A, B, C and D, are shown in Figure 6.5 and Figure 6.6. This set of velocity fields shows the evolution of longitudinal velocity fields in the runner's wake.

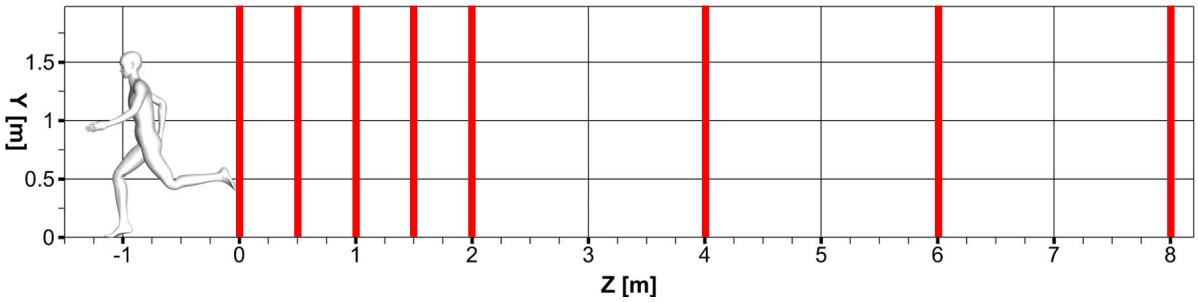

Figure 6.4: Plane locations

The area of nonzero longitudinal velocity field can be referred to as the wake. Figure 6.5 shows that right behind the runner, the wake originates mostly from the torso, with some contribution from the head, hands, and a smaller contribution from the legs.

Already 0.5m behind the runner the wake starts to shrink vertically and stretch horizontally. The magnitude of the velocity in the center of the wake decays as the size of the wake increases slightly in the range of 0.5m to 2m. Until 2m behind the runner, there is a clear downwash in the middle of the wake

Figure 6.6 shows that after 4m, the averaged wake splits into 2 seperate wakes, where there are 2 maxima of longitudinal velocity on the sides, in the middle between them the velocity is back to the freestream. It could be thought that this is just an effect of averaging, that some of the runs had the wake travel to the left, and some had it travel to the right. However, this behaviour is also noticeable in the non-averaged velocity fields of runs B and C. Figure 6.7 shows an example of this phenomenon from the single flow field of run C at a distance of 9m behind the runner. The cause for this phenomenon has been discussed in subsection 6.1.1.

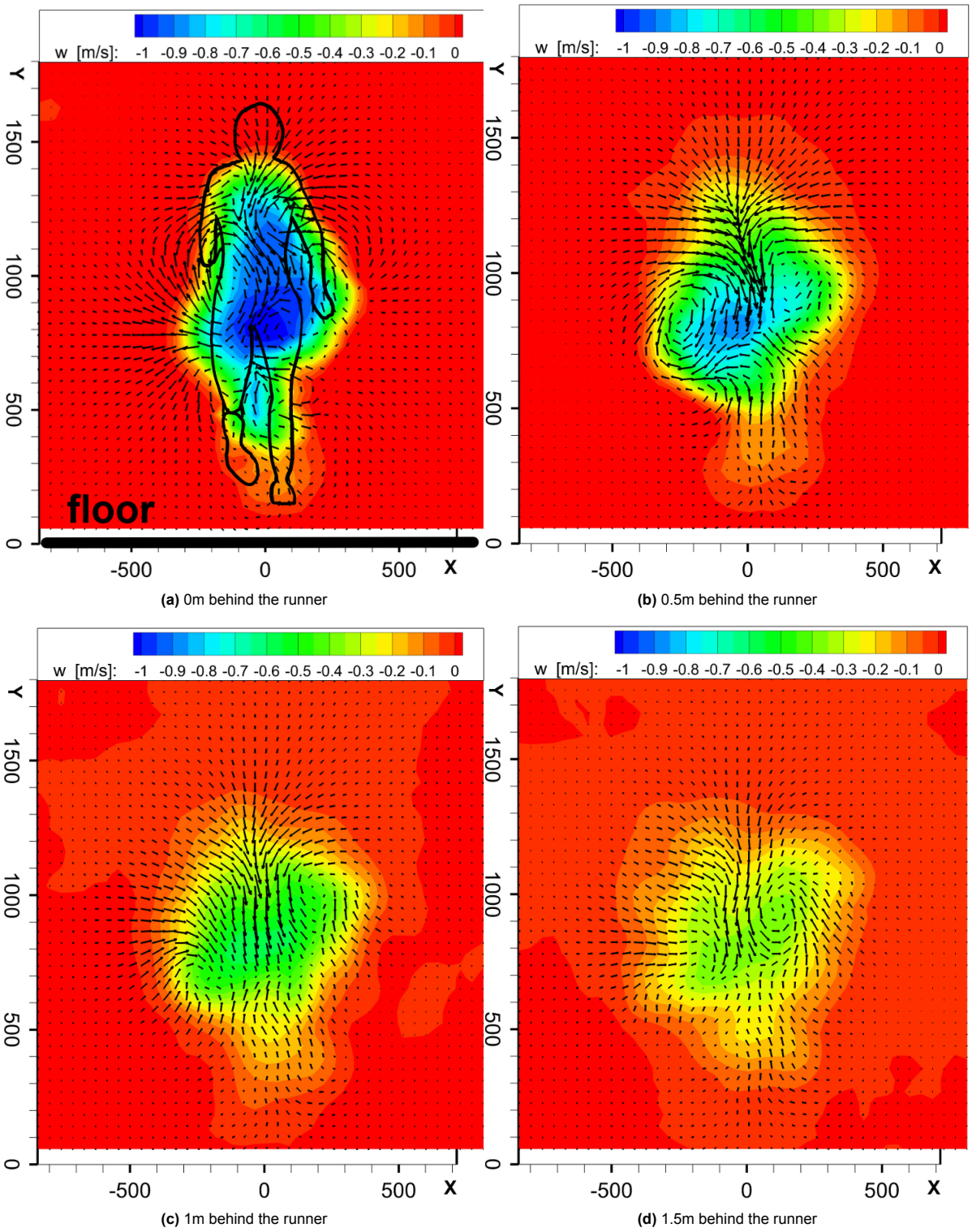

(a) 0m behind the runner

(b) 0.5m behind the runner

(c) 1m behind the runner

(d) 1.5m behind the runner

Figure 6.5: Longitudinal velocity fields at 0m to 1.5m behind the runner, averaged from runs A, B, C and D

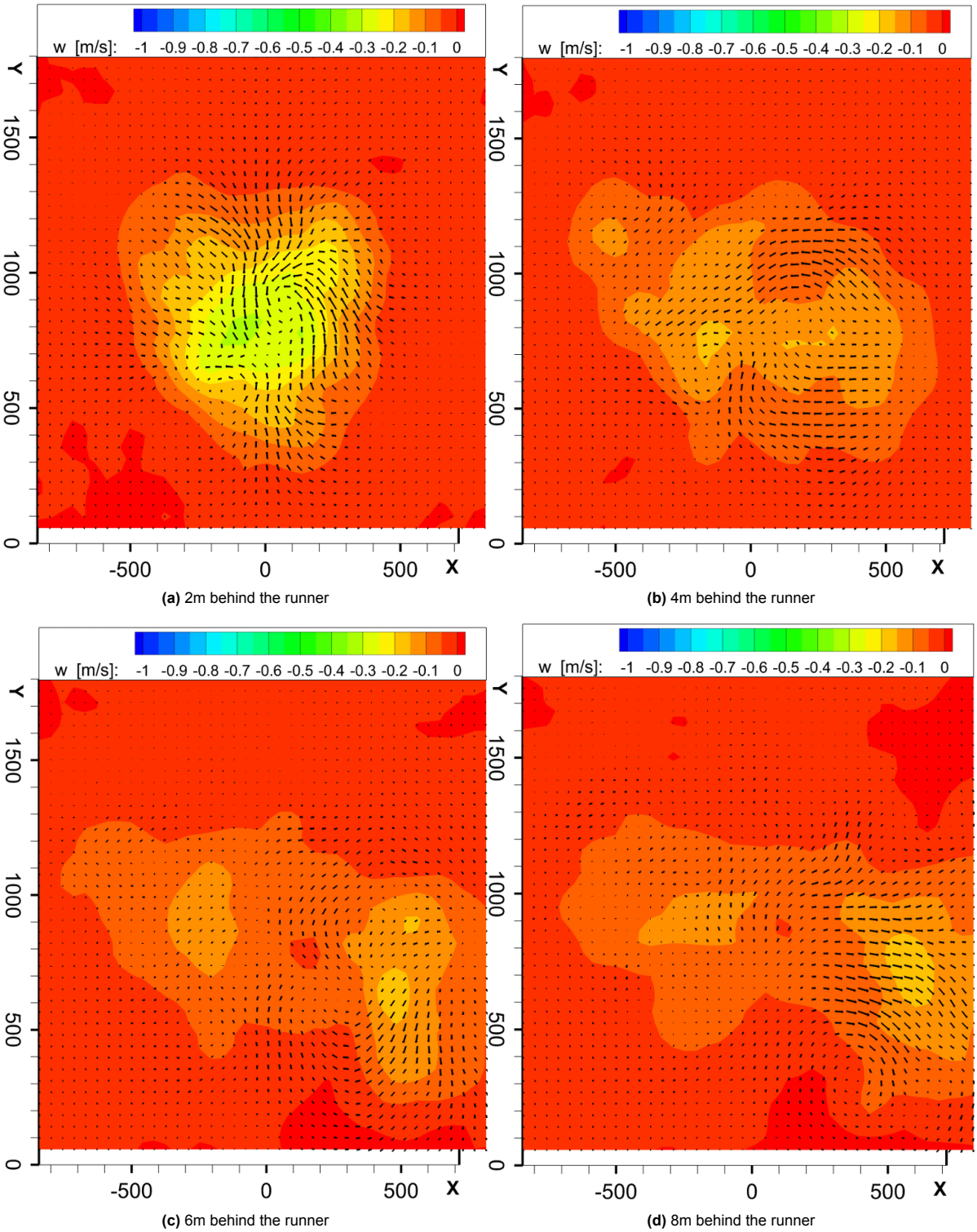

(a) 2m behind the runner

(b) 4m behind the runner

(c) 6m behind the runner

(d) 8m behind the runner

Figure 6.6: Longitudinal velocity fields at 2m to 8m behind the runner, averaged from runs A, B, C and D

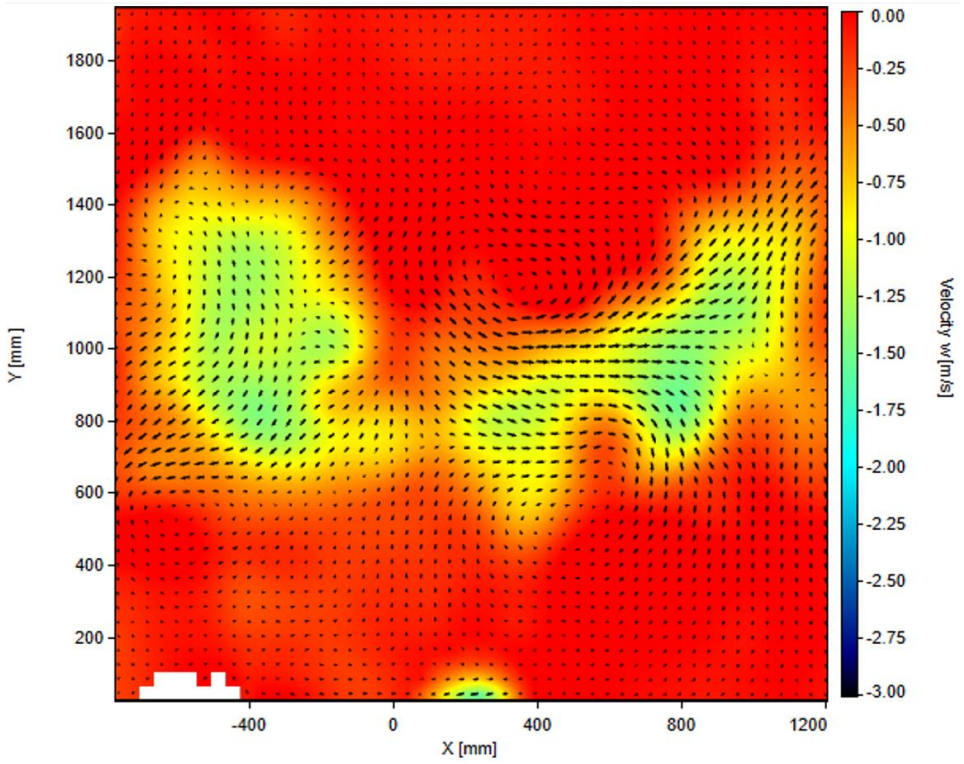

Figure 6.7: Longitudinal velocity field of run C, 9m behind the runner

6.2.2. Velocity deficit quantification

The velocity deficit in the wake of the runner can be quantified by inspecting the evolution of the longitudinal velocity of the wake.

One parameter to investigate is the average velocity in the running direction over an area behind the runner's body, equivalent to the runner's torso. This can be useful for determining how close to the front runner a drafting runner would have to be to gain any aerodynamic benefits. The torso area has been chosen as the most important in agreement with the conclusions of section 6.1.

Another parameter that is interesting to investigate is the maximum value of the longitudinal velocity and its evolution.

Both of those values were investigated for all available data after passage of the athlete in run A. Figure 6.8 shows the placement and size of a rectangle in which the velocity is averaged, with respect to the runner's torso. on the right side of Figure 6.8 it can be seen that right after passage, the rectangle overlaps with a large portion of the highest velocity wake.

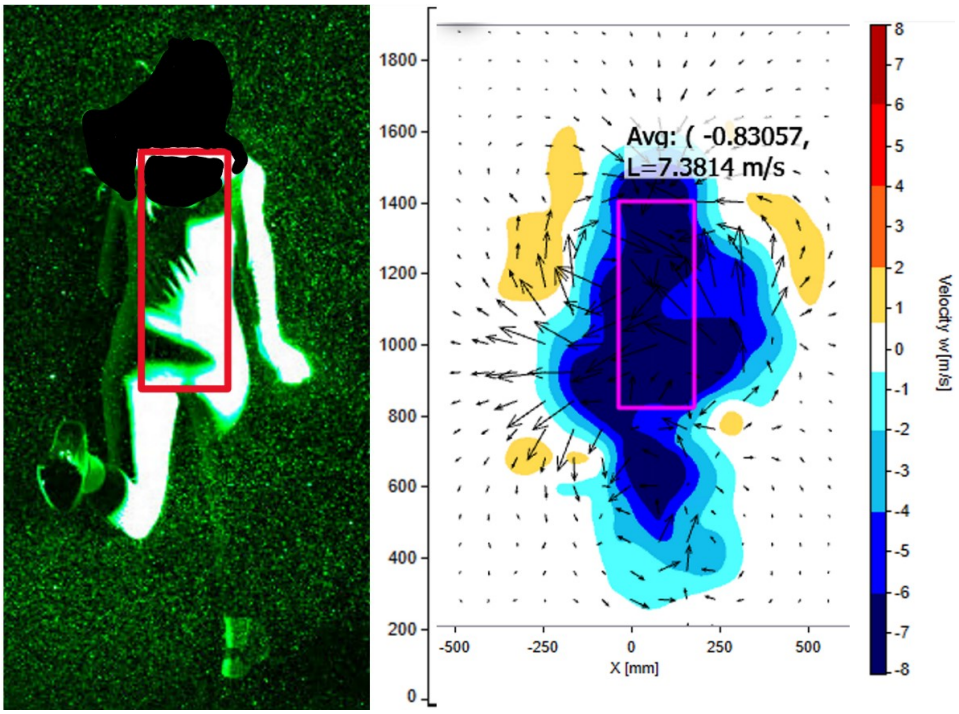

Figure 6.8: Area used for averaging the velocity behind the runner's back.

Figure 6.9 shows the maximum and averaged longitudinal velocity as a function of distance behind the runner. The graphs initially follow a trend of exponential decay. The maximum velocity just behind the runner is slightly higher than the runner's speed, where the recirculation zone contains particles travelling at 120% of the runner's velocity. The average velocity just behind the torso is slightly lower than the running speed because the flow in the recirculation region gets averaged with some flow from outside of the recirculation region.

At some point between 4 and 8 meters behind the runner, the graphs reach a plateau, and then their values grow slightly, the maximum velocity growing more than the average. This happens because a higher velocity region develops on the sides of the wake, as was seen in Figure 6.6. The maximum velocity graph of course detects that, but the region of higher velocity falls outside of the torso rectangle where the average is taken, which means a trailing runner wouldn't feel this effect fully. Note that the maximum velocity increases in the far wake instead of the expected decay. This maximum velocity is found in one of the two separated stream tubes, which fall outside of the blue line's averaging rectangle, so it's possible that a trailing runner in the far wake might get a higher aerodynamic benefit at a slight sideways offset, not in the center of the wake.

Pope [31] claims the velocity in the far wake of a bluff body decays with $x^{-2/3}$. For cyclists in the near wake the decay is claimed to be proportional to $x^{-1/3}$ [13].

In Figure 6.9, the averaged wake longitudinal velocity in the torso area is roughly proportional to x^{-1} between 2 and 8 meters behind the runner. This is the expected trailing distance in running sports, because at a trailing distance of less than 2 meters, a collision with the leading runner is expected.

The conclusion for a trailing runner is to keep as close as possible to the leading runner, because the drag benefit of being in the wake diminishes quickly with increasing trailing distance. At a distance exceeding 2 m, the drag benefit is expected to become negligible, especially considering that the pressure term decays faster than the momentum term, which is proven by Figure 3.5.

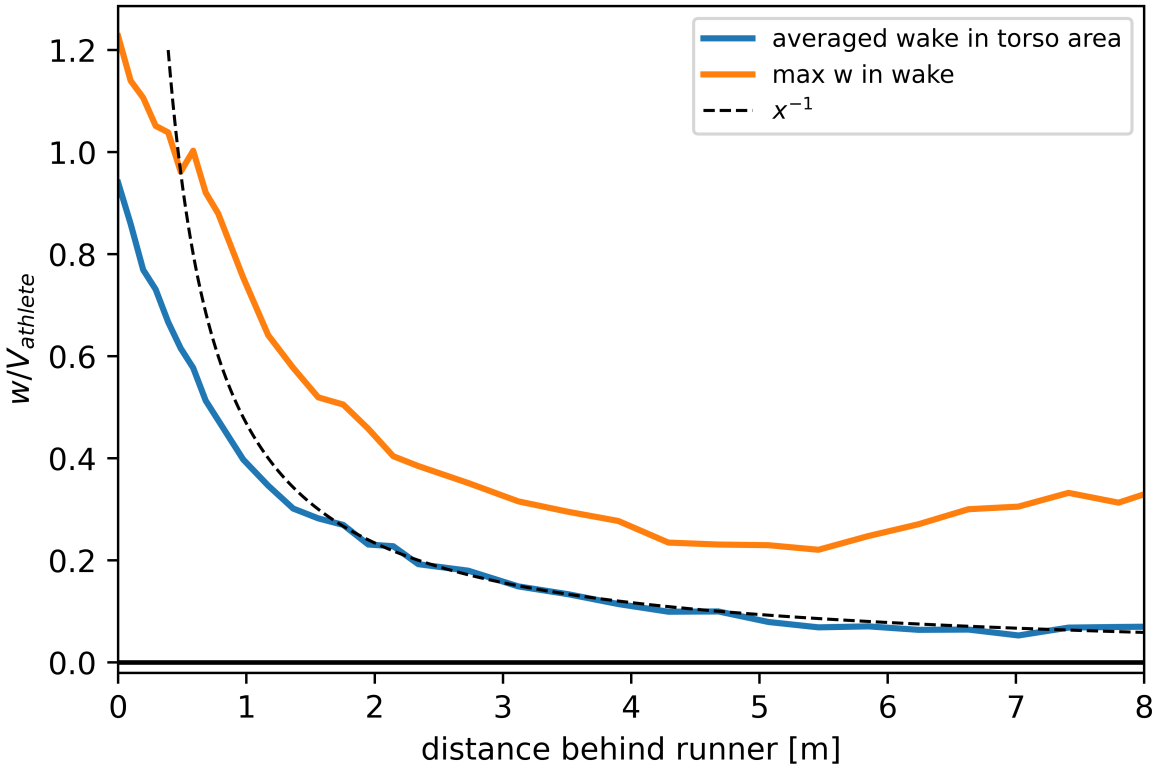

Figure 6.9: Maximum and averaged longitudinal velocity as a function of distance behind the runner

6.3. Vorticity analysis

This section aims at developing new understanding of vorticity structures in the wake of a runner. The creation of vorticity is important to understand because it can be the base for understanding the origin of any vortices formed behind the runner. Vorticity fields can also show areas where more energy is inserted into the flow and therefore lost by the runner. By this reasoning, it should be possible to reduce the drag of a runner by addressing the flow in areas of high vorticity.

To do this, vorticity pairs are identified in the close wake of three runs of the same athlete, and their positions are investigated with respect to the athlete's body parts. The z-direction vorticity is considered because the main vortex structures have their axes mostly in the z-direction.

It's important to note that the vorticity identified in this section does not only represent vortices, but also areas of shear flow. This section uses the λ_2 criterion to locate vortices, which is further explained in Appendix B.

A discrete color scheme has been chosen for easier understanding of the exact locations and strengths of the vortices. For clarity, the zero-vorticity color is white, and the strength of vorticity is displayed as the saturation of the blue and red colors. The color scale is symmetric and in all runs is limited to the same value of ± 100 [1/s].

The perpendicular sketch of the athlete for each run has been created separately using the method explained in subsection 5.3.2. The images for each run are the vorticity fields with dense arrows of in-plane velocity components, overlaid with the sketch of the athlete in black and vorticity identification markers in grey.

Run A has an identifiable vorticity field already around 10 frames ($0.025s$) before the reference frame, and it becomes more chaotic already at the reference frame, which is a good opportunity to investigate the very near wake. The other two runs have a chaotic very close wake, but the vorticity structures become identifiable at the reference passage frame, so they are used to investigate the regular close wake.

Lastly, note that in runs A and C the athlete passes through the measurement domain in exactly the same phase (midway through the flight with right foot forward, with the right hand swinging forward and the left hand swinging backwards) and in run B the phase of the run is slightly earlier, meaning that the athlete is passing through the measurement volume sooner after launching from the left foot, and both of her arms are stationary, not swinging yet. This phase difference will be visible in the wake. The phases during the reference passage frame have been shown in Figure 5.4.

Lastly, the vorticity patterns for run D were not identifiable like in the rest of the runs, the close wake was more chaotic. It might be due to the loose long hair. Enough information about the vorticity fields has been extracted from runs A, B and C, so it has been decided that run D wouldn't add anything valuable in this section.

6.3.1. run A

Figure 6.10 shows the vorticity right after passage of run A. The phase of the athlete is just before landing on the right foot. Note that the floor height is drawn on the left of the figure.

Note that the frame analysed here is around 8 frames ($0.02s$) earlier than the other two runs. The outward flow around the torso is strongly visible, which means the wake is still expanding. There is no downwash visible yet, but it appears in later frames, similarly to the runs shown further below.

The main body's vorticity is identified at the head, shoulders and hips, where it follows the logic of the flow around a finite cylinder, as explained in chapter 2. The vorticity at the head and shoulders is the strongest, and it is in the direction that creates a downwash, because the body has a sudden reduction in width on the upper side. Inversely, the vorticity at the hips is such that it creates an upwash, because the body has a sudden reduction in width on the bottom, where the torso ends and legs begin.

Note that the right hand, even though it is swinging forwards as a finite cylinder, doesn't show any vorticity in this frame. The hand is behind the runner, and it still has not passed through the measurement volume, therefore its effect is not seen yet. In later frames of this run the right hand vorticity appears and behaves similarly to the right hand vorticity identified in the other two runs.

Another vorticity pair identified in this run is the right foot vorticity pair, where there is cylinder tip behaviour again. The vorticity creates an upwash in the location where the foot passed, as the foot the tip of the moving cylinder (which is the leg).

An interesting vorticity pair identified in this run is the left knee vorticity pair, which rotates the opposite direction to what is expected from a steady-body analysis. The bent knee acts as a tip of the thigh cylinder, but it creates the opposite rotation of what a cylinder tip would create. It is observed that this might be caused by the knee moving downwards in addition to forwards in this phase of the run, which overcomes the cylinder tip effect and creates quite a strong local downwash. The strength of this effect can be clearly seen by the saturated color of this vorticity pair in Figure 6.10.

Using the λ_2 criterion, the main vortex behind the runner in this run is contained in the left shoulder vorticity, as can be seen in Figure B.1. This matches the high strength of the left shoulder vorticity and the clockwise curving nature of the vectors seen around that vorticity area.

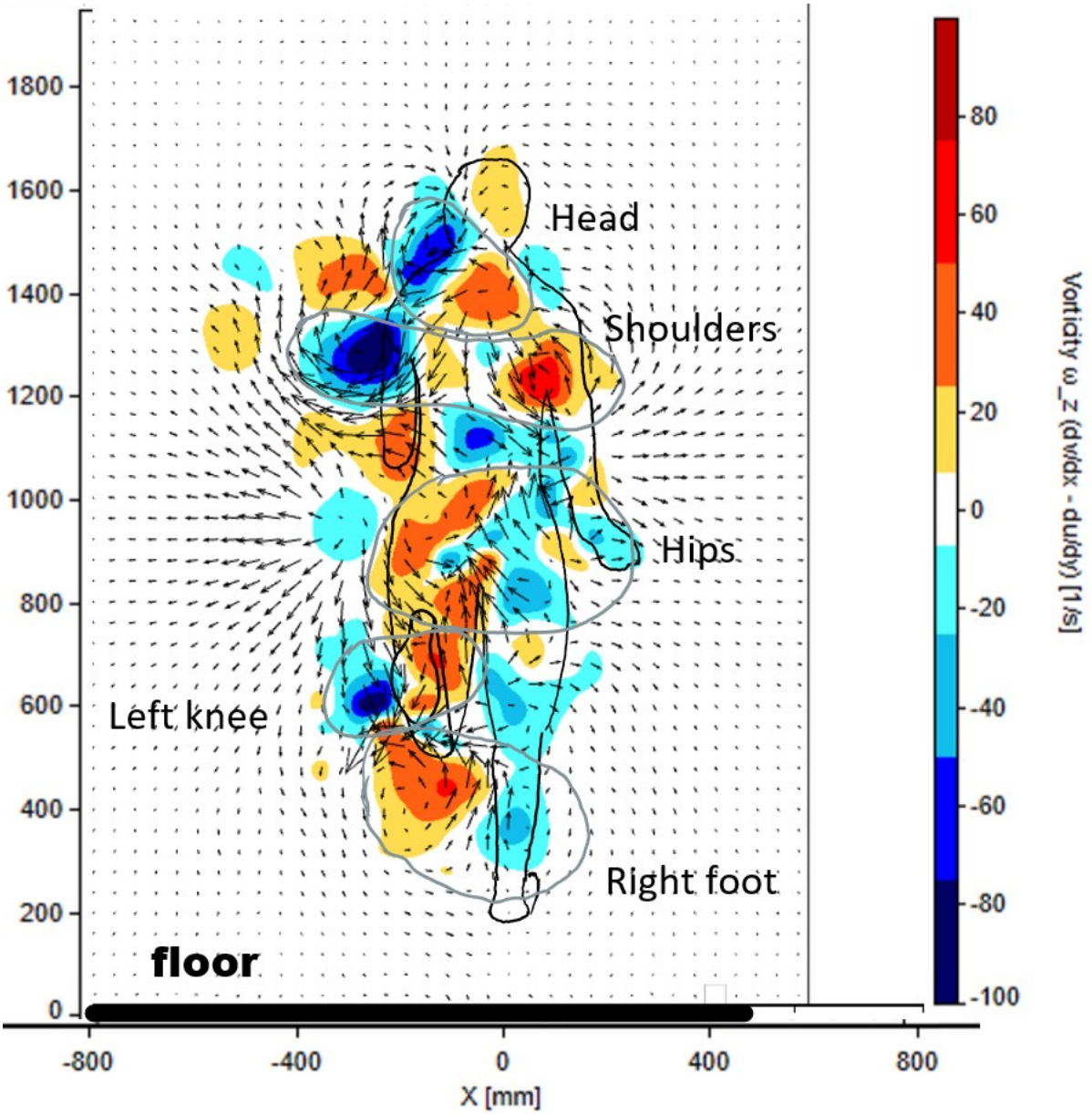

Figure 6.10: Vorticity origin identification on run A right after passage

6.3.2. run B

Figure 6.10 shows the vorticity right after passage of run B. The phase of the athlete is again during flight, before landing on the right foot. However, note that the phase is slightly earlier than in the other two runs, which has an effect on the identified vortices.

During the frame analysed here, the outward flow around the torso seen in the previous run is not visible anymore, but the characteristic downwash behind the athlete's back is fully developed. This might mean that the available data begins slightly further in the wake than in the previous case. However, the difference is small and the identified vortices are all still not displaced from their original locations.

During this run, the dominant vorticity pair is again the shoulder vorticity pair, having the largest strength visible in the image.

The hip vorticity identified in run A is not visible here, it instead got dominated by the vorticity caused by the hands, which is equivalent to the tip of the arm cylinder, pointed downwards. Therefore, during this run both hands cause a vorticity pair in the direction that makes an upwash at the location where

each hand passed the measurement domain.

The effect of the left hand vorticity is stronger than in the other two runs due to the slight phase difference. During the passage through the measurement domain, the left hand was still not swinging backwards, instead it was pointed forwards, in front of the athlete's torso, even with a bit of forward momentum from the phase before.

The vorticity below the waist is difficult to distinguish.

Run B has the most structured vortex geometry in the wake, looking at the λ_2 criterion in Figure B.2. Both shoulder vorticity regions form counter-rotating vortices, despite the relatively low strength of the left shoulder vortex. In the area where the left hand passed the measurement domain, there is also one clockwise rotating vortex, in the area of strong negative vorticity. If the hand was a finite wing, this vortex would correspond to the wingtip vortex.

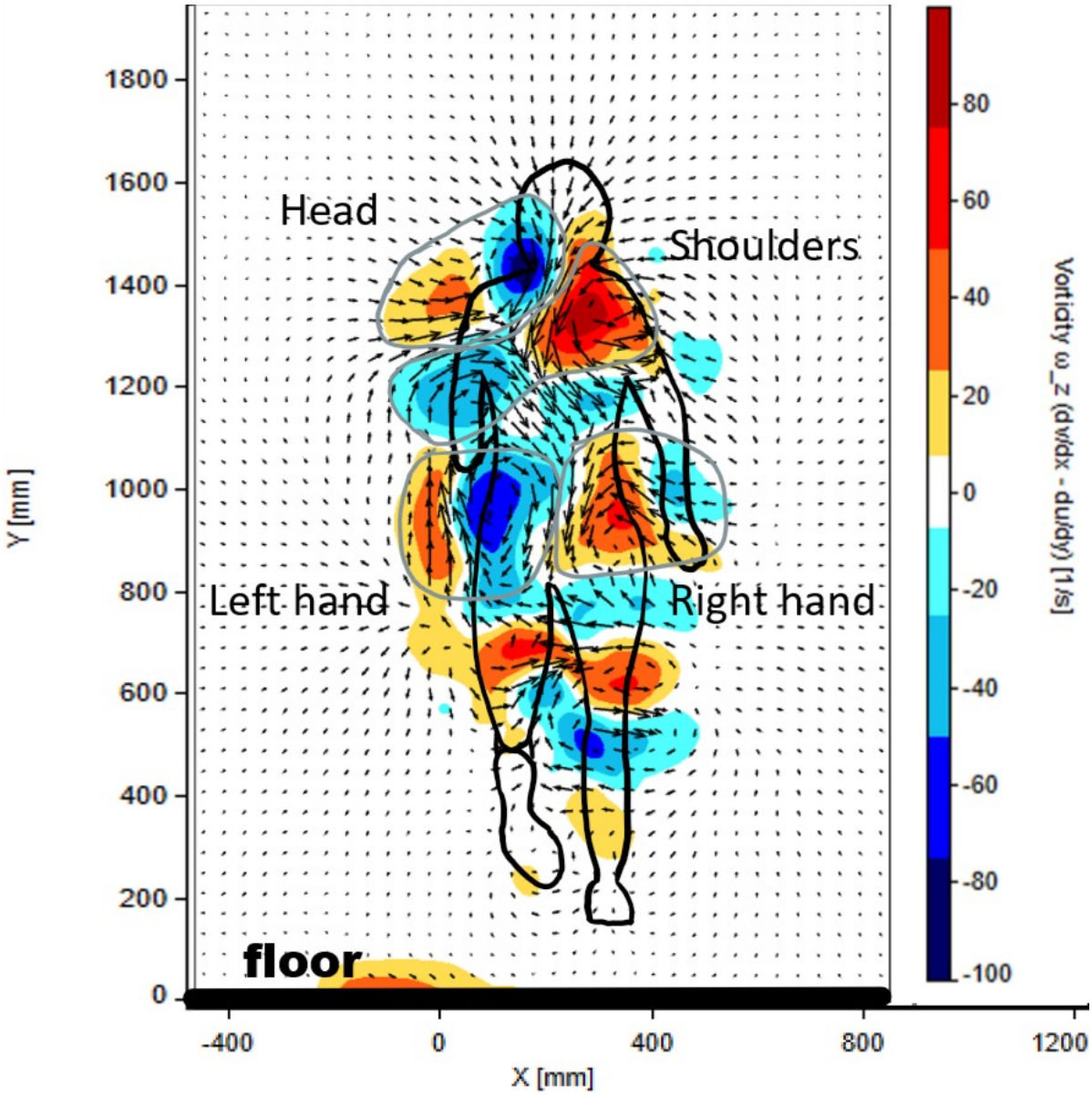

Figure 6.11: Vorticity origin identification on run B right after passage

6.3.3. run C

Figure 6.10 shows the vorticity right after passage of run C in the same phase of the run as before. It shares similarities with both of the previous two shown runs, which suggests that the results are repeatable.

During the frame analysed here, the outward flow around the torso is still visible on the left side, but not on the right, and the characteristic downwash behind the back is well defined.

Similarly to run A, the head and the shoulder vorticity pairs are distinguishable from each other. The shoulder vorticity strength in this case is not significantly larger than the rest, but it is still significant.

The right foot vorticity pair appears in a similar form to run A, and the right hand vorticity pair is similar to the one in run B. The chaos on the unidentified left side of the torso and the lack of a clear left hand vorticity structure can be explained by the left hand swinging backwards.

There is also a left foot vorticity pair in the same location as in run A, but this time in the opposite direction, causing an upwash at the location of the foot. Looking at the relatively high strength of the left foot vorticity pair, it is caused not only by the forward movement of the tip of the leg cylinder, but also by the upwards movement of the foot as it passes through the measurement domain. This suggests that this specific vorticity pair is highly sensitive to the movement of the trailing foot, which varies with the runner's technique.

Despite all the vorticity regions, run C has no clear vortex in the wake. This can be seen in Figure B.3, where the values of λ_2 are significantly less negative than in the other runs. This means that the vorticity field of this run mostly represents shear layers or other strains.

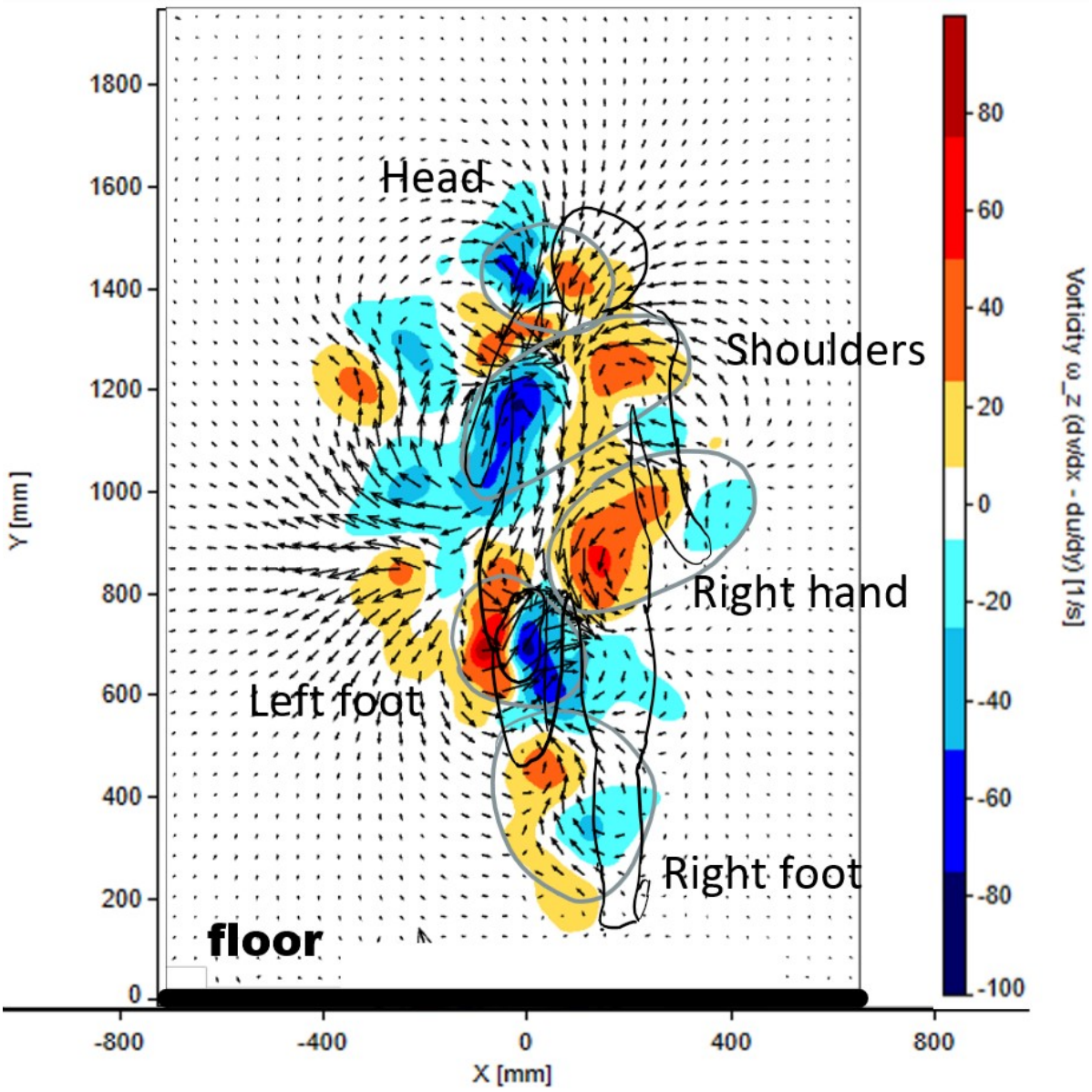

Figure 6.12: Vorticity origin identification on run C right after passage

6.3.4. vorticity conclusions

The conclusion of this investigation is that many of the vorticity structures are repeatable and they can be traced back to the body parts that cause them.

The shoulder vorticity pair seems to be the strongest, the easiest to identify and the most repeatable across different runs. The head vorticity pair works on the same principle as the shoulder vorticity pair, but in some cases the two can get blended together because of their proximity and shared directionality.

The hip vorticity that has been theoretically proposed to exist due to the decrease of the body's width from the torso to the legs (and the bypass flow between legs) has been identified in the very close wake, but it is weaker and less repeatable than the shoulder vorticity. This makes sense because of two reasons: Firstly, the decrease in body width on the upper torso is larger than it is on the lower torso, dictating the larger strenght of the tip vorticity. Secondly, the weak hip vorticity can get interrupted by other vorticity created closeby, like the highly variable hand and leg vorticity. The latter explains why the hip vorticity was only visible in the very close wake of run A, before the right hand passing by interrupted it.

As for hand vorticity, the pattern for the phase of the run analysed here is that the right hand vorticity pair apperas more often than the left pair. This happens bacause during this phase of the run, the right hand tends to be extended and travel forward, slightly away from the body, and the left hand tends to be bent, traveling backwards, closer to the body, therefore its effect is less pronounced. The exeption of run B, where both hand vorticity pairs exist and are strong, is due to a small difference in phase to the other two runs, causing two effects: Firstly, the left hand is stationary and not moving backwards, allowing it to make a cylinder tip vorticity pair. Secondly, the left hand vorticity still remains from when it was created by the left hand moving forward (which is the phase just before the analysed phase).

The vorticity analysis suggests possible areas of improvement that could lead to lowering the runner's drag, like the shoulders and arms, which both cause a significant vorticity. A proper use of flow control devices like vortex generators over the shoulders and arms could decrease the vorticity in the flow and possibly reduce drag.

6.3.5. Evolution of average vorticity in time

Figure 6.14 shows the evolution of the vorticity field behind the runner. The vorticity fields are averaged from runs A, B, C and D with the method explained in section 5.4. The velocity fields are taken at the planes shown in Figure 6.13.

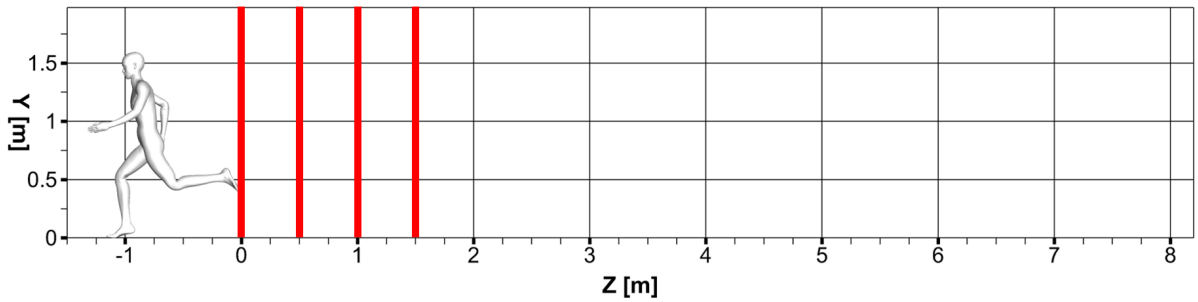

Figure 6.13: Locations of planes for vorticity evolution analysis

It can be seen that the vorticity origins identified in previous sections have some similarities, because the averaged field keeps some identifiable vorticity structures. The averaged vorticity fields show that in general there are two main vorticity areas, a positive one on the right and a negative one on the left. At 0m behind the runner in Figure 6.14 those two main areas correspond to the shoulder vorticity identified in the previous section. Using a λ_2 criterion for vortex identification, it is confirmed that those two main vorticity areas indeed correspond to the presence of two counter-rotating vortices at 0m behind the runner. This is shown in Appendix B.

Looking further into the wake, 0.5m behind the runner the right and left shoulder vorticity areas remain prominent, while other areas of vorticity fade out. The left vorticity area has the characteristics of a clockwise rotating vortex, while the right area does not. There is also a noticeable strong downwash between the two mentioned areas. Interestingly, 1m behind the runner the left, clockwise vortex fades away and 1.5m behind the runner the right shoulder vorticity area becomes a counter-clockwise vortex. This switch of vortex location and rotational direction can be due to the changing phase of the running motion.

The vorticity after 1.5m behind the runner mostly fades away, without any high maximum values. However, some weak vorticity structures remain and they are shown in Figure 6.15.

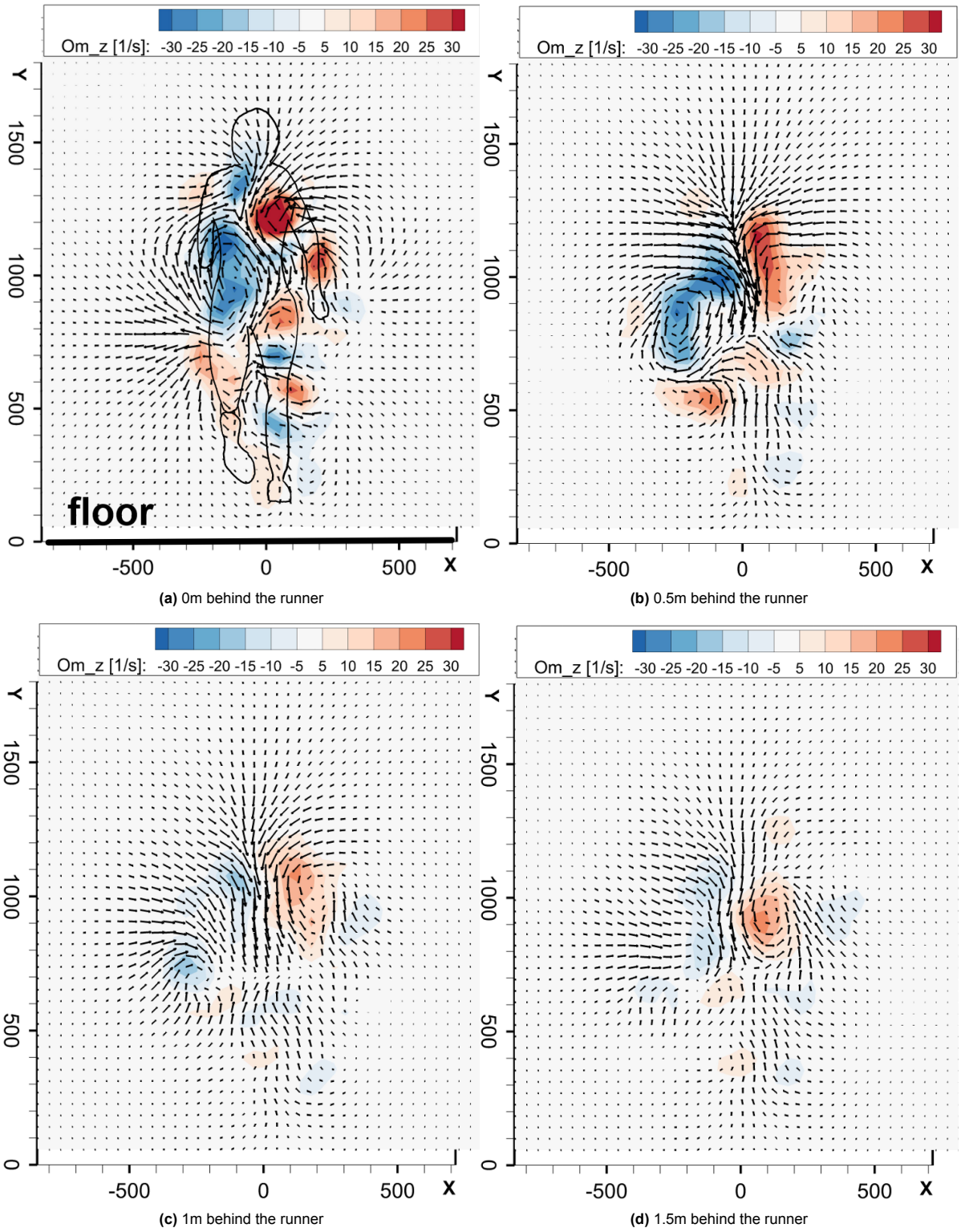

(a) 0m behind the runner

(b) 0.5m behind the runner

(c) 1m behind the runner

(d) 1.5m behind the runner

Figure 6.14: Vorticity evolution for the flow averaged from runs A, B, C and D

Figure 6.15 shows a contour surface with a low vorticity value of $8s^{-1}$. This graph shows that even thouigh the vorticity decays quickly within the first 2m of the wake, long backwards pointing tubes of low-value vorticity remain in the wake. It is interesting to note that around 2 to 4 meters behind the runner the vorticity is mostly positive (red) and later, around 6 to 8 meters behind the runner, the vorticity is mostly negative. This change of the vorticity direction matches almost perfectly with the change in the

direction of lateral velocity in Figure 6.21 later in section 6.4, where it has been associated with the changing phase of the running motion.

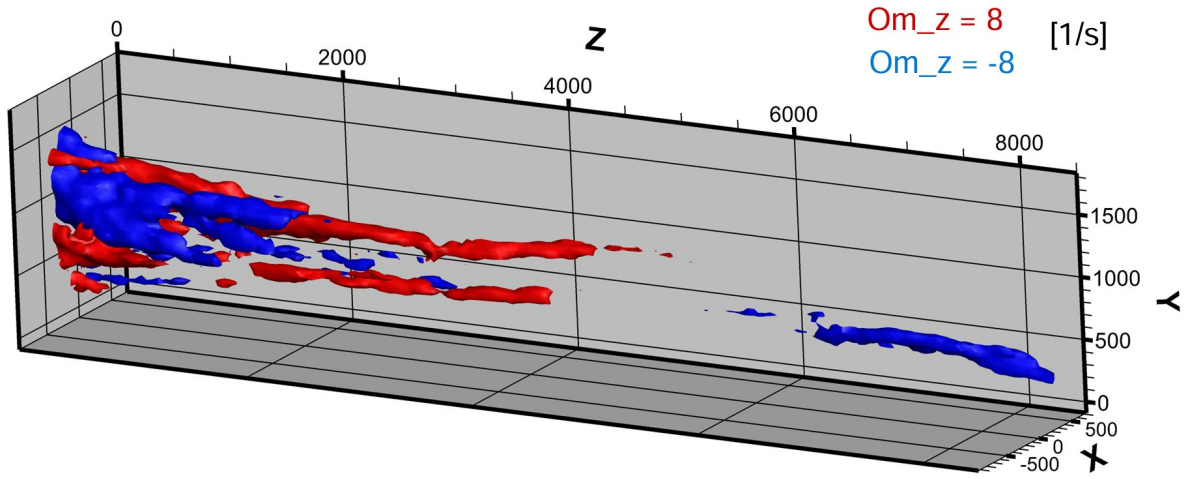

Figure 6.15: Contour plot of z-direction vorticity of the average of runs A, B, C and D, with contours of $\omega_z = \pm 8s^{-1}$

6.4. Dependence of lateral velocity on the phase of the running motion

Since each athlete passed through the domain in a roughly consistent phase every run, the only comparison between different phases happens between different athletes. Therefore, in comparing different phases, the differences seen will be not only due to phase difference, but also due to athlete difference. With the current data it is not feasible to analyse the full effect of phase on the flow beyond visual observations. However, some effects of the phase on the wake can be investigated.

During the experiment, it was visually noted that during some runs the flow suddenly accelerates to one side. An interesting topic to investigate is whether the wake oscillates sideways with the frequency of the runner's steps. Figure 6.17 shows the evolution of the sideways velocity u with distance after passage. The velocity was averaged over a large rectangle containing the entire wake, without the wrong vectors on the edges of the domain, as shown in Figure 6.16. If the wake shifted to the side towards the end of the run, the averaging rectangle was also shifted to still cover the whole wake, but the area was kept constant.

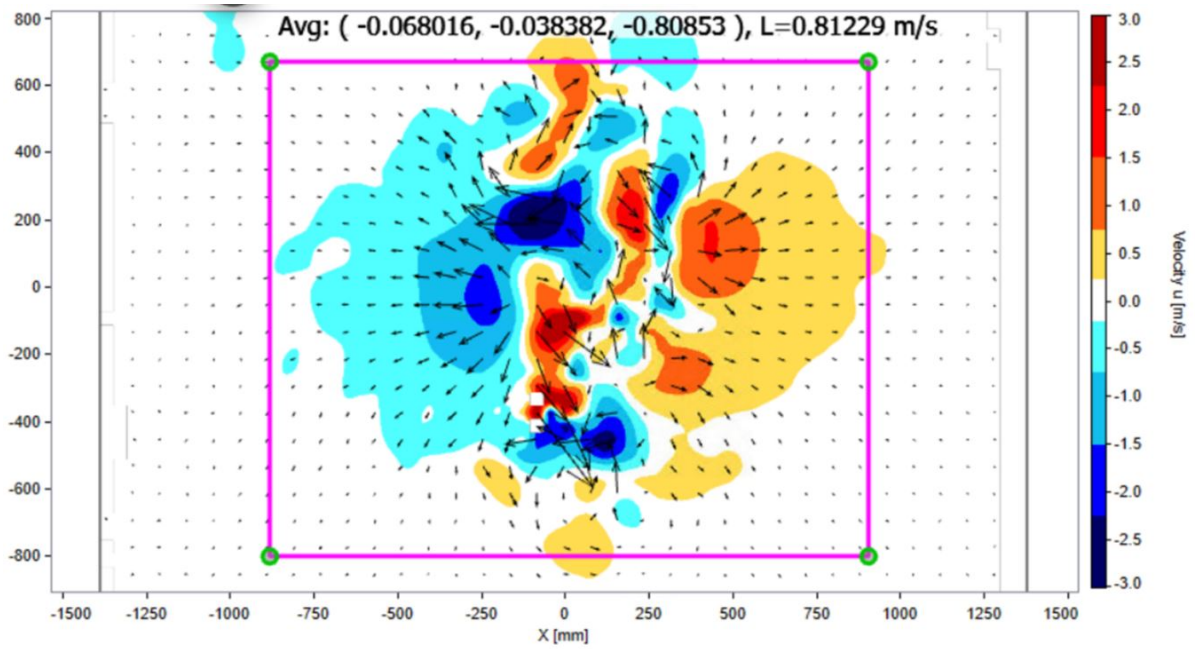

Figure 6.16: The domain in which the lateral velocity is averaged.

The time axis of Figure 6.17 starts at the reference passage time frame. This means the runs are synchronised to each other with respect to the runner's position on the track. However, runs A and C are in a running phase slightly later than runs B and D.

A black sinusoid has been plotted with the same frequency as the runner's movement. Since it takes 220 frames (0.55s) for a runner to go through an entire cycle of 2 steps, the sinusoid has a frequency of $1/0.55[1/s]$ and it is scaled to match the initial amplitude of the other curves.

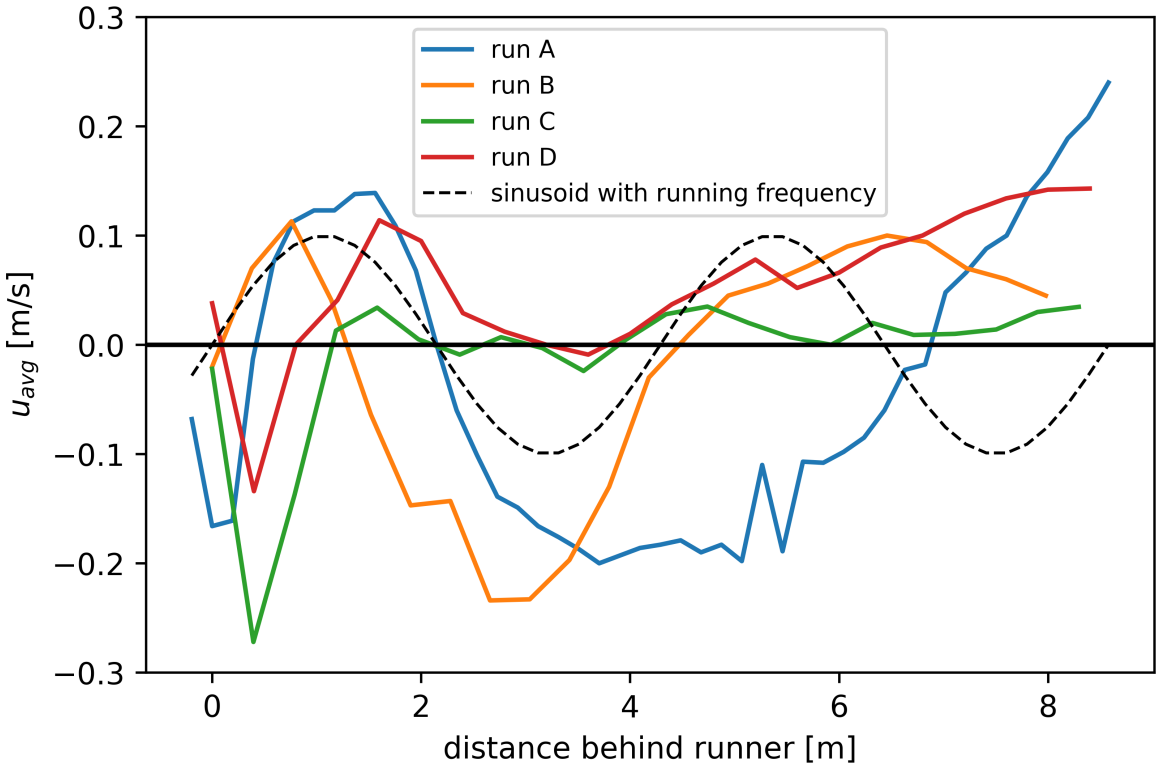

Figure 6.17: Evolution of the average sideways velocity u with distance after passage

In Figure 6.17, even though the average sideways velocity evolution curves all appear different, there is some pattern common to all of them. All the curves begin around zero, while the flow is passing around the runner roughly symmetrically. Then, the average flow quickly jumps to the left (within 0.1s). After some time, all wakes develop an average rightwards flow, and a quarter of a phase later, the average flow is again leftwards.

Comparing with the frequency of the black sinusoid, the frequency of the sideways oscillations seems to be similar. This fact suggests that for each phase of the run there is a corresponding sideways direction in which the flow travels.

It is also worth noting that run B, which has a slighlty earlier phase than run A and C, also has an earlier phase in Figure 6.17. However, run D, which has the same phase as run B, does not show this phase difference in Figure 6.17. Run D is also different to the others in the fact that the average sideways oscillation decays quickly and is not distinguishable anymaore after 2 meters.

After around 4 meters, which is equivalent to a whole cycle of 2 steps, the frequency of the oscillation of the curves seems to significantly decrease. This frequency decrease is likely due to the fact that the measurement domain is stationary on the ground, and not following the runner at a constant distance (in which case it is safe to assume that the frequency of the oscillations would be constant).

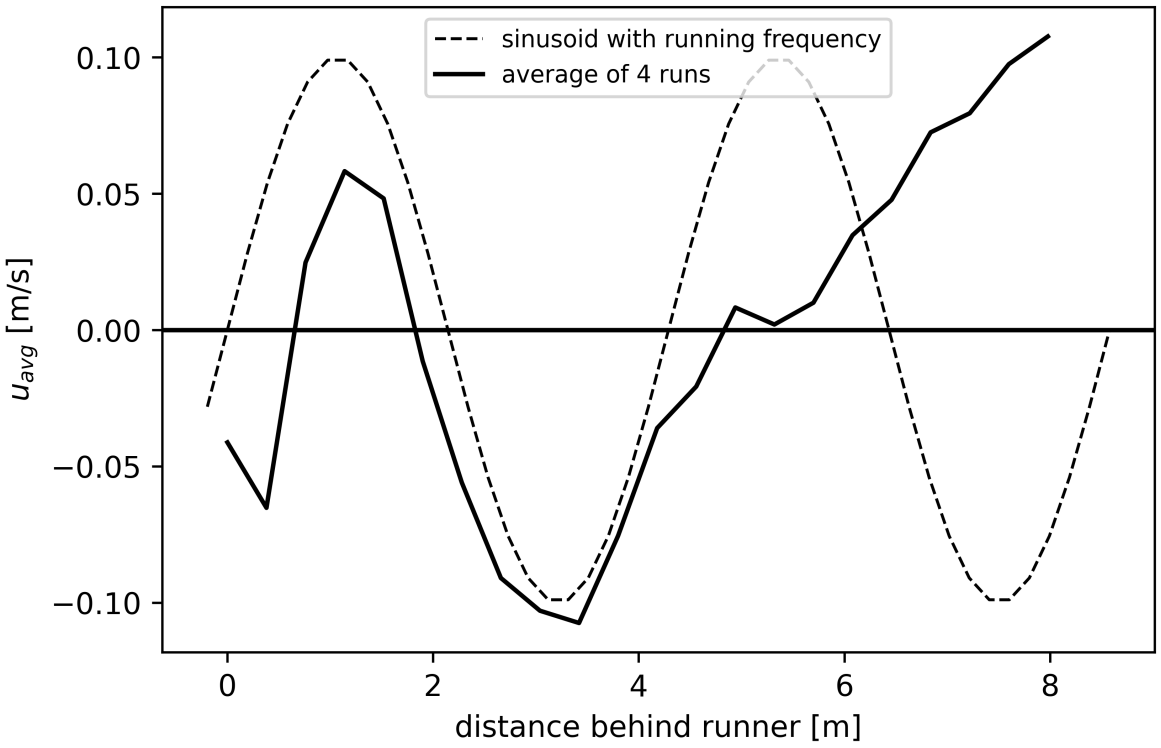

Figure 6.18: Evolution of the average sideways velocity u averaged over the 4 runs with distance after passage

Figure 6.18 shows the curves of Figure 6.17 averaged into one curve, together with the sinusoid matching the frequency of the running cycle.

Here it can be more clearly seen that the averaged sideways flow roughly matches the running cycle frequency, but after around 4 meters the frequency decreases and the wake slowly transitions into a consistent sideways flow. This suggests that the sideways flow is induced by the movement and changing positions of the runner's body, not by an oscillating vortex shedding of a moving cylinder.

Interestingly, instead of the expected gradual decay of the oscillations, the averaged oscillation seems to gain strength over time.

To investigate this curious behaviour, Figure 6.19 and Figure 6.20 show examples of the leftwards and rightwards average flows during run A, and they show the growing magnitude of the sideways flow. The average velocities of the previous figures were relatively small because of the large measurement rectangle size, but here the real magnitude of the velocity can be seen. The leftwards flow at around 4 meters behind the runner reaches around 1 m/s, and the rightwards flow around 8 meters behind the runner reaches as high as 2 m/s, which is a quarter the runner's velocity. Since no decay has been observed, an investigation of lateral velocity behaviour further downstream would give a better overview of the full phenomenon.

As for the cause of the lateral velocity oscillation, it has been concluded that the lateral movement of the flow depends on the movement cycle of the runner, so it is reasonable to say that the lateral velocities are created either by the shape of the runner's body in one of the phases, or by the movement of the body.

In subsection 2.4.1 it has been discovered that for a static model of a race walker in an asymmetrical position (left hand forward, right hand close to the body) the wake deforms slightly to one side. This was shown specifically in Figure 2.5. Therefore, the asymmetrical positions that the runner takes while running should be a cause for the alternating lateral flow.

Another cause of the lateral oscillations could be the movement of the arms, which in some phases move significanlty faster or slower with respect to the stationary air than the rest of the body. Further-

more, the height where the arms pass next to the hips corresponds to the height where the largest lateral oscillation is observed.

It is also interesting to note that the alternating behaviour of the lateral velocity corresponds very closely to the change of sign of the vorticity, back in Figure 6.15 in subsection 6.3.5.

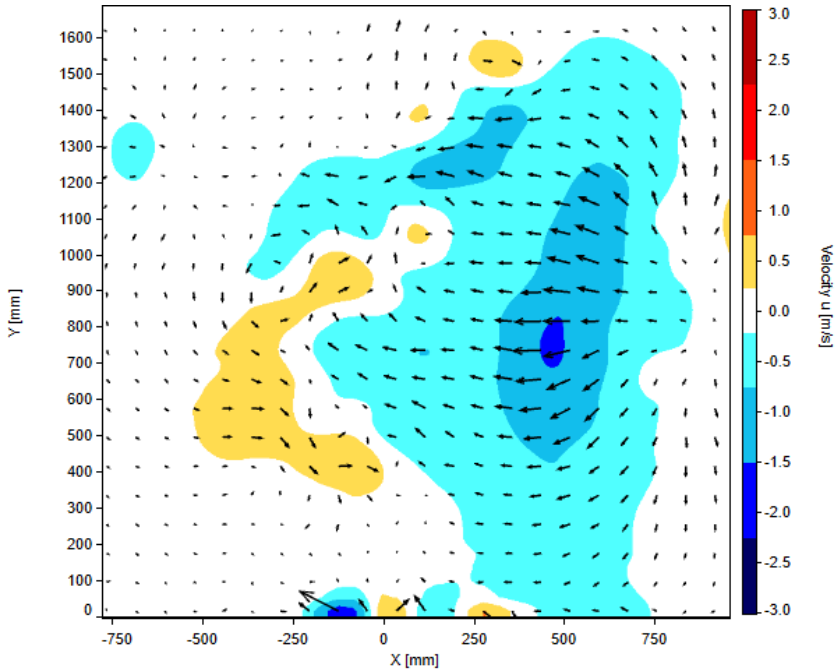

Figure 6.19: Example of the left-traveling average flow of run A - 4 m behind runner

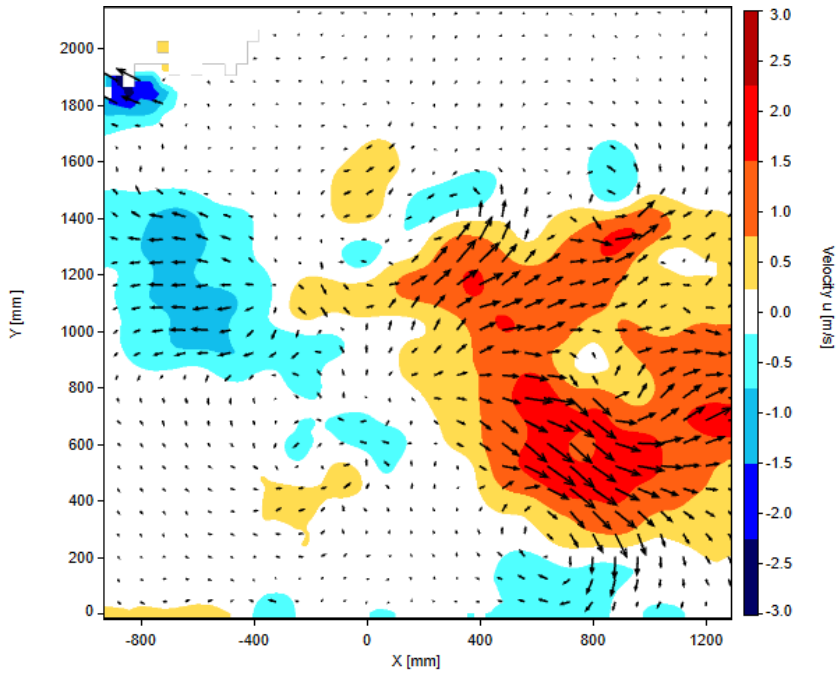

Figure 6.20: Example of the right-traveling average flow of run A - 8 m behind runner

Lastly, Figure 6.21 shows the lateral velocity field from the top view, sliced at $y = 830mm$, corresponding to the height of the hips. Like before, this height is chosen because that is where the far wake develops,

so maximum flow information is available at this height. The visualisation is made to facilitate the understanding of the full evolution of the lateral velocity.

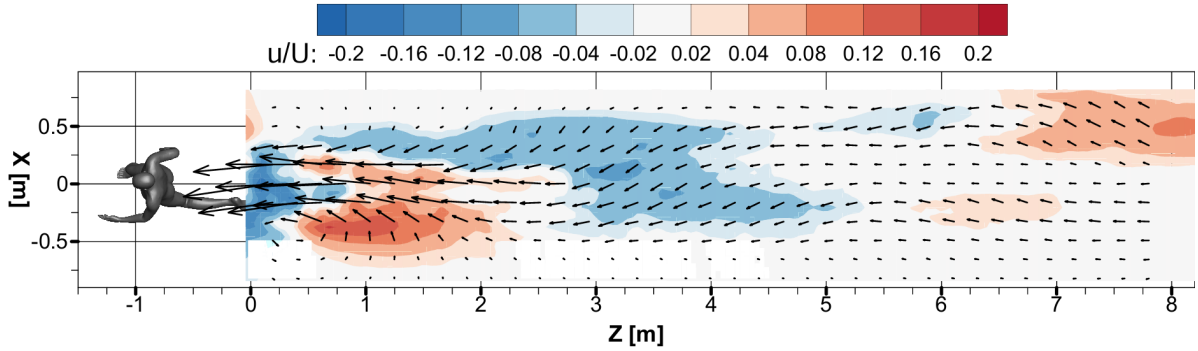

Figure 6.21: top view of the lateral flow averaged from 4 runs, measured at the height $y = 830mm$

6.5. Drag analysis

The method for obtaining drag from a known wake is described in section 3.5. In short, conservation of momentum is evaluated in a volume around the runner, considering the freesream flow and the wake flow.

For a sphere, it has been found by Terra et al. [18] that reliable drag results can be obtained after around 2 sphere diameters, because the drag term of Equation 3.1 has high uncertainty, but decays quickly. Assuming a shoulder width of no more than 50cm for the athlete, it is safe to estimate the drag after 2 body diameters into the wake. Therefore, Figure 6.22 shows the drag areas ($C_D A$) of the runs analysed in this thesis, starting from 1m into the wake. The drag values after 3m into the wake are not shown to minimise the loss of the wake's momentum to the environment, and therefore to minimise the error. Section 5.5 explains the procedure for obtaining the drag area from the velocity data.

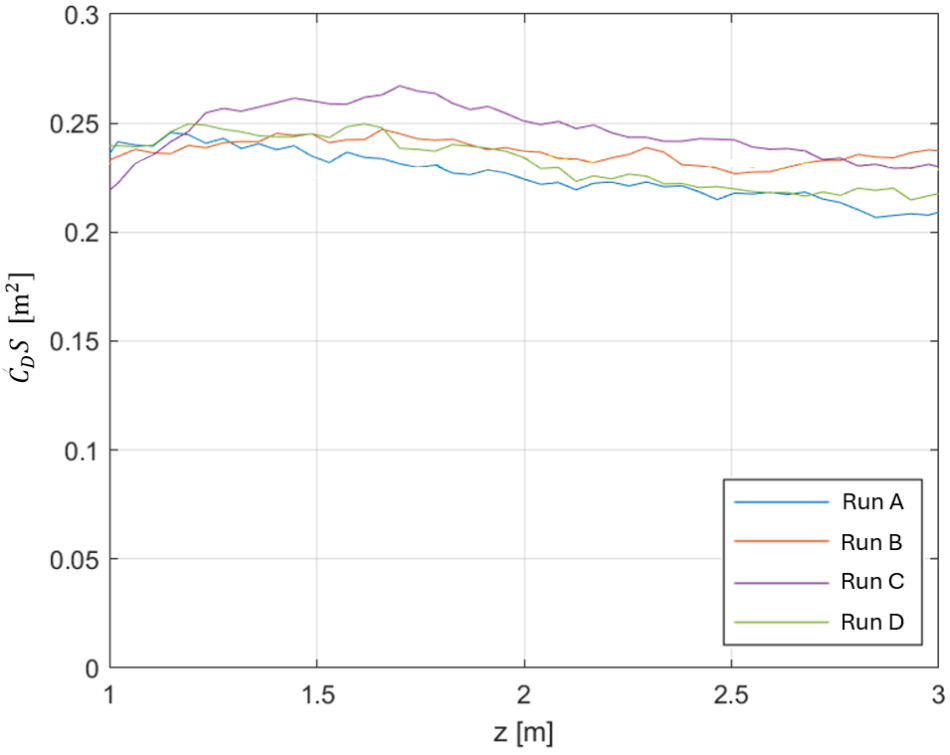

Figure 6.22: Evolution of drag area with distance behind the runner for all 4 runs

The 4 runs have similar drag results, with differences of up to 15% between the lowest and the highest values. The average drag area of the athlete from these 4 runs is in the range of 0.23-0.24 m^2, which equals to an effective area of half of that value, which is around $0.1175m^2$

Those values are significanlty smaller than the findings of Pecchiari et al. [11]. In their study, where drag of real runners was measured by a treadmill in a wind tunnel, a runner with a height of 165-170cm at a running speed of 5m/s would have an effective area of around 0.2 m^2, which is almost double of the measured drag in this thesis.

One possible reason for that difference is the difference in running speeds. Pecchiari et al. state that "in this speed range ($5m/s$) the velocity dependence of drag area is small", but they do not show data beyond a speed of $5m/s$. It is possible that the Reynolds number change between $5m/s$ and $8m/s$ is significant enough to reduce the drag, or the running technique at a higher speed is more aerodynamically efficient.

The difference between the drag values of this thesis and Pecchiari's could also be due to the runners themselves. Pecchiari had professional male, adult runners, while this thesis is based on a junior female runner, so the running technique and the body proportions are most probably different.

Adding the runner from this thesis to the dataset created by Pecchiari results in Figure 6.23.

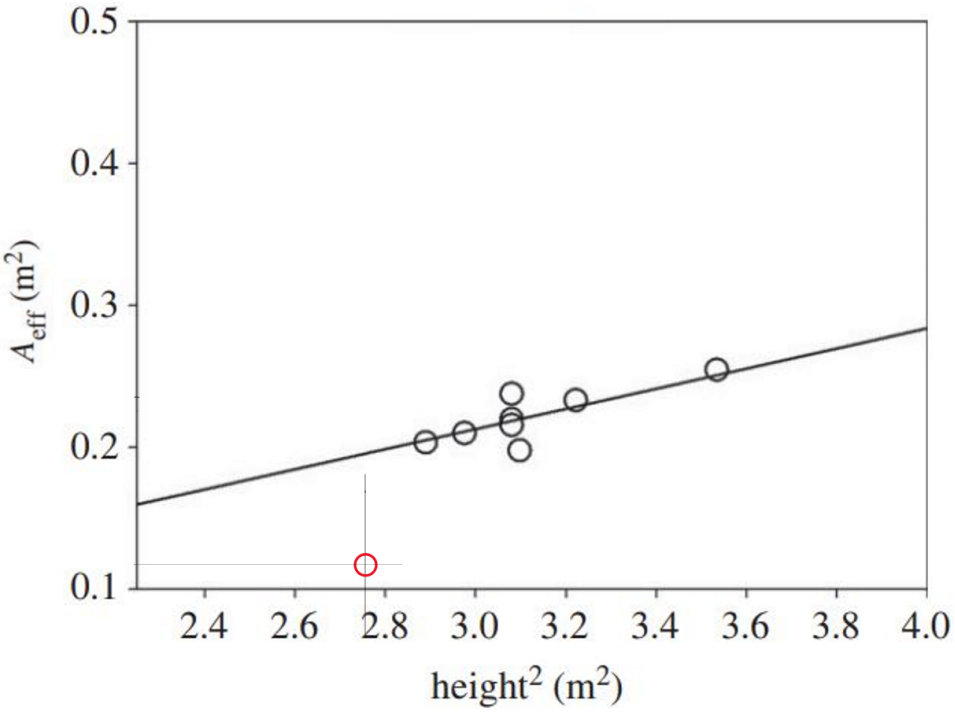

Figure 6.23: Effect of runner's height on the drag area by Pecchiari et al. [11] The red datapoint is an addition from this thesis.

7

Conclusion

This research investigated the aerodynamics of sprinting with the use of large-scale particle tracking velocimetry (PTV) in a ”Ring-of-Fire” setup. The focus of the research is to develop new knowledge on flow topology in the wake of a runner.

Helium filled soap bubbles (HFSB) were used as tracer particles with a maximum acquisition frequency of 400 Hz. The running speeds were around 8 m/s, measured with a laser system pointing at the runner from behind. The imaging system, using 4 LED arrays in a vertical arrangement and 3 high speed cameras, captured three-dimensional velocity data over a 2.7 m × 2.7 m × 0.3 m volume at a digital resolution of 2.51 mm/pixel. Nine junior athletes participated in the experiments and the athlete with the best data quality and most consistent running technique was chosen for analysis. The chosen athlete is a female with a height of 165-170cm.

7.1. Findings

This thesis has one main research question, which can be split into subquestions, as follows:

What are the general characteristics of airflow in the wake of a real moving sprinter?

- What is the evolution of the flow velocity component in the direction of the runner?
- Where are the main vorticity structures around the runner’s body?
- How does the lateral velocity of the flow depend on the phase of the runner’s movement?
- What is the drag area of the runner?

This section presents the key results of the investigation to answer those research questions, including the visualisation of the full wake, quantification of the velocity deficit, a vorticity analysis, some lateral velocity findings and the measured values for drag of the athletes.

The general three-dimensional wake has been visualised using the average flow of 4 runs in which the runner was passing through the measurement domain in the same phase of her step. The bulk of the wake has been found to originate from the torso. As the wake evolves, it shrinks vertically and expands horizontally, and most of it remains at hip height. An interesting phenomenon has been found in the far wake, mainly the wake splits into 2 side-by-side sub-wakes.

The velocity deficit has been found to vary with x^{-1}, where x is the distance behind the runner. This approximation is valid between 2m and 8m behind the runner, which is conveniently the range of distances in which a second runner would be running to gain an aerodynamic benefit.

A vorticity analysis has been performed and some of the vorticity structures are repeatable between different runs. It has been found that vorticity areas can be predicted by comparing the body to a finite cylinder flow, where the tip of the cylinder sheds vorticity. With this in mind, the shoulder vorticity is the strongest. The swinging hands also caused significant vorticity, and the creation of the vorticity on the sides of the wake have been linked to the phase in which the swing of the arm is in. Lastly, the analysis

using a λ_2 criterion showed no consistent vortex formations between the different runs. The only vortex that is shared between the 4 runs is a clockwise vortex on the left of the wake, but it is only temporary and it disappears after 0.5m of wake evolution.

Furthermore, the lateral velocity has been investigated, and it has been linked to the phase of the step that the runner is in. The lateral oscillations of the wake are quite strong, reaching up to a quarter of the runner's velocity in the far wake. The lateral movements have been shown to not decay in the first 8m of the wake, which is interesting considering that the velocity in the running direction decays quickly.

Lastly, the average drag area of the athlete is in the range of 0.23-0.24, which is comparable but slightly higher than what is found in literature.

7.2. recommendations

Based on the findings and challenges encountered in this research, this section proposes some recommendations for future investigations based on this research or for investigations of similar nature.

One of the main conceptual errors in this investigation is that while the athletes were wearing aerodynamic clothing and keeping a constant speed to make the results uniform, the female athletes had loose long hair, which is proven to be a major source of drag and very probably a major source of inconsistency between runs. Kyle et al. showed that a head with long loose hair generates almost 2 times more drag than a head with long hair covered with a rubber cap [5]. Covering long or short hair with a cap in future experiments on runners would complete the rest of the aerodynamic clothing they wear and could potentially lead to more repeatable results.

Another recommendation for future Ring of Fire systems is to further improve the new concept for the piston-cylinder seeding system, which is illustrated and discussed in the appendix. Multiple recommendations can be tested for this purpose. Firstly, the hole size and the release speed can be increased to reduce the time needed for seeding release and give the seeding less time to move away from the measurement domain. Secondly, the holes can be pointed at slight angles to the front and to the back of the tube, to increase the thickness of the created seeding volume, again giving more time before the seeding gets blown away. Lastly, to accommodate for those changes, multiple seeding nozzles and/or a larger diameter cylinder can be used to increase the maximum total number of bubbles that are available in 1 stroke of the piston-cylinder system. Implementing those improvements will allow the Ring of Fire user to transition from the current seeding rake system to the piston-cylinder system to achieve a more uniform tracer distribution and reduce manual intervention in the experiment procedure.

A suggestion for further research is to investigate the mechanic behind the wake splitting into two side-by-side wakes. This thesis suggested that a possible cause for this wake behaviour is the arms having a higher maximum velocity with respect to the air than the rest of the body, which could make the momentum of the arm's wake stay in the air for a longer time than the wake of the rest of the body. However, this is just a guess and further investigation is needed to understand this behaviour.

References

[1] L. Schickhofer and H. Hanson. “Aerodynamic effects and performance improvements of running in drafting formations”. In: *Journal of Biomechanics* 122 (June 2021). ISSN: 18732380. DOI: 10.1016/j.jbiomech.2021.110457.

[2] A. V. Hill. *The Air-Resistance to a Runner*. Dec. 1927. URL: https://royalsocietypublishing.org/.

[3] F. Alam H. Chowdhury and A. Subic. “Aerodynamic performance evaluation of sports textile”. In: *a*. Vol. 2. Elsevier Ltd, 2010, pp. 2517–2522. DOI: 10.1016/j.proeng.2010.04.025.

[4] J. Carbo E. Harber R. Henry I. Ilcheva L. Brownlie Y. Aihara and P. Ostafichuk. “The Use of Vortex Generators to Reduce the Aerodynamic Drag of Athletic Apparel”. In: vol. 147. Elsevier Ltd, 2016, pp. 20–25. DOI: 10.1016/j.proeng.2016.06.183.

[5] C. R. Kyle and V. J. Caiozzo. “The effect of athletic clothing aerodynamics upon running speed”. In: *Medicine and Science in Sports and Exercise* (1986).

[6] F. Bogard S. Murer V. Vernede F. Beaumont F. Legrand and G. Polidori. “Aerodynamic interaction between in-line runners: new insights on the drafting strategy in running”. In: *Sports Biomechanics* (2021). ISSN: 17526116. DOI: 10.1080/14763141.2021.2006295.

[7] J. R. Mureika. *The Legality of Wind and Altitude Assisted Performances in the Sprints*. 2001.

[8] P. Ke Y. Zhang and P. Hong. “Aerodynamic Drag Reduction Analysis of Race Walking Formations Based on CFD Numerical Simulations and Wind Tunnel Experiments”. In: *Applied Sciences (Switzerland)* 13 (19 Oct. 2023). ISSN: 20763417. DOI: 10.3390/app131910604.

[9] J. Teixeira D. Marinho A. Monteiro J. Bragada J. Morais P. Forte N. Sousa and T. Barbosa. “Aerodynamic analysis of human walking, running and sprinting by numerical simulations”. In: *Acta of Bioengineering and Biomechanics* 24 (3 2022), pp. 3–11. ISSN: 1509409X. DOI: 10.37190/ABB-02019-2022-06.

[10] V. T. Ho D. Shin J. Kim S. Lee and J. Ryu. “Effects of Speed and Posture on Aerodynamic Characteristics of Running and Required Power”. In: *International Journal of Applied Mechanics* 15 (1 Jan. 2023). ISSN: 1758826X. DOI: 10.1142/S1758825122501058.

[11] G. Gibertini M. M. Pecchiari M. A. Legramandi and G. A. Cavagna. “Still air resistance during walking and running”. In: *Proceedings of the Royal Society B: Biological Sciences* 290 (2013 Dec. 2023). ISSN: 14712954. DOI: 10.1098/rspb.2023.1763.

[12] A. Sciacchitano G. C. A. Caridi D. Ragni and F. Scarano. “HFSB-seeding for large-scale tomographic PIV in wind tunnels”. In: *Experiments in Fluids* 57 (12 Dec. 2016). ISSN: 07234864. DOI: 10.1007/s00348-016-2277-7.

[13] F. Scarano A. Spoelstra A. Sciacchitano and N. Mahalingesh. “On-site drag analysis of drafting cyclists”. In: *Journal of Wind Engineering and Industrial Aerodynamics* 219 (Dec. 2021). ISSN: 01676105. DOI: 10.1016/j.jweia.2021.104797.

[14] W. Terra A. Spoelstra and A. Sciacchitano. “On-site aerodynamics investigation of speed skating”. In: *Journal of Wind Engineering and Industrial Aerodynamics* 239 (Aug. 2023). ISSN: 01676105. DOI: 10.1016/j.jweia.2023.105457.

[15] A. Roshko. “Perspectives on bluff body aerodynamics”. In: *Journal of Wind Engineering and Industrial Aerodynamics* 49.1 (1993), pp. 79–100. ISSN: 0167-6105. DOI: https://doi.org/10.1016/0167-6105(93)90007-B. URL: https://www.sciencedirect.com/science/article/pii/016761059390007B.

[16] E. Achenbach. “Influence of surface roughness on the cross-flow around a circular cylinder”. In: *Journal of Fluid Mechanics* 46.2 (1971), pp. 321–335. DOI: 10.1017/S0022112071000569.

[17] T. Teraoka S. Maeno T. Inoue T. Okayama and K. Hirata. “Wind-tunnel experiment on aerodynamic characteristics of a runner using a moving-belt system”. In: *Cogent Engineering* 3.1 (2016). Ed. by Z. Jin, p. 1231389. DOI: 10.1080/23311916.2016.1231389. URL: https://doi.org/10.1080/23311916.2016.1231389.

[18] A. Sciacchitano W. Terra and F. Scarano. “Aerodynamic drag of a transiting sphere by large-scale tomographic-PIV”. In: *Experiments in Fluids* 58 (7 July 2017). ISSN: 07234864. DOI: 10.1007/s00348-017-2331-0.

[19] R. G. J. Flay. “Bluff Body Aerodynamics”. In: *Advanced Structural Wind Engineering*. Ed. by Y. Tamura and A. Kareem. Tokyo: Springer Japan, 2013, pp. 59–84. ISBN: 978-4-431-54337-4. DOI: 10.1007/978-4-431-54337-4_3. URL: https://doi.org/10.1007/978-4-431-54337-4_3.

[20] C. E. Willert S. T. Wereley F. Scarano M. Raffel C. J. Kähler and J. Kompenhans. *Particle Image Velocimetry: A Practical Guide*. English. 3rd. Springer, 2018. ISBN: 978-3-319-68851-0. DOI: 10.1007/978-3-319-68852-7.

[21] A. Sciacchitano W. Terra and Y. H. Shah. “Aerodynamic drag determination of a full-scale cyclist mannequin from large-scale PTV measurements”. In: *Experiments in Fluids* 60 (2 Feb. 2019). ISSN: 07234864. DOI: 10.1007/s00348-019-2677-6.

[22] S. Gesemann D. Schanz and A. Schröder. “Shake-The-Box: Lagrangian particle tracking at high particle image densities”. In: *Experiments in Fluids* 57 (5 May 2016). ISSN: 07234864. DOI: 10.1007/s00348-016-2157-1.

[23] F. Scarano. *Tomographic PIV: Principles and practice*. 2013. DOI: 10.1088/0957-0233/24/1/012001.

[24] F. Erzinger M. Quadrio F. J. W. A. Martins J. Kirchmann A. Melling S. M. Tauwald and A. Kronenburg. *Tracer particles and seeding for particle image velocimetry You may also like Tomo-PIV in a patient-specific model of human nasal cavities: a methodological approach This content was downloaded from IP address 131 Tracer particles and seeding for particle image velocimetry*. 1997.

[25] M. Kühn J. Bosbach and C. Wagner. “Large scale particle image velocimetry with helium filled soap bubbles”. In: *Experiments in Fluids* 46 (Mar. 2009), pp. 539–547. DOI: 10.1007/s00348-008-0579-0.

[26] G. C. A. Caridi J. Bosbach U. Dierksheide F. Scarano S. Ghaemi and A. Sciacchitano. “On the use of helium-filled soap bubbles for large-scale tomographic PIV in wind tunnel experiments”. In: *Experiments in Fluids* 56 (2 Feb. 2015). ISSN: 14321114. DOI: 10.1007/s00348-015-1909-7.

[27] L. de Martino Norante A. Spoelstra and W. Terra. “On-site cycling drag analysis with the Ring of Fire.” In: *Exp Fluids 60, 90* (2019). URL: https://doi.org/10.1007/s00348-019-2737-y.

[28] J. Ashton and P. A. Jones. “The Reliability of Using a Laser Device to Assess Deceleration Ability”. In: *Sports (Basel, Switzerland)* 7,8 (2019). DOI: 10.3390/sports7080191.

[29] *Product Manual for DaVis 10.2*.

[30] A. Sciacchitano A. Spoelstra M. Hirsch and F. Scarano. “Uncertainty assessment of the Ring of Fire concept for on-site aerodynamic drag evaluation”. In: *Sports (Basel, Switzerland)* (2020). DOI: https://doi.org/10.1088/1361-6501/abb50d.

[31] S. B. Pope. *Turbulent Flows*. Cambridge University Press, 2000.

[32] J. Jeong and F. Hussain. “On the identification of a vortex”. In: *Journal of Fluid Mechanics* 285 (1995), pp. 69–94. DOI: 10.1017/S0022112095000462.

A

New seeding injection system

As mentioned in subsection 3.4.2, a part of this thesis was developing a new seeding injection system.

The main principle of the new system is the accumulation of HFSB in a large cylinder, and pushing them out with a piston through a perforated long tube that wraps around the desired domain, releasing bubbles uniformly, right where they are needed. The system operates on only one nozzle, as opposed to the current 264 nozzles. A sketch of the system is presented in Figure A.1 and a A zoomed-in sketch of the piston-cylinder system that pushes seeding into the tube is presented in Figure A.2.

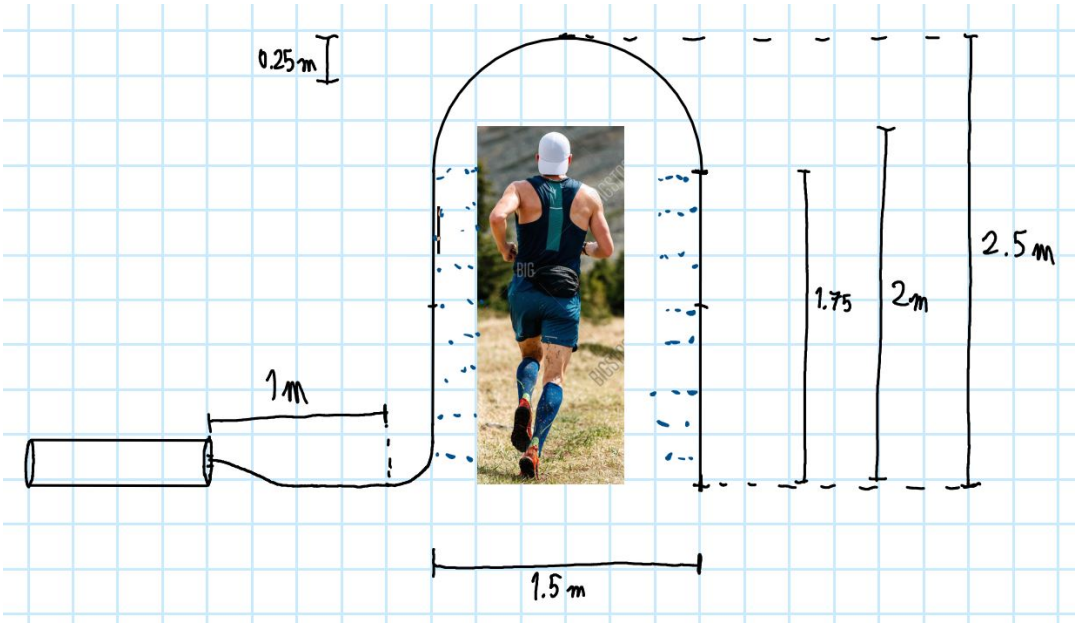

Figure A.1: A sketch of the piston-cylinder seeding injection system

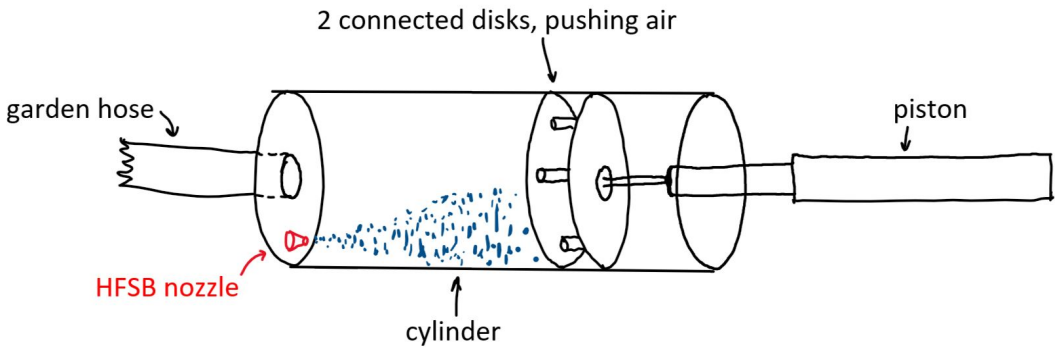

Figure A.2: A zoomed-in sketch of the piston-cylinder system that pushes seeding into the tube

The hose is pressurised with air full of seeding as shown in Figure A.2. The tube is tightly connected to an opening in the left wall, while the right wall travels to the left, pushed by a Kollmorgen actuator. The right wall is made as tight as possible to the inner cylinder wall with painting tape, which adds a small thickness and is able to slide across the inner wall of the cylinder. The maximum tightness allowed is such that the piston does not get jammed inside of the cylinder, and it provides sufficient pressurisation to release seeding from the entire tube. There are 2 piston discs to improve pressurisation, similarly to the design of piston rings in internal combusion engines.

The seeding is supplied by 1 HFSB nozzle, friction fitted into a small hole in the left wall of the cylinder. The cylinder is made of plexiglass and has an internal diameter of 30cm and a lenght of above 1 meter.

The garden hose wraps around the measurement domain as shown in Figure A.1, supported in this position by a wooden frame. There are holes in the tube with a diameter of 2.5mm and a spacing of 10cm, with an equal amount of holes on the left and right sides of the tube.

With those hole dimensions, an optimal piston velocity was found by trial and error to be 0.02-0.03 m/s, so the full stroke of bubble release lasts slightly longer than 30s. With this velocity, the bubbles get released from the tubes, the streams of air from the left and right sides collide gently, and the seeding remains in the measurement domain. At lower release velocities the tube is not pressurised enough, and at higher release velocity the seeding travels too far and exits the measurement domain before the flow settles down.

A setup with bigger holes, of diameter 6mm was tried initially, but the seeding was only coming out from the half of the tube next to the cylinder. The other half of the tube was not pressurised, even at high piston speeds, which made the entire measurement domain filled with seeding that has a momentum to the side, clearly not good for a Ring-of-Fire system. With the knowledge available now, this setup could have worked by adding more paper tape around the piston rings to pressurise the cylinder better and using fast release speeds. This can be worth experimenting with in the future.

During the day of experiment preparation in Apeldoorn, the piston-cylinder system worked as intended, but a slight wind through the measurement tunnel was carrying the seeding downstream even before the seeding release got finalised. This exposes the problem of a release time of the order of 30 seconds - the system becomes sensitive to any air movement during and after seeding release. It is possible that a tube with bigger holes and faster release time could have prevented this problem.

In the end, the backup solution of a seeding rake with 200 nozzles was used, and there was so much seeding available that it could be spread across a thicker volume and it was therefore not sensitive to slight winds.

B

Vortex identification using the λ_2 criterion

The λ_2 criterion is explained by Jeong Hussain in [32]. The variable quantifies the swirling strength of a flow field at every point, which is useful for vortex detection λ_2 is negative in regions of the flow where rotation dominates over strain, and it is zero where there is little rotation, but strong strain, for example in a shear layer.

The mathematical procedure for obtaining the λ_2 values is as follows:

- Velocity Gradient Tensor Analysis: The velocity gradient tensor, $\nabla \mathbf{u}$, is decomposed into its symmetric and antisymmetric parts, like shown in Equation B.1.

$$\nabla \mathbf{u} = \mathbf{S} + \mathbf{\Omega} \tag{B.1}$$

  Where $\mathbf{S}$ is the symmetric rate-of-strain tensor and $\mathbf{\Omega}$ is the antisymmetric rate-of-rotation tensor.
- Identification of Rotational Regions: The criterion analyzes the eigenvalues of the tensor $\mathbf{J} = \mathbf{S}^2 + \mathbf{\Omega}^2$. In regions of swirling motion, $\mathbf{J}$ has three real eigenvalues ($\lambda_1, \lambda_2, \lambda_3$) ordered such that $\lambda_1 \geq \lambda_2 \geq \lambda_3$.
- λ_2 Criterion: A vortex is identified if the second-largest eigenvalue, λ_2, is negative ($\lambda_2 < 0$). This indicates that the local flow structure has a net rotational dominance, signifying swirling motion.

Figures B.1, B.2 and B.3 show the λ_2 fields of runs A, B and C, respectively. The images are taken at the same frames as figures 6.10, 6.11 and 6.12 and they act as complements to the vorticity analysis in section 6.3.

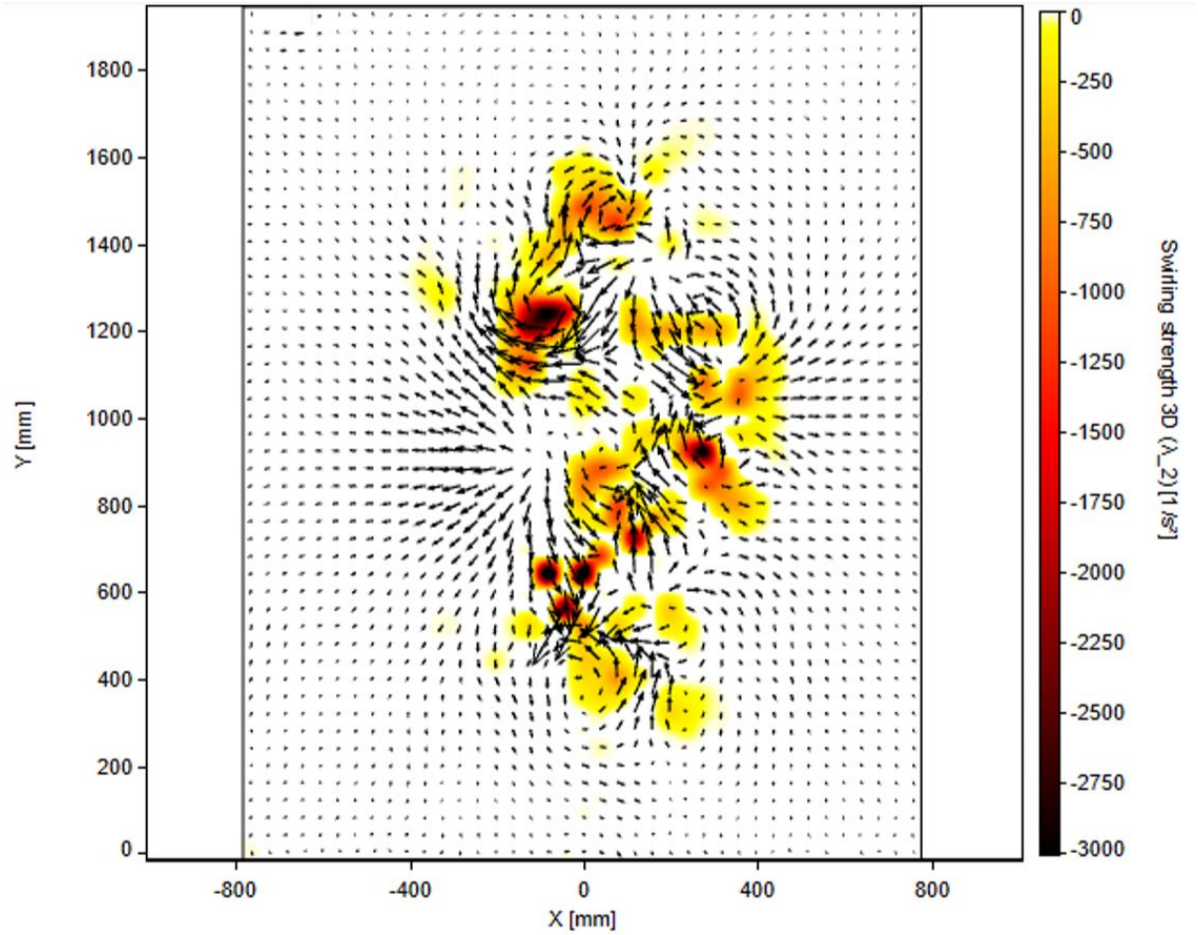

Figure B.1: λ_2 field of run A, at the same frame as Figure 6.10

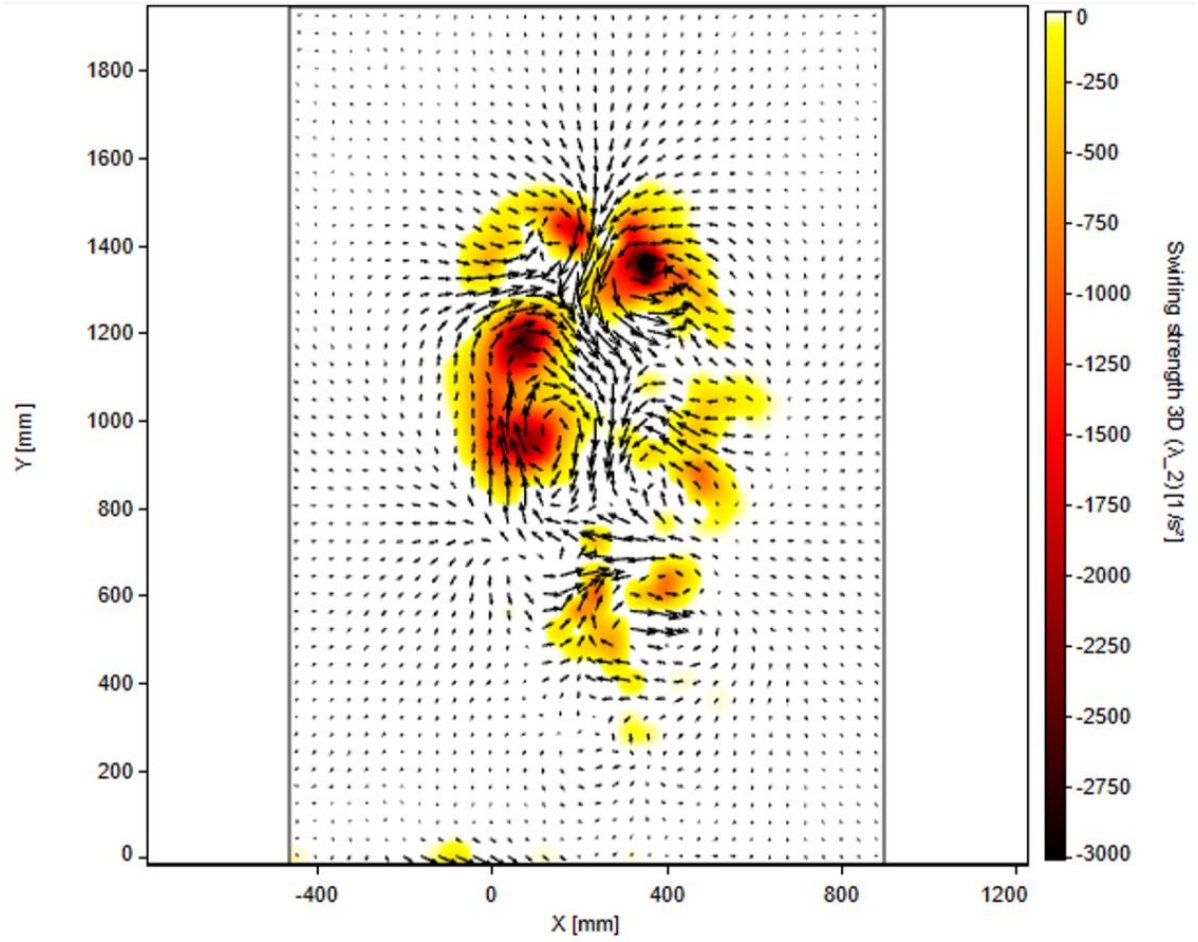

Figure B.2: λ_2 field of run B, at the same frame as Figure 6.11

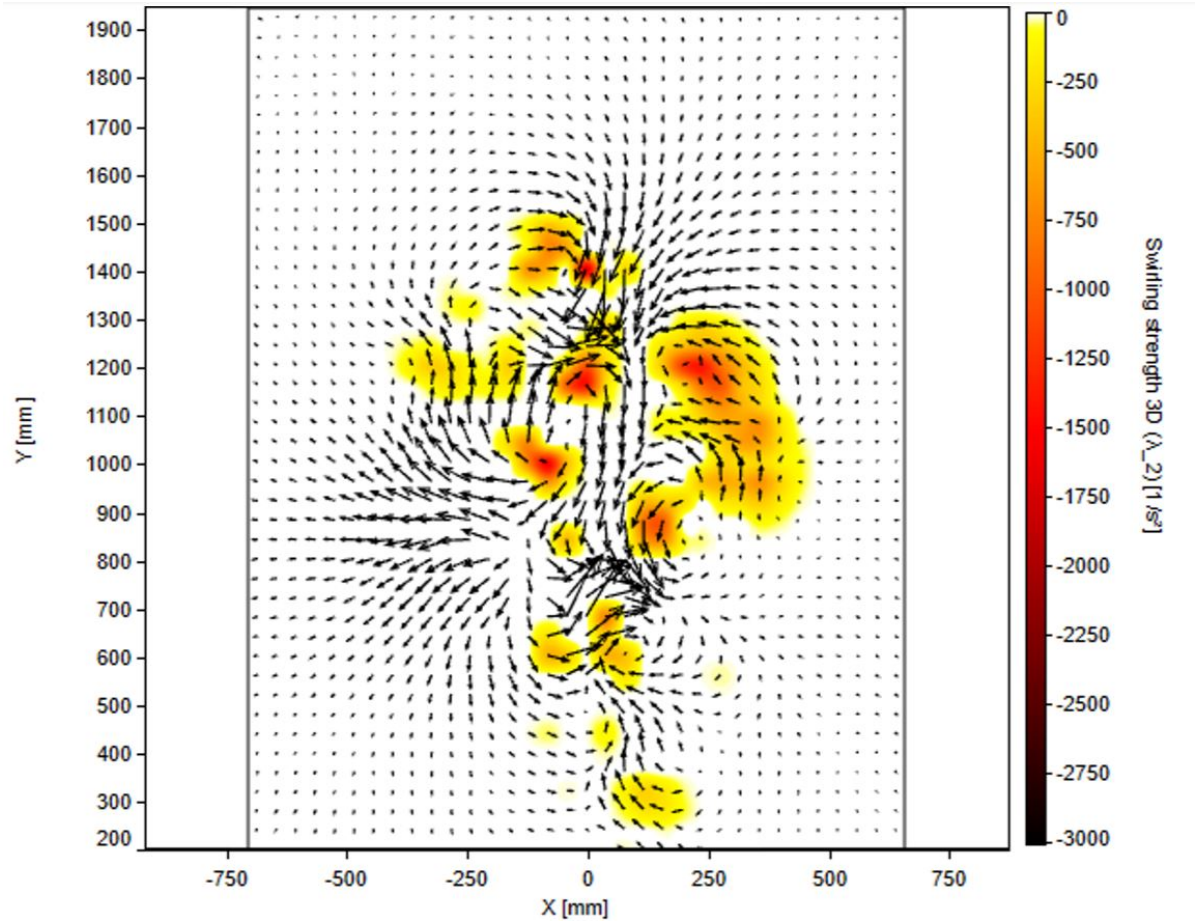

Figure B.3: λ_2 field of run C, at the same frame as Figure 6.12

C

Test matrix

Table C.1 is the test matrix of the last day of the experiment. Only the last day is presented because that is when the experimental setup was finalised and only this data is considered for analysis.

Runs 63, 66, 81 and 84, corresponding to runs A, B, C and D in this report, do not have any negative comments, therefore the seeding and the acquisition were good.

Table C.1: Test matrix of the last measurement day

Run number	Athlete	Suit	Speed [m/s]	Comments
063	7	aero	7.8	
064	8	aero	8.3	
065	9	sprint	8.2	
066	7	aero	7.6	Did not save the first time
067	8	sprint	8.2	
068	9	sprint	8.7	
069	7	sprint	7.8	
070	8	aero	8.3	A bit too high seeding
071	9	aero	8.4	
072	7	sprint	7.9	Maybe she was slowing down in the ’tunnel’
073	8	aero	8.4	
074	9	sprint	8.4	Few bubbles on bottom left
075	7	sprint	8.1	
076	8	aero	8.3	
077	9	aero	8.6	Few bubbles on bottom left
078	7	aero	7.9	
079	8	sprint	8.3	
080	9	aero	8.6	
081	7	aero	7.9	
082	8	sprint	8.2	Few seeding centre bottom
083	9	aero	8.5	
084	7	aero	8	
085	8	aero	8.3	
086	9	aero	8.6	High seeding on the right, few on the left
087	7	sprint	7.9	
088	8	sprint	8.3	
089	9	sprint	8.4	
090	7	sprint	8.2	
091	8	sprint	8.2	
092	9	sprint	8.5	